PHOTONUCLEAR REACTION MECHANISMS AT INTERMEDIATE ENERGIES

A Thesis

Submitted to the College of Graduate Studies and Research

in Partial Fulfillment of the Requirements

for the Degree of Doctor of Philosophy

in the

Department of Physics and

Engineering Physics

University of Saskatchewan

by

Kenneth Roy Garrow

Saskatoon, Saskatchewan

CANADA

Spring, 1998

In presenting this thesis in partial fulfilment of the requirements for a Postgraduate degree from the University of Saskatchewan, the author agrees that the Libraries of this University may make it freely available for inspection. The author further agrees that permission for copying of this thesis in any manner, in whole or in part, for scholarly purposes may be granted by the professor or professors who supervised the thesis work or, in their absence, by the Head of the Department or the Dean of the College in which the thesis work was done. It is understood that any copying or publication or use of this thesis or parts thereof for financial gain shall not be allowed without the author's written permission. It is also understood that due recognition shall be given to the author and to the University of Saskatchewan in any scholarly use which may be made of any material in the thesis.

Requests for permission to copy or make other use of material in this thesis in whole or part should be addressed to:

Head of the Department of Physics and Engineering Physics
University of Saskatchewan
Saskatoon, Saskatchewan S7N 0W0

Abstract

The work reported in this thesis is an experiment performed using the tagged photon facility at the Saskatchewan Accelerator Laboratory. Results were obtained due to the collaboration of the University of Saskatchewan, Trent University and the University of Melbourne.

The goal of the present experiment was to study the reaction mechanisms involved in the absorption of photons by nuclei in the energy range $E_\gamma = 60$ to 140 MeV. For the photon energy of 64 MeV the $^{16}O(\gamma, p)^{15}N_{g.s.}$ reaction cross section was measured. A description of the process in terms of a direct knockout formalism was inadequate to explain the magnitude of the measured cross section. The inclusion of two-body meson-exchange-currents in the calculation was found to give a much better fit to the data.

Of particular interest for this experiment was the study of the absorption of a photon on a correlated proton-neutron pair for the photon energy range $E_\gamma = 100$ to 140 MeV. The two-nucleon absorption mechanism is dominant in this photon energy range. The reaction studied was $^{16}O(\gamma, pn)^{14}N_{0,1,2,..}$. Having sufficient experimental energy resolution to determine the population to discrete states in the residual ^{14}N nucleus provided information on the quantum numbers involved in the two-nucleon absorption mechanism. Also the large continuum yield at excitation energies larger than 20 MeV compared to the yield below 20 MeV is seen as evidence that short range nucleon-nucleon correlations play a significant role for the two body reaction mechanism in the photon energy region studied.

To complement the present study of absorption mechanisms, a previous measurement performed by the author in 1990 is contained in Appendix B. This inclusive

measurement of the $^{12}C(\gamma, p)$ reaction was also carried out using the tagged photon facility at the Saskatchewan Accelerator Laboratory. Photoproton spectra were obtained for the photon energy range from 177 to 217 MeV at the laboratory angles θ_p = 51°, 81°, 109° and 141°. When the inclusive proton spectra were plotted as a function of momentum, structures indicative of both the quasideuteron (QD) and the quasifree pion production (QFPP) reaction mechanisms were exhibited at the forward angles. At the backward angles the structure of the proton spectra was found to exhibit characteristics arising primarily from the QD reaction mechanism. This is an important feature not previously observed for photonuclear reactions on light nuclei. The inclusive proton spectra are compared to the results of a QD model calculation for a photon energy of 212 MeV where the two-nucleon absorption peak was not obscured by the proton detection threshold inherent for the charged particle detectors used in this measurement. Some of the results of this inclusive measurement given in Appendix B are discussed in Chapter 2 and the conclusions are stated in Chapter 6.

Acknowledgements

I wish to express my sincere gratitude to my supervisor Dr. R. E. Pywell for his dedication to seeing the completion of this thesis. The many conversations with him were both enlightening and encouraging, not to mention invaluable, in obtaining the results presented in this thesis.

I wish to thank all the collaborators involved in this experiment and in particular Dr. M. Thompson of the University of Melbourne for supplying the high resolution CsI detectors necessary so that this experiment could be undertaken. I would also like to thank Dr. J. W. Jury of Trent University for supplying the heavy water which allowed many consistency checks of the experimental data to be performed, and Dr. N. Kolb for his many informative discussions. My thanks to the SAL technical staff who worked extremely hard to keep the accelerator in top operating condition throughout this experiment and the computing science staff for their help with the computing problems encountered. I would like to thank Dr. E. L. Tomusiak whose lectures allowed the calculation presented in Appendix A to be performed. Finally, I would like to express a special acknowledgement to E. Skopik for a thorough editing of this thesis.

This thesis is dedicated to Nicholas and Nina.

Contents

List of Figures

List of Tables

Glossary

AND	And logic unit
CDWIA	Complete distorted wave impulse approximation
CERN	European Center for Nuclear Research, Geneva Switzerland
CFD	Constant fraction discriminator
CM	Center-of-mass
CW	Continuous wave
DKO	Direct knock-out
DWIA	Distorted wave impulse approximation
ECS	Energy compression system
EA2	Experimental area 2
FLUKA	Hadronic interaction package for GEANT
FSI	Final state interaction
FWHM	Full width half maximum
GDR	Giant dipole resonance
GEANT	Detector simulation package developed at CERN
GR	Giant resonance
IA	Impulse approximation
IPM	Independent particle motion
MEC	Meson exchange current
OR	Or logic unit
PMT	Photomultiplier tube
PSR	Pulse stretcher ring
PWIA	Plane wave impulse approximation
QD	Quasideuteron

QFPP	Quasifree pion production
RF	Radio frequency
SAL	Saskatchewan Accelerator Laboratory
SRC	Short range correlations
TDC	Time to digital converter
TOF	Time-of-flight

Chapter 1

Introduction

The electromagnetic interaction is thought to be an ideal probe for the study of nuclear structure. This is because the electromagnetic force is well known and interacts weakly, so that perturbation theory is relevant for theoretical calculations describing photonuclear interactions. The absorption of electromagnetic radiation by nuclei is usually studied assuming that the reaction mechanism is known. The particular reaction mechanism used depends on the energy of the absorbed quanta. For instance for low energy photons of the order of 20 MeV the wavelength is of the order of a few times the nuclear radius so the reaction mechanism or model is that of the photon interacting with the nucleus as a whole. At higher photon energies when the wavelength is of the order of the internucleon spacing the photon is assumed to interact with a single nucleon when the momentum mismatch is not too large or a pair of nucleons in the case of a large momentum mismatch between the incident photon and ejected nucleons.

Experimental observations provide important clues as to the physical nature of the reaction mechanism. One of the most striking experimental observations is that the (γ, p) and (γ, n) cross sections are of comparable magnitude [16, 17, 18, 19, 20, 21] over a photon energy range from the giant dipole resonance (GDR), ~20 MeV, to a photon energy of approximately 200 MeV. In the GDR region, collective models for the absorption of photons were able to account for this phenomenon by the introduction of the concept of an effective charge for the neutron. As the oscillating electric field of the photon induces vibrations in the proton fluid, the neutrons move in the opposite direction to keep the center-of-mass (CM) fixed, thereby acquiring an effective charge

which is equal in magnitude but opposite in polarity to that of the proton. For photon energies in the GDR region, the photon wavelength is typically two to three times larger than the size of the nucleus and was therefore thought to excite gross degrees of freedom of the nucleus. With this photoabsorption mechanism relatively well understood, much information was gained pertaining to the conventional part of the nuclear ground state wave function. That is, only the low momentum components of the nuclear wave function are required to explain the nuclear structure of the various low energy excitation modes of the nucleus. As the photon energy increases, above approximately 40 MeV, the long wavelength approximation used to derive the effective charges is no longer valid and therefore provides an inadequate solution to the experimental observations [16, 17, 18, 19, 20, 21].

In the energy region from above the GDR to approximately 100 MeV, the wavelength of the photon is typically smaller than the nuclear radius. Therefore it was assumed that the photon would interact with either a single nucleon or a small subgroup of nucleons within the nucleus. Since the photon was expected to interact with a single nucleon or small subgroup of nucleons, study of the shell model seemed the ideal way to try to understand the photoabsorption reaction mechanism. The success of this formalism in other fields of research in nuclear physics, such as in the (p,2p) [22, 23] and (e,e'p) [24] reactions, yielded vital information on nucleon separation energies from the various shell model orbits as well as the momentum distributions of the nucleons in these various shells. This single particle theory assumed that the struck nucleon was only weakly interacting with the rest of the nucleus, so that the recoil A-1 nucleus was thought to be a spectator in the reaction. Such an assumption is known as the impulse approximation (IA) and it has resulted in a wealth of nuclear structure information. Regarding these two quasifree scattering processes, it was discovered that less ambiguous information about the nuclear states could be obtained

using the (e,e'p) reaction. This is due to the fact that there is only one strongly interacting particle in the final state, so that final state interactions (FSI) of the nucleon as it exits the nucleus are of less importance. However, these two reactions probe only the lower momentum components of the single particle wave function (as high as 1.5 fm^{-1}).

Unlike the (p,2p) and (e,e'p) reactions, the photoabsorption process has a large momentum mismatch between the momentum carried by the incoming photon and the momentum of the ejected high energy nucleon. In this area would be an opportunity to investigate the high momentum components of the distribution, far above the Fermi level. Photoabsorption measurements were thought to be a unique tool to probe more exotic parts of the nuclear wave function by exploring such properties as the high momentum components of the nuclear wave function, short-range correlations, clustering, and non-nucleonic degrees of freedom such as meson-exchange currents and nucleon isobars. Calculations involving the plane wave impulse approximation (PWIA) and distorted wave impulse approximation (DWIA) have been used to qualitatively understand the measured yields of photoprotons for photon energies up to about 100 MeV. In such calculations, extreme caution must be taken to remove spurious contributions due to orthogonality violation, antisymmetrization, recoil effects and the effects of FSI of the outgoing nucleon. Since the neutron has no charge, the photoneutron interaction cross section is proportional to the magnetization current term only, which appears in the PWIA and DWIA calculations. Therefore, the yield of neutrons is predicted to be significantly less than the yield of protons in contrast to the experimental measurements [16, 17, 18, 19, 20, 21].

The similarity in the proton and neutron cross sections is explained when the nucleon correlations within the nucleus are considered. In this model, the photon is assumed to interact with a correlated nucleon pair within the nucleus, resulting

in one nucleon being ejected, carrying all the available energy of the reaction. The other nucleon remains bound, absorbing the large momentum mismatch implied in the photoabsorption process. Using this hypothesis, it is possible to explain the near unity ratio for the (γ,p)/(γ,n) cross sections that leave the nucleus in the ground state or low-lying excited state of the residual nucleus (except for the more forward angles). This model could also explain the near unity ratio between the (γ,p)/(γ,n) continuum cross sections which are found at high excitation energies of the residual nucleus. The continuum yield occurs as a result of removing nucleons from non-valence shells, thereby leaving the residual nucleus in a highly excited state. It should be noted that the continuum yield is known to result primarily from the two-nucleon absorption mechanism for the photon energy range studied in this thesis. The near equal yields of the continuum neutrons and protons were first studied by Levinger in 1951. In this so-called quasideuteron (QD) mechanism, the photon is absorbed by a correlated proton-neutron pair within the nucleus. The cross section for the emission of high energy photonucleons is related to the photodisintegration of the deuteron multiplied by the effective number of proton-neutron pairs within the nucleus and by the Levinger constant, which accounts for the higher momentum components of the bound QD compared to the lower momentum components of the free weakly bound deuteron. Early experiments [25, 26, 27, 28, 29] verified Levinger's prediction. With growing support for this phenomenological model, Gottfried [30] reworked Levinger's original model, which only predicted the total cross section, to a more fundamental form which could predict the angular correlation of the emitted pair, the proton and neutron emission cross sections differential in the solid angle and energy of the emitted nucleons, along with other observables of the reaction.

The relative strengths of the possible quantum numbers influencing the behavior of the two-nucleon absorption cross section are included in the various two-nucleon

absorption models in an *ad hoc* way. As an example, consider the commonly used zero-range approximation applied to the phenomenological QD model for two nucleons bound in the p-shell orbitals in ^{16}O. The zero-range approximation restricts the relative angular momentum between the pair to be s-wave or $l = 0$. A further assumption that the isospin of the absorbing pair is $T = 0$ and the spin is $S = 1$, as in the deuteron case, now restricts the orbital angular momentum transfer to the spectator ^{14}N to be L=0,2, with L=1 being ruled out via parity conservation of the nuclear force, for the two p-shell nucleons. The relative strength of the angular momentum transfer to the residual nucleus can be set by using shell model wave functions derived from phenomenological nuclear potentials which are usually normalized to the experimental data [11]. In a somewhat more thorough treatment of the calculations, the relative strength of the angular momentum transfer to the residual nucleus can be predicted by the application of sum rules, so that a more meaningful comparison between the results of the calculations to the results of the experimental measurements can be made [31]. It is evident that in order to test the approximations in the phenomenological QD model and the relative importance of the quantum numbers required for input to microscopic calculations, such as the recent calculation by Ryckebusch *et al.* [5], measurements to discrete states in the recoil nucleus of known structure (spin, parity, isospin and angular momentum transfer to the recoil nucleus) are required.

It is the goal of the present experiment to examine the reaction mechanisms involved in the photoabsorption process for the photon energy range of 60 to 140 MeV. A PWIA model will be compared to the measured $^{16}O(\gamma,p)^{15}N_{g.s.}$ at 64 MeV, since there are several features common to most shell model (IA) calculations commonly used in nuclear physics. The present measurement examines the exclusive two-nucleon photoabsorption process in the photon energy range from 100 to 140 MeV. The mea-

surement performed was the kinematically complete $^{16}O(\gamma,pn)^{14}N_{0,1,2,..}$ reaction. If the IA formalism is applied to this reaction, then the known spin, parity and isospin of the ^{16}O target nucleus, as well as the known nuclear structure information of the recoil ^{14}N nucleus, will specify the quantum numbers involved in the two-nucleon absorption mechanism. These quantum numbers are of paramount importance to all calculations for the two-nucleon absorption mechanism. In order to be able to separate the low lying excited states of ^{14}N, a net excitation energy resolution of about 2 to 3 MeV is necessary. It has been previously demonstrated that the relative importance of the quantum numbers in the two-nucleon absorption mechanism is related to the kinematical acceptance of the phase space available for the reaction. Therefore, the quantum numbers deduced from this measurement are pertinent to the phase space which consists of a $\pm$ 7° cone about the quasifree opening angle of the proton-neutron pair (that is the opening angle expected for the free deuterium breakup, kinematically corrected for the reaction Q value).

The results of an inclusive measurement of the $^{12}C(\gamma,p)$ reaction were also analysed as part of the research for my degree of Doctor of Philosophy. Photoproton spectra were obtained for the photon energy range from 177 to 217 MeV at the laboratory angles θ_p = 51°, 81°, 109° and 141°. This inclusive data was interpreted by use of a QD model calculation. The results of this measurement are presented in detail in Appendix B. Some references to these results are made in Chapter 2 and the conclusions that can be made from the inclusive $^{12}C(\gamma,p)$ reaction are presented in Chapter 6. From the analysis of such inclusive data it is realized that only a limited amount of information can be gained from such inclusive measurements. This fact motivated the present exclusive $^{16}O(\gamma,pn)^{14}N_{0,1,2,..}$ measurement from which information on a microscopic level could be obtained for the two-nucleon absorption mechanism.

Chapter 2

Photonuclear reaction mechanisms at intermediate energies

2.1 Introduction

Reaction mechanisms for the intermediate photon energy range from 60 to 140 MeV will be discussed. Figure 2.1 depicts a universal relationship between the total photoabsorption cross section, normalized to the number of nucleons in the nucleus, versus the photon energy. Shown also in the figure is the total photoabsorption cross section for the proton. The figure clearly depicts the GDR region where collective excitations of the nucleus characterize the absorption mechanism. For a photon energy of about 300 MeV the first excited state $(J^{\pi}, T) = (\frac{3}{2}^{+}, \frac{3}{2})$ of the nucleon, known as the Δ-resonance, is reached. Here the photon wavelength is of the order of the proton radius so that it preferentially interacts with a single nucleon forming the Δ-resonance. The photon energy region between the GDR and Δ-resonance is known as the dip region. For photon energies between approximately 40 to 60 MeV, the photon momentum mismatch is not too excessive, so that the PWIA and DWIA formalisms for single nucleon knockout are commonly applied. However, as the photon energy approaches 100 MeV, the momentum mismatch between the incoming photon and emitted nucleon dictates that the photoabsorption process occur via a two-nucleon absorption mechanism. In this two-nucleon absorption mechanism, the photon is taken to interact with a correlated nucleon pair within the nucleus, so that both nucleons share the momentum and energy brought into the reaction by the photon. In the reaction the recoil A-2 nucleons are assumed to act as spectators during the absorption process. For this reason the dip region is often referred to as the quasideuteron (QD) region

in the total photoabsorption spectra.

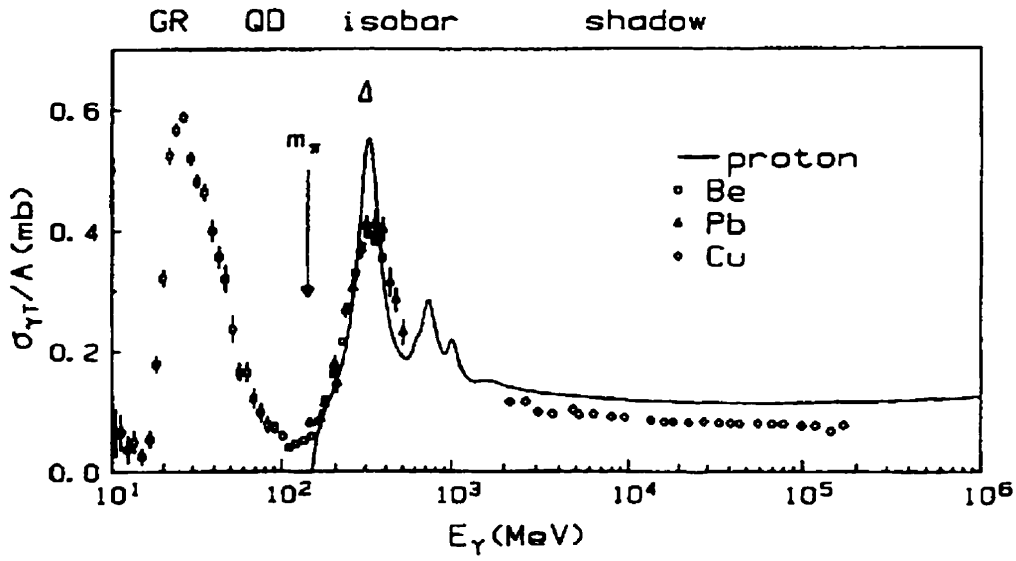

Figure 2.1: The total photoabsorption cross section per nucleon for various nuclei. The absorption spectrum is labeled by the dominant absorption mechanism occurring for each photon energy region. The energy regions depicted are: giant resonance (GR), quasideuteron (QD), Δ-resonance (isobar), and the shadow region. The figure is taken from Reference [1].

The PWIA calculation will be discussed, as it provides a useful insight to common ingredients in these calculations as well as to the problems implicit in calculations based on the IA using phenomenological shell model wave functions. The lack of high momentum components in the ground state shell model wave functions makes the direct knock-out (DKO) reaction mechanism unable to account for the relatively large $(\gamma, p_{0,1,2,..})$ cross sections for photon energies in excess of approximately 60 MeV. Compounding this problem for the DKO formalism is the fact that the photon interacts with neutrons via the relatively weak interaction with the neutron spin-current, thereby predicting a large ratio for the (γ, p) to (γ, n) yields in contrast with the experimental observations. These two discrepancies in the DKO approach are resolved by the two-nucleon absorption mechanism. The two-nucleon absorption mechanism

provides the high momentum components necessary to explain the large yields of coincident high energy protons and neutrons, and also accounts for the near equal yields of ground state protons and neutrons [18].

2.2 The direct knockout photoreaction

Assuming that the photon interacts with only one nucleon in the nucleus while the A − 1 recoil nucleus acts as a spectator, then only the one-body nuclear current operators need to be considered. Inserting the one-body nuclear current operators, which consist of an electric or convection current and a pure spin flip magnetic moment current, into the scattering matrix (S_{fi}), and performing the necessary calculations, yields to first order in S_{fi}, the laboratory differential cross section for the DKO (γ, p) and (γ, n) reactions. Such a calculation includes all multipoles of the electromagnetic field and in the PWIA predicts the laboratory differential cross section to be given by [see Appendix A]

$$\frac{d\sigma}{d\Omega} = 2\pi^2 \alpha_{em} \frac{k_N^2}{k_\gamma} \frac{dk_N}{dE_f} \Omega(q) \left[\left(\frac{k_N^2}{m^2} \sin^2(\theta_{\gamma,p}) + \frac{k_\gamma^2}{2m^2} \mu_p^2 \right) \left(\frac{1+T_3}{2} \right) + \frac{k_\gamma^2}{2m^2} \mu_n^2 \left(\frac{1-T_3}{2} \right) \right] \quad (2.1)$$

where k_N is the ejected nucleon momentum in the laboratory reference frame, k_γ is the laboratory photon energy initiating the photoreaction, α_{em} is the fine structure constant equal to $\frac{e^2}{4\pi}$ in units where $\hbar = c = 1$, $\frac{dk_N}{dE_f}$ is a kinematical factor, E_f is the total energy of the ejected nucleon and residual nucleus in the final state, $\theta_{\gamma,p}$ is the angle between the incident photon and the ejected proton, μ_p and μ_n are the anomalous proton and neutron magnetic moments respectively, m is the nucleon mass, T_3 is the z-projection of the isospin (+1 for protons and -1 for neutrons) and $\Omega(q)$ is the single particle momentum density. It should be noted that implicit in the

cross section as defined by Eq. 2.1 is a dependence on the photon energy. For an explicit detection angle and photon energy, the two body kinematics of the reaction fix the dependence of the cross section given by the term $\Omega(q)$ with a one-to-one correspondence to the photon energy. Therefore the cross section given by Eq. 2.1 is differential in the solid angle of the detected particle and in the photon energy initiating the reaction whose dependence is implicitly assumed.

The single particle momentum density $\Omega(q)$ is given by

$$\Omega(q) = \frac{2j+1}{4\pi 8\pi^3} |R_{nl}(q)|^2 \tag{2.2}$$

where j is the total angular momentum of the shell the nucleon is emitted from, and $R_{nl}(q)$ is the Fourier transform of the radial part of the wave function corresponding to the shell model state with quantum numbers (n, l, j). The additional factor of $8\pi^3$ in the denominator is to assure that the integral

$$\int N^2 |R_{nl}(q)|^2 q^2 dq = 8\pi^3 N^2 = 1 \tag{2.3}$$

is normalized to unity so that $N^2 = \frac{1}{8\pi^3}$.

Using harmonic oscillator wave functions in momentum space, one obtains for a $p_{\frac{1}{2}}$ shell nucleon in ^{16}O the following result

$$R_{01} = \sqrt{8\pi^3}\sqrt{\frac{8}{3\alpha^3\sqrt{\pi}}}\frac{q}{\alpha}e^{-\frac{q^2}{2\alpha^2}}. \tag{2.4}$$

Finally, one can write the momentum density for a $p_{\frac{1}{2}}$ nucleon in ^{16}O as

$$\begin{aligned} \Omega(q) &= \frac{2j+1}{4\pi 8\pi^3}|R_{01}|^2 \\ &= \frac{2j+1}{4\pi}\frac{8}{3\sqrt{\pi}}\frac{q^2}{\alpha^5}e^{-\frac{q^2}{\alpha^2}} \end{aligned} \tag{2.5}$$

where j is equal to $\frac{1}{2}$ and $\alpha = 0.55\text{fm}^{-1}$ is the harmonic oscillator parameter found to reproduce the root-mean-square charge radius for ^{16}O of 2.73 fm [32].

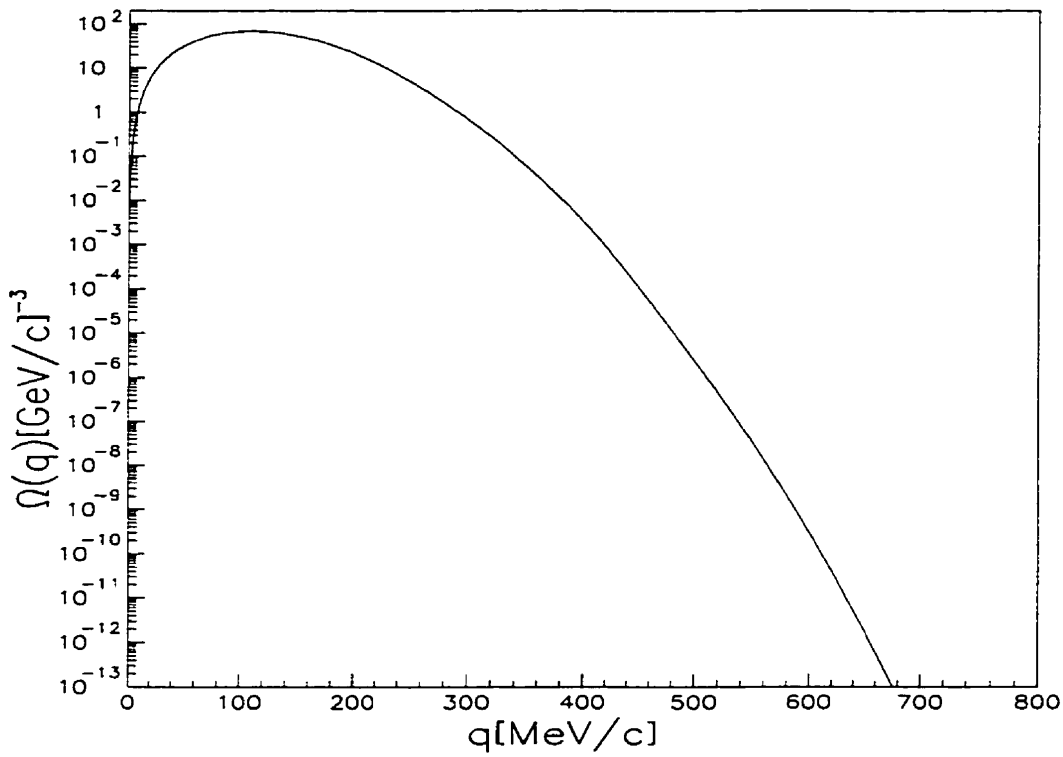

Figure 2.2: The calculated single-particle momentum density $\Omega(q)$, in $[\text{GeV/c}]^{-3}$, versus the momentum of the bound proton in MeV/c. The curve has been calculated for a $1p_{\frac{1}{2}}$ proton in ^{16}O and the oscillator parameter α was 0.55 fm^{-1}.

In Eq. 2.1 the PWIA single-nucleon cross section is seen to scale linearly with the single-nucleon bound-state momentum density $\Omega(q)$. The proton momentum density

constructed in the PWIA or the DWIA is known to reproduce the measured shape in the case of the PWIA calculation, and the measured shape and magnitude in the case of the DWIA calculation, for momentum components below approximately $q =$ 400 MeV/c, [33]. As is evident from Figure 2.2 above a momentum of $q = 400$ MeV/c the single particle momentum density decreases much more quickly than in the experimental data (see Reference [33] for example) and in effect the harmonic oscillator shell model wave functions are not capable of producing the predicted scaling of the measured cross section with the momentum density $\Omega(q)$, as given in Eq. 2.1.

A more recent $^{16}O(\gamma, n_0)^{15}N$ measurement [34] using tagged photons confirmed the old bremsstrahlung measurements of the near equality of the (γ, p_0) to (γ, n_0) cross sections. According to Eq. 2.1, the ratio of the $^{16}O(\gamma, p_0)^{15}N$ to the $^{16}O(\gamma, n_0)^{15}N$ cross sections, at the laboratory angle of 90°, and for a photon energy of 100 MeV, is given by $2k_p^2/k_\gamma^2\mu_n^2 + \mu_p^2/\mu_n^2$. This gives the predicted ratio of the (γ, p_0) to (γ, n_0) cross sections to be about 10.9 in contrast to the experimental findings.

The apparent failure of reaction models based on the independent particle motion (IPM) for the bound nucleons, is qualitatively not too surprising. It has been noted by degli Atti [35] that for a photon energy of 100 MeV the reduced photon wavelength ($\frac{\lambda}{2\pi} \approx 2$fm) is of the order of the nuclear radius. The author comments that it is very difficult to reconcile such a large value of the photon wavelength with a direct knock-out mechanism. On the contrary, for the quasi-elastic $(e, e'p)$ reactions the momentum transfer is of the order of $q \approx 2\text{fm}^{-1}$, implying that the reduced wavelength of the electron is $\approx$ 0.5fm, so that an IPM description for such a reaction seems more plausible.

It seems that the approximations entering into IPM calculations need to be investigated in light of the apparent discrepancy between experimental results and the theoretical predictions. Boffi *et al.* [2], in a PWIA calculation, study the effects

of orthogonality, antisymmetry and center-of-mass motion effects in direct knockout photoreactions. The transformation of lab frame variables into intrinsic and center-of-mass variables, which is the correct treatment of the CM motion, destroys the single-particle nature of the operator and introduces a recoil term. Figure 2.3 shows the effect on the magnitude of the cross section when the effects of center-of-mass motion (recoil term), orthogonality and antisymmetrization are accounted for in the PWIA calculation for the photon energies of 40, 80 and 120 MeV. For all energies, the proper treatment of the recoil term dominates the correction to the PWIA calculation reducing the PWIA result by nearly a factor of three for a photon energy of 40 MeV. It is also clearly evident that the effect of the recoil term decreases with increasing photon energy. Inclusion of orthogonality between initial and final states is also seen to be significant, with an effect that decreases with increasing photon energies. The inclusion of antisymmetry of initial and final states, to satisfy the Pauli exclusion principle for fermions, modifies the results of the calculation insignificantly once the recoil and orthogonality corrections have been applied.

In more realistic calculations, distorted wave functions are used to describe the outgoing nucleon. When dealing with such DWIA calculations, which involve energy dependent potentials, large orthogonality defects occur and their spurious contribution is difficult to remove. In an earlier paper, Boffi *et al.* [36] used a DWIA calculation to explain the (γ, p_0) measurements. They state that the orthogonality problem of the initial and final state wave functions is not relevant to their calculation. However, the recoil or CM motion terms were not explicitly dealt with and are now known to contribute significantly to the calculated cross section. Furthermore, calculations with the same bound state wave functions using different optical model parameters can make differences in the calculated cross section of up to an order of magnitude. The validity of the results of PWIA or DWIA calculations therefore seems

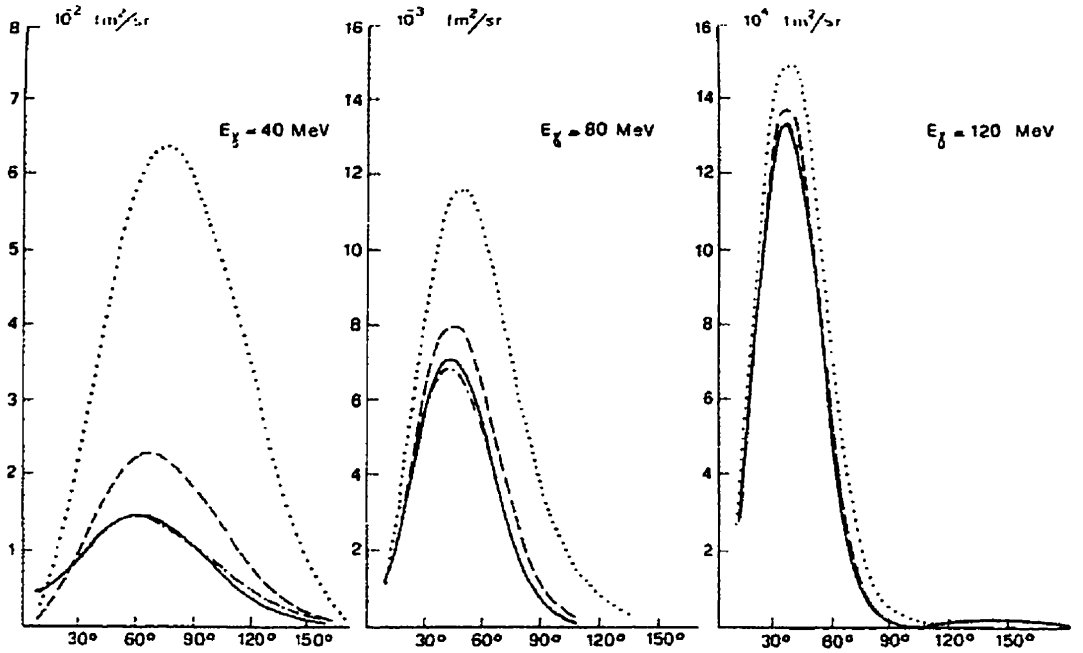

Figure 2.3: The $^{12}C(\gamma, p)$ differential cross section for the photon energies 40, 80, and 120 MeV. The PWIA calculations were performed using harmonic oscillator wave functions and neglecting the spin current contribution. The dotted line represents the results of the PWIA calculation without orthogonalization and without recoil, the dashed line without orthogonalization, the dot-dashed line contains orthogonalization, and the solid line is the fully antisymmetrized result. The figure is taken from Reference [2].

to be rather questionable unless very special care is taken to ensure orthogonality, antisymmetrization and the proper treatment of recoil or CM motion effects.

A two-step charge-exchange contribution [37] to the (γ, n) cross section resulting from a (γ, p) reaction followed by a (p, n) transition has been investigated. The charge-exchange mechanism was found to be of considerable strength. As much as a factor of two increase in the DKO (γ, n) cross section resulted if the charge-exchange mechanism was included. However, this increase was not adequate, as the calculation was still nearly an order of magnitude below the experimental data. The significance of the increase in the (γ, n) cross section which resulted from the charge-exchange process was stated to be strongly dependent on the relatively uncertain isospin term in the phenomenological optical-model potential.

In an article comparing the quasielastic $(e, e'p)$ and the (γ, p) reactions, Ireland and Steenhoven [38] concluded that a scaling of the reduced cross section, which is proportional to the momentum density of the nucleons as a function of the missing momentum, does not exist between the two reaction mechanisms. The DKO calculation is able to reproduce the data reasonably well for the $(e, e'p)$ reaction. However, when the DKO calculation (in which the optical model parameters were constrained by the complete DWIA (CDWIA) analysis of the $(e, e'p)$ data) is compared to the (γ, p) measurements, the results typically are a factor of six less than the data. The authors then make an estimate of the meson-exchange-current (MEC) contribution to the reaction by multiplying their DKO calculation by the ratio of the results of a plane wave (PW) calculation incorporating Siegert's theorem, PWS, (to account for MEC's) divided by a PWIA calculation. The result of their DKO calculation multiplied by the ratio $\frac{PWS}{PWIA}$ was found to reproduce the (γ, p) data reasonably well. This phenomenological calculation suggested that MEC's contributions appear to dominate over the DKO formalism in the (γ, p) reaction. Such a significant contribution

could be very useful in the understanding of the near equivalence of the (γ, p) to (γ, n) cross sections. A more recent relativistic DKO calculation [39] was found to be able to reproduce the (γ, p) data to within a factor of two. This implies that MEC are perhaps not as dominant in the (γ, p) reaction as predicted by Ireland and Steenhoven. If this is the case, the ability to explain the ratio of the (γ, p) to (γ, n) cross sections requires further theoretical investigation.

2.3 Two-nucleon absorption mechanisms in nuclear physics

In Appendix B, a previously measured $^{12}C(\gamma, p)X$ reaction for the photon energy region 177-217 MeV at various laboratory angles is presented. The results of the measurement are discussed in the framework of a QD model with the inclusion of a phenomenological treatment of the final state interactions (FSI) of the ejected protons. The results are also compared with other measurements. Microscopic calculations, available up to 1994 when this analysis was completed, are also discussed in comparison to the data. Some of the results presented in Appendix B will be referred to throughout this section.

The two-nucleon absorption mechanism seems to be the prevalent interaction of light or massless bosonic probes when interacting with nuclei. Both electromagnetic radiation and pions (if the pion is absorbed so that it does not exist in the final state) have the ability to eject high energy nucleons without a significant transfer in momentum. Although pion absorption on a free nucleon is kinematically forbidden, the pion may be absorbed on a single nucleon within the nucleus. In the IA this would require single particle momentum components of typically 450 MeV/c or greater making this process extremely rare. The momentum mismatch in real photon and pion absorption interactions suggests that the energy and momentum of these bosonic probes are shared by at least two nucleons. For the case of virtual photons created in

electron scattering experiments the momentum and energy transferred to the nucleus can be varied independently. When the electron transfers little energy but significant momentum to the nucleus the reaction proceeds by a DKO reaction. Electron-nucleus reactions satisfying this kinematical constraint are referred to as the quasi-elastic reactions. As the momentum and energy transfer of the virtual photon approaches the photon point ($\vec{p}^2c^2 \approx E^2$) ,the four momentum transfer approaches zero. As in the real photon case, a large momentum mismatch exists, so that the energy and momentum of the photon will preferentially be absorbed by two or more nucleons within the nucleus.

It was the very pronounced forward peaking in the angular distribution of high energy photoprotons which yielded the first indication that the photon was absorbed by a small subunit in the nucleus rather than by the nucleus as a whole. Taking into consideration the momentum mismatch between the photon and the emitted high energy proton, Levinger [40] first postulated that the photon would be absorbed by a correlated proton-neutron pair within the nucleus. He justified his assumption qualitatively as follows. If a nucleon is much closer to its neighbour than the average internucleon spacing of 1.2 fm, then it is highly unlikely that a third nucleon will be also in such close proximity. He therefore realized that it would be only two strongly interacting or correlated nucleons which would share in absorbing the energy and momentum of the absorbed photon. Next he considered the type of radiation which would mediate the interaction. Levinger noted that for photon energies up to approximately 200 MeV, the photodisintegration of deuterium is predominantly electric dipole in nature. He therefore assumed this would also be the case for the bound two nucleon system. Previously, Bethe [41] had demonstrated that a proton-proton and a neutron-neutron system possess no electric dipole moment. His proof was based on the use of effective charges and he demonstrated that a system which

consists of particles with all the same charge-to-mass ratio could not have a separation of the charge with respect to the center-of-mass and therefore the dipole moment would vanish identically. Levinger therefore predicted that high energy photons would be absorbed by a correlated proton-neutron pair within the nucleus and so the QD mechanism was founded.

With growing support for the two-nucleon absorption mechanism Gottfried [30] reworked Levinger's original formalism into a somewhat more microscopic form. Within the IA he derived the cross section differential in both the proton and neutron momentum and solid angle as

$$d\sigma = (2\pi)^{-4} F(P_{qd}) S_{fi} \delta(E_f - E_i) d^3k_n d^3k_p. \tag{2.6}$$

The cross section is given as the product of three factors. These are: the available phase space; the probability for finding a correlated proton-neutron pair with momentum P_{qd} and zero separation (that is, the pair are restricted to be in a relative S state) in the Slater determinant; and S_{fi} is the sum of the squares of the matrix elements evaluated in the center-of-momentum frame defined by the two ejected nucleons. A more detailed description of Eq. 2.6 is given in Appendix B. For closed shell nuclei, the sum over the magnetic quantum numbers can be performed so that S_{fi} can be replaced by the elementary deuterium cross section evaluated in the center-of-momentum frame of the ejected nucleons. Gottfried notes that the angular correlation of the emitted nucleons is driven by the form factor $F(P_{qd})$ with S_{fi} being only a small perturbation to the angular correlation. He did however believe that there should be a measurable effect due to the variation in S_{fi}. Eden *et al.* [3] evaluated the angular correlation cross section using first the experimentally measured deuterium cross

section, and then repeating the calculation assuming a constant cross section. The results show that there is an almost unmeasurable difference in the angular correlation function, except perhaps when the opening angle is equal to the quasifree opening angle of the pair.

The measured $^{12}C(\gamma,p)X$ cross sections presented in Appendix B are compared with the QD code of Eden using the real deuterium differential cross section and an isotropic cross section. The results are presented in Figure 2.4 and indicate that both calculations predicted virtually the same angular distribution. Apparently the choice of using off-shell cross sections for the photon energies studied, and for the interaction at a specific laboratory detection angle, results in averaging over such a large photon energy range and angular range of the deuterium cross section, that all information about the deuterium cross section is washed out.

The calculation and normalization of the calculation is described in detail in Appendix B. The results of the QD model calculation with the inclusion of FSI's fit the data well at the backward angles; however, they consistently underpredict the measured cross sections at the more forward angles (by nearly a factor of two at the most forward angle investigated). In order to fit the data at forward angles, another absorption mechanism capable of producing a large yield of forward peaked, high momentum protons is necessary. This mechanism would also have to be of significant strength to explain the measured cross sections. The required large yield and the high nucleon energies involved surely rule out a three-nucleon absorption mechanism. The use of off-shell cross sections in the QD model predicts the same results as those obtained by using an isotropic deuterium cross section for both comparisons of the QD predictions made above. This demonstrates that in such a model only information on the less interesting momentum distribution of the pn pair within the nucleus could be gained from inclusive measurements as well as the exclusive angular correlation

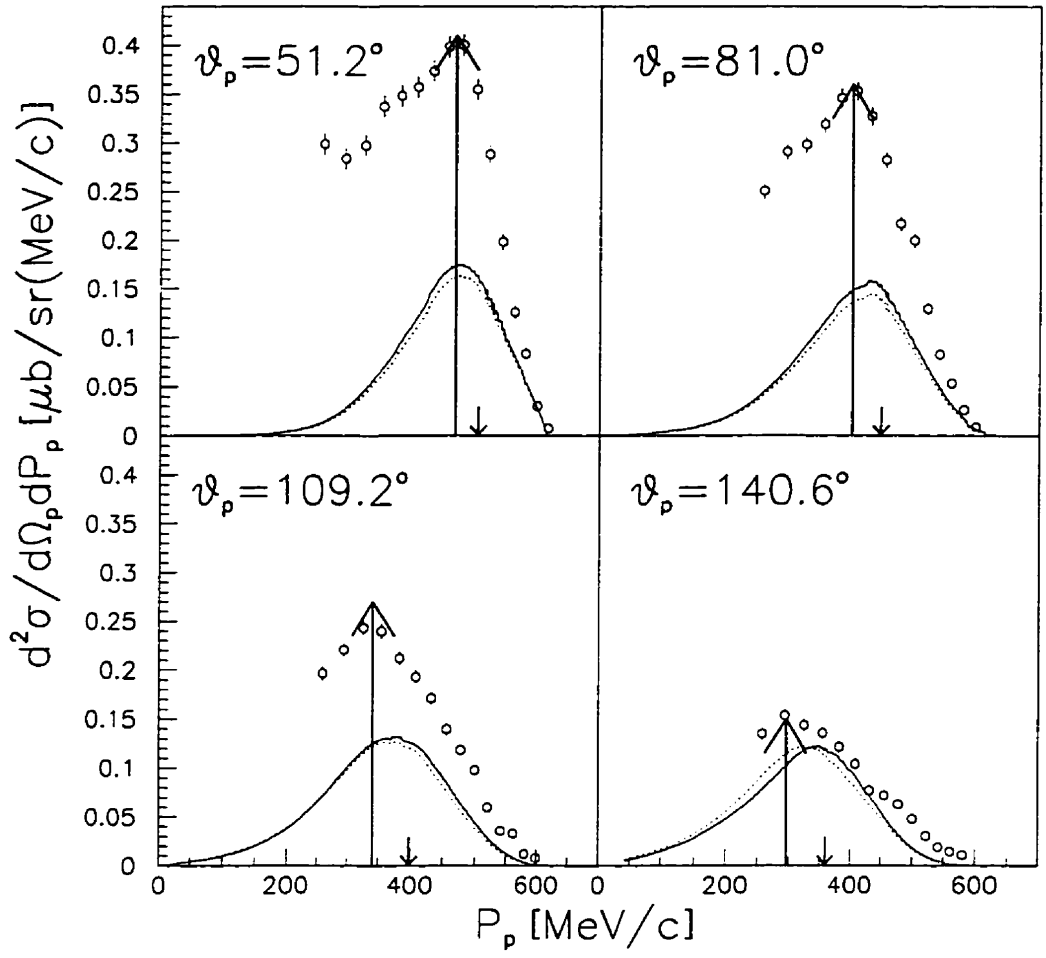

Figure 2.4: Proton momentum spectra for the photon energy range 212.6 ± 4.5 MeV at all four proton detection angles. The solid curves in the figure are the results of the quasideuteron calculation of Reference [3] when the experimentally measured angular distribution for the deuteron was used. The dashed curves are the results of the same calculation when an isotropic angular distribution for the deuterium cross section was assumed. The normalization of the calculation using the free deuterium cross section was obtained by setting the Levinger constant L = 4.9. The normalization of the isotropic calculation was such that at $\theta_p = 141°$ the two calculations predicted equal strength for the cross section. The height of the arrows in the figure is proportional to the d(γ, p)n laboratory cross section $(d\sigma/d\Omega_p)$ for $E_\gamma = 208$ MeV [4] when normalized at 51°. The small downward arrows represent the proton momentum expected for the free deuterium photodisintegration kinematics.

measurement, with little or no information on the more interesting S_{fi} terms.

However, use of the off-shell deuterium cross section does not in fact explain the measured angular photoproton distributions. In Figure 2.4, the height of the QD peak is shown to be remarkably well reproduced by the on-shell deuterium cross sections. If the form factor $F(P_{qd})$ is used to generate the phase space or momentum distribution of the absorbing pair and the on-shell deuterium cross section is used for each angle, then the two nucleon absorption part of the inclusive proton spectrum can be well reproduced by the QD model.

Ryckebusch *et al.* [5] use a nonrelativistic microscopic calculation to describe the inclusive (γ, p) and the exclusive (γ, pn) reactions. They assume the IA and use shell model wave functions. The FSIs are accounted for by an optical model approach, where care is taken to ensure orthogonality between the initial and final states. They compare the results of their calculation with an inclusive $^{12}C(\gamma, p)X$ measurement for E_γ =123 MeV. For this photon energy the (γ, p) yield is expected to result primarily from the absorption of the photon on two-nucleon currents. Figure 2.5 shows the result of the calculation in comparison to the measured data [5]. The calculation gives a fair account of the measured strength at backward detection angles; however, it consistently underpredicts the measured cross section as the detection angle decreases. At the most forward angle measured, $\theta_p = 57^o$, the calculation under-predicts the measured cross section by more than a factor of two. Ryckebusch *et al.* comment that the missing strength in the cross section at forward angles results from absorption mechanisms other than two-body and suggest that a three-body mechanism will account for the missing strength. However, in order to account for the missing yield, a three-body mechanism would have to have more strength than that resulting from their two-body absorption calculation. Surely such a large three-body mechanism would have been identified in previous experiments. Furthermore,

the phase space available to a three-nucleon absorption mechanism would favour more backward detection angles where the nucleons are less energetic. FSI's such as quasielastic $(p, 2p)$ would tend to shift the yield of the more energetic nucleons detected at forward angles to the more backward detection angles where the phase space is able to accommodate protons so degraded in energy. That is, protons at backward detection angles are typically kinematically forbidden to undergo a FSI and as a result are not likely to be detected in the two-nucleon absorption phase space at more forward detection angles.

In Fig. 2.6 the measured inclusive $^{16}O(\pi^+, p)X$ cross sections [8] for $T_\pi = 116$ MeV and for various angles are presented. The spectra are compared to a pion absorption QD model which uses the on-shell elementary $^2H(\pi^+, p)p$ cross section. FSI's are taken into account using an optical model calculation to account for proton distortions in the final state. For $\theta_p = 30°$ the QD part of the spectrum is well reproduced by the calculation. The approximate 10% difference between the data and calculation can be explained as resulting from the (π^+, pn) and (π^+, pd) reactions. Mack *et al.* [8] also note that three-nucleon phase space calculations show that at forward angles the two-nucleon absorption peak is well separated from protons resulting from a three nucleon absorption. This is, however, not the case at backward angles. At $\theta_p = 78°$ which corresponds to the center-of-mass angle of $\theta_{p_{cm}} = 90°$ the elementary $^2H(\pi^+, p)p$ cross section is a minimum (due to the $\cos^2(\theta_{p_{cm}})$ dependence of the elementary cross section) and only about 65% of the measured yield results from a two-nucleon absorption. As the detection angle increases the calculation seems to increasingly underpredict the measured cross section. This can be understood qualitatively by the arguments presented in the previous paragraph.

Figure 2.7 depicts experimental results [9] of the missing energy spectra for the $^{16}O(\gamma, pn)$ and the $^{12}C(\gamma, pN)$ reactions. The yields have been corrected for the

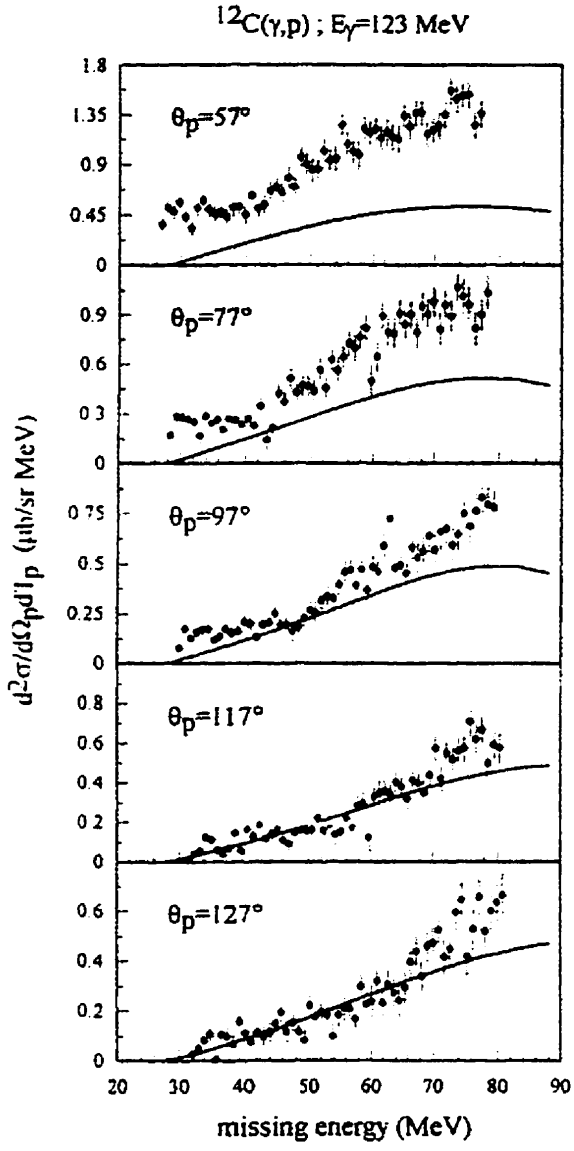

Figure 2.5: The double differential cross sections for the $^{12}C(\gamma,p)X$ cross section are shown for various laboratory angles. The curves represent the results of the microscopic calculation of Ryckebusch *et al.* The calculation used the IA with respect to the recoil ^{14}N nucleus. Distortion of the outgoing protons in the final state has been accounted for. The figure is taken from Reference [5].

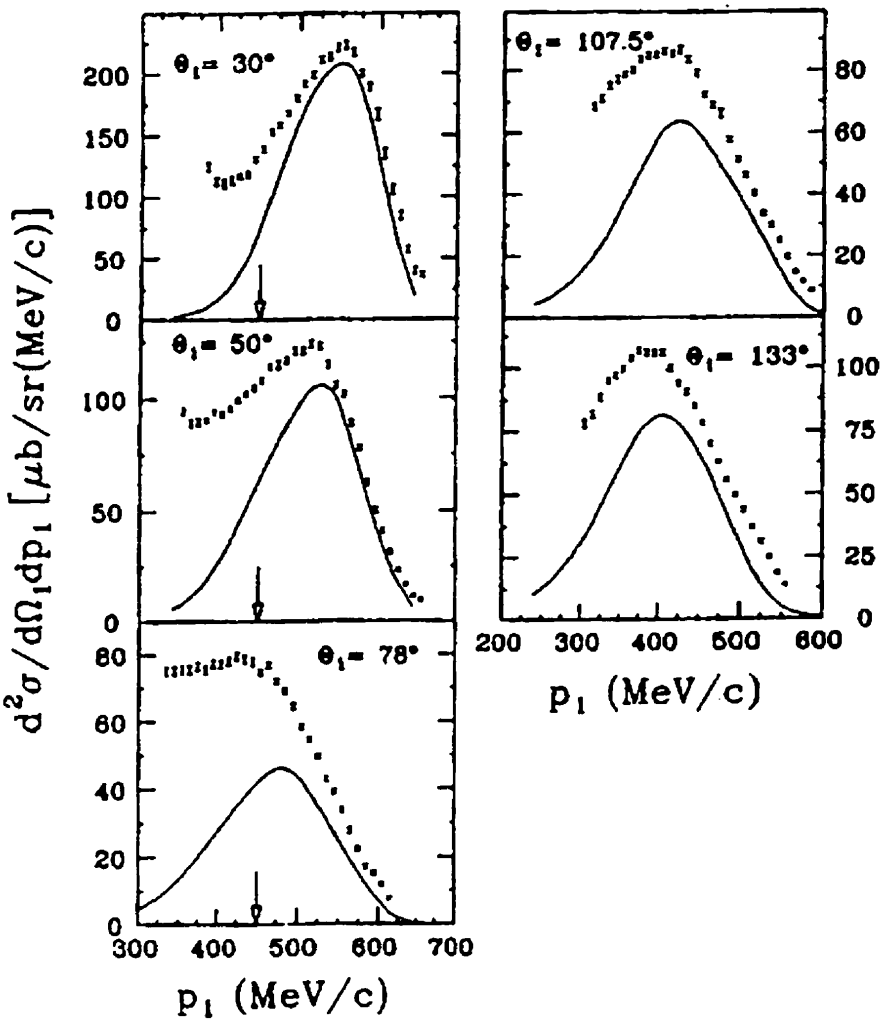

Figure 2.6: The inclusive $^{16}O(\pi^+, p)X$ double differential cross sections are displayed for various laboratory angles. The curves are the result of a DWIA calculation based on a factorized form of the QD model derived by Chant and Roos [6]. This calculation uses the wave functions derived by Cohen and Kurath [7]. An optical potential was used to simulate the distortions of the outgoing protons in the final state. The figure is taken from Reference [8].

neutron detection efficiency. Of particular interest to the current measurement is the $^{16}O(\gamma, pn)$ result. The missing energy resolution for this measurement was 7 MeV full width half maximum (FWHM). The measurement covered a considerable fraction of the 4π solid angle. The results show a strong peak with a FWHM of about 14 MeV which occurs at an excitation energy of about 5 MeV. MacGregor *et al.* [9], interpret this as meaning that several of the low lying states in the residual ^{14}N nucleus must be populated. Due to their large phase space acceptance [9], this result is consistent with the results of the pion absorption experiment of Reference [11].

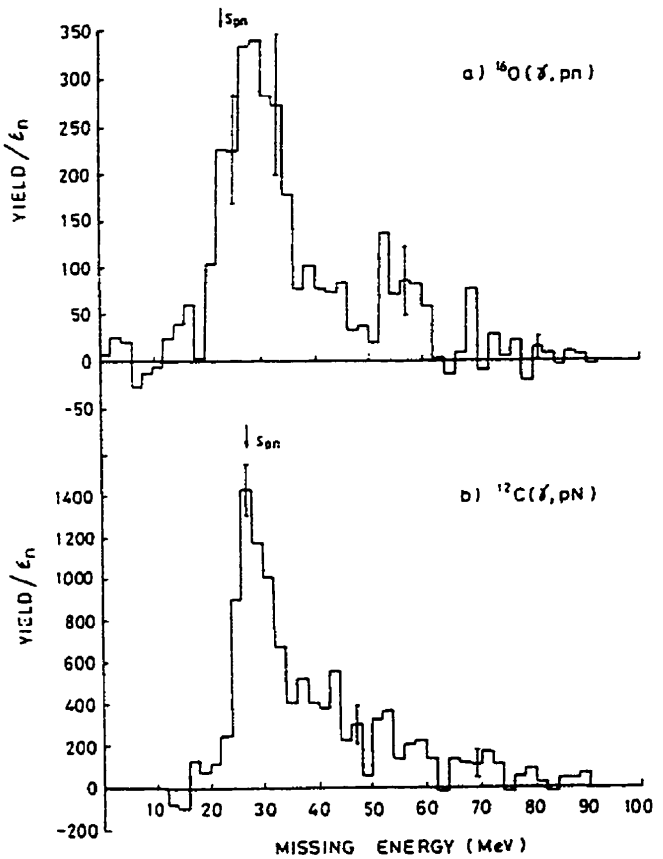

Figure 2.7: Missing energy spectra for a) the $^{16}O(\gamma, pn)$ reaction and b) the $^{12}C(\gamma, pN)$ reaction. The photon energy was 83-131 MeV and the yields have been corrected for the neutron detection efficiency. The figure is from Reference [9].

For both photon absorption and pion absorption processes, at intermediate en-

ergies, the two nucleon absorption mechanism has been verified to be the dominant reaction mechanism as is demonstrated by the experiments referenced in this section. Although microscopic models exist, experimental results are normally compared with the phenomenological quasideuteron (QD) model. The pion absorption data is reasonably well explained by the QD model where they use the on-shell deuterium cross section. It was demonstrated that the QD model, applied to the inclusive photoabsorption measurement presented in this section, does not predict the magnitude of the measured cross section when the off-shell deuterium cross sections are used. This result needs further theoretical investigation. The goal of the present experiment is to compliment the available data by making a high resolution measurement to separate the residual excited states of the recoil nucleus in order to obtain explicit information about the two nucleon absorption reaction mechanism.

2.4 The coupling scheme and the structure of ^{14}N

The purpose of this experiment was to make a kinematically complete measurement of the $^{16}O(\gamma, pn)^{14}N_{0,1,2,..}$ reaction with sufficient energy resolution to be able to separate the low lying excited states from the ground state of the ^{14}N nucleus. The spin (J), parity (π) and isospin T of the ground state of the ^{16}O nucleus are known to be $(J^{\pi}, T) = (0^{+}, 0)$. In the IA or spectator model, the coupling of the quantum numbers of the absorbing proton-neutron pair and the recoil nucleus to the quantum numbers of the ^{16}O nucleus can be obtained only if the quantum numbers for the pair are identical to those for the residual ^{14}N nucleus as will be proven below. Therefore, if the quantum numbers of the recoil ^{14}N nucleus are known, the quantum numbers for the absorbing proton-neutron pair can be uniquely determined.

To identify the two-nucleon components of the shell-model configurations, the total spin $\vec{J}_{pn}$ of a proton-neutron pair with individual angular momenta $\vec{j}_1$ and $\vec{j}_2$

can be written as

$$\vec{j}_1 + \vec{j}_2 = \vec{J}_{pn} = \vec{S} + \vec{L} \tag{2.7}$$

where $\vec{S} = \vec{l} + \vec{s}$, $\vec{s}$ is the spin of the nucleon pair ($=\vec{s}_1 + \vec{s}_2$), $\vec{l}$ is the relative orbital angular momentum of the pair and $\vec{L}$ is the orbital angular momentum characterizing the center-of-mass motion of the pair. The parity of the nucleon pair is determined by

$$\pi_{pn} = (-1)^l(-1)^L. \tag{2.8}$$

In the spectator model, isospin, angular momentum and parity impose the following relations for the quantum numbers of the proton-neutron pair which absorbed the photon.

$$\begin{aligned} \vec{T}_{pn} + \vec{T}_R &= \vec{T}_T \\ \vec{J}_{pn} + \vec{J}_R &= \vec{J}_T \\ \pi_{pn}\pi_R &= \pi_T \end{aligned} \tag{2.9}$$

where the subscripts R and T refer to the recoil and target nuclei, respectively. Inserting the known spin, parity and isospin of the ground state ^{16}O nucleus into Eq. 2.9

yields the following relationships

$$\begin{aligned} \vec{T}_{pn} + \vec{T}_R &= 0 \\ \vec{J}_{pn} + \vec{J}_R &= 0 \\ \pi_{pn}\pi_R &= +1. \end{aligned} \tag{2.10}$$

Therefore the relationships between the quantum numbers of the proton-neutron pair and the recoil ^{14}N nucleus in the IA are

$$\begin{aligned} \vec{T}_{pn} &= \vec{T}_R \\ \vec{s} + \vec{L} + \vec{l} &= \vec{J}_R \\ (-1)^l(-1)^L &= \pi_R. \end{aligned} \tag{2.11}$$

The Pauli principle requires the total two-nucleon wave function to be antisymmetric under the exchange of the two particles. As in the case of the deuteron wave function, this condition applied to the space, spin and isospin parts of the wave function requires that

$$l + s + T = odd. \tag{2.12}$$

Given in Table 2.1 are the possible quantum numbers using the angular momentum and parity relations derived above. Only low values of the relative angular momentum of the pair are given, since it is known that values of $\vec{l}$ larger than 2 do not contribute

significantly to the calculation of the cross section [6].

Table 2.1: Allowed quantum numbers for correlated proton-neutron pairs for several low lying states of the recoil ^{14}N nucleus.

$E_x =$ 0.0,3.95MeV $(J_R^\pi, T_R) =$ $(1^+, 0)$			$E_x =$ 2.31MeV $(J_R^\pi, T_R) =$ $(0^+, 1)$			$E_x =$ 7.03MeV $(J_R^\pi, T_R) =$ $(2^+, 0)$		
l	s	L	l	s	L	l	s	L
0	1	0,2	0	0	0	0	1	2
1	0	1	1	1	1	1	0	1,3
2	1	0,2,4	2	0	2	2	1	0,2,4

States in ^{14}N with the same spin and parity, J^π, may still have different internally structured wave functions. The source of this difference in the structure of the wave functions stems from the preferred orbital angular momentum transfer, L, of the proton-neutron pair leading to a discrete state of known J^π in the recoil nucleus. Various calculations and the interpretation of experimental data indicate that states of the same J^π are preferentially reached by a dominant angular momentum transfer L. This explains why states of the same J^π may be excited differently both quantitatively and qualitatively. In the present experiment, use of the theoretically and experimentally known angular momentum transfer to specific states in the recoil ^{14}N nucleus is required in order to interpret the results of this measurement. In particular, it is known [11] that for two-nucleon absorption at the quasifree opening angle of the pair, $L = 0$ transfer dominates the phase space of the reaction for this kinematical condition. The present experiment is performed in such kinematics so that $L = 0$ transfer is expected to dominate the current measured reaction.

Cohen and Kurath [7], using a phenomenological potential derived from fitting nucleon-nucleon scattering data, construct wave functions from a fit to the energy levels of 1p shell nuclei and the binding energy of each ground state with respect

to the $(1s)^4$ core. Although 4 of the 5 non-diagonal two-body matrix elements connect an orbital wave function with L=1 to a wave function of even L, the authors note that the matrix elements vanish identically for the commonly used potentials which are symmetric under the permutation of the spatial coordinates. If a zero-range approximation is assumed for the two-nucleon wave function (relative angular momentum l=0 for the pair) then only L=0 and L=2 states can contribute to the transfer in 1p shell nuclei. The spectroscopic factors [7] for strongly excited states in the $^{16}O(d,\alpha)^{14}N$ transfer reaction [10] are listed in Table 2.2. Spectroscopic factors are commonly used to scale theoretically calculated cross sections.

Table 2.2: Spectroscopic factors [7] indicating the dominant shell-model configuration for principal T=0 states which may be excited in the $^{16}O(\gamma,pn)^{14}N_{0,1,2,..}$ reaction. Also given are the factors for the T=1 state at 2.31 MeV which may also be weakly excited.

E_x				Spectroscopic factor for state with (T,L) :		
(MeV)	J^π	T	Configuration	(0,0)	(0,2)	(1,0)
0	1^+	0	$(p_{\frac{1}{2}})^{-2}$	0.016	2.704	
2.31	0^+	1	$(p_{\frac{1}{2}})^{-2}$			2.212
3.95	1^+	0	$(p_{\frac{1}{2}})^{-1}(p_{\frac{3}{2}})^{-1}$	2.675	0.081	
7.03	2^+	0	$(p_{\frac{1}{2}})^{-1}(p_{\frac{3}{2}})^{-1}$		5.0	
11.05	3^+	0	$(p_{\frac{3}{2}})^{-2}$		7.0	

The results of the zero-range distorted wave Born approximation (DWBA) calculation by Woude and Meijer [10] using the two-particle spectroscopic factors or the equivalent two-nucleon coefficient of fractional percentage [7] and one set of optical model parameters for all transitions are shown in Figure 2.8. Woude and Meijer conclude that the fit of the calculation to the experimental data for the $^{16}O(d,\alpha)^{14}N$ reaction and the $^{12}C(\alpha,d)^{14}N$ (not shown) supports that the ground state, 3.95 MeV state, 7.03 MEV state and the 11.03 MeV state in ^{14}N are reached by a predominant L = 2, 0, 2 and 2 transfer respectively in agreement with the predictions of Cohen and

Kurath. The analysis of Fleming *et al.* [42], using a zero-range DWBA calculation and an optical model to describe the distortions in the final state, when compared to their $^{16}O(p,^3He)^{14}N$ data, also concludes that the ground state, and 7.03 MeV state in ^{14}N are reached by a predominant L=2 transfer while the 3.95 MeV state is reached by a predominant L=0 transfer. It should be noted that using these theoretical calculations to extract the orbital momentum transfer, L, is in most cases very sensitive to both the choice of wave functions and the choice of the optical model potential and parameters used therein. Other transfer reactions show that there are discrepancies in these model dependent analyses when compared with the Cohen and Kurath predictions for the structure of the ^{14}N nucleus.

A complimentary measurement of the orbital angular momentum transfer with respect to the residual states in ^{14}N is supplied by the $^{16}O(\pi^+,pp)^{14}N_{0,1,2,...}$ measurement of Schumacher *et al.* [11]. Here the authors assume a Fermi gas density for the initial two-nucleon states. The IA was also assumed for the recoil ^{14}N nucleus. After Monte Carlo simulations to account for detector thresholds and acceptances, they extract the form factors for the various excited states as is depicted in Figure 2.9. Shown for comparison is an arbitrarily normalized probability density for harmonic-oscillator states with N=1, L=0 for the 3.95 MeV state and N=0, L=2 for the 7.03 MeV state. The L=0 behavior of the 3.95 MeV state is evident and well produced by the harmonic oscillator probability density. The data for the 7.03 MeV state exhibit greater strength at higher recoil momenta as expected from a L=2 transfer; however, the data do not fall to zero at low recoil momenta as is expected from the oscillator model. Schumacher *et al.* claim that the ground state exhibits characteristics between a pure L=0 and L=2 transfer. There seem to be large discrepancies between the characteristic preference of the orbital angular momentum transfer for the various states in ^{14}N and it appears that further measurements are required to see which wave functions

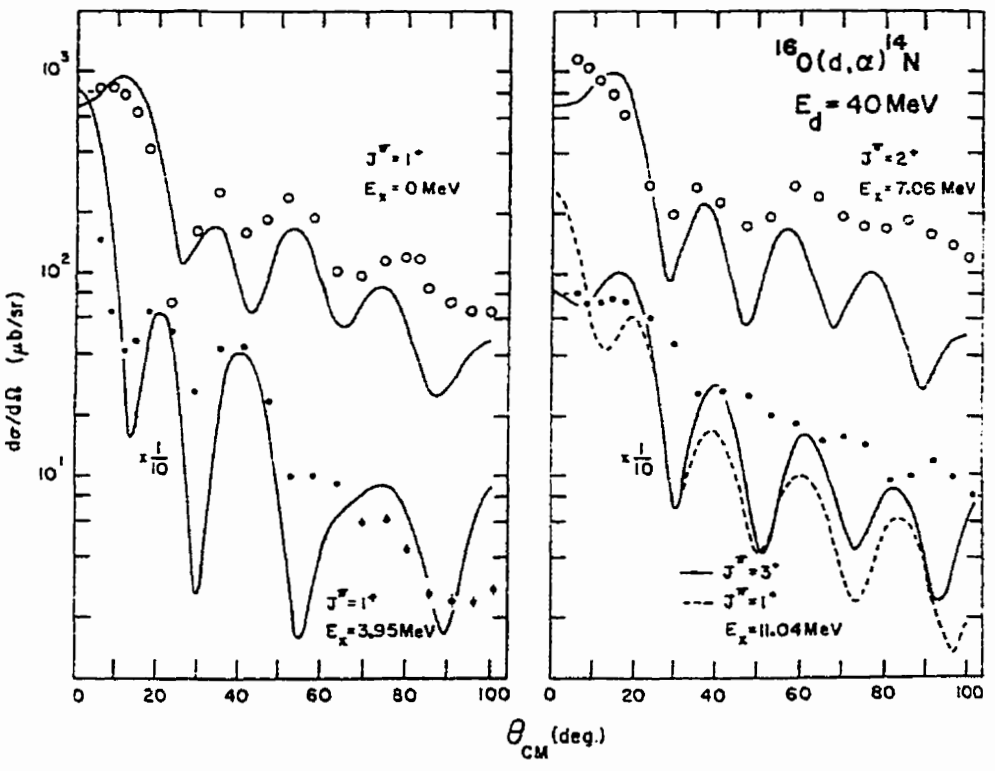

Figure 2.8: Angular distribution for selected states in ^{14}N resulting from the $^{16}O(d,\alpha)^{14}N$ reaction. The curves are the result of DWIA calculations using single particle form factors and coefficients of fractional parentage calculated by Cohen and Kurath. An optical model was used to account for the final state interactions. The figure is taken from Reference [10].

predict the correct dependence of the orbital angular momentum transfer for the ^{14}N nucleus.

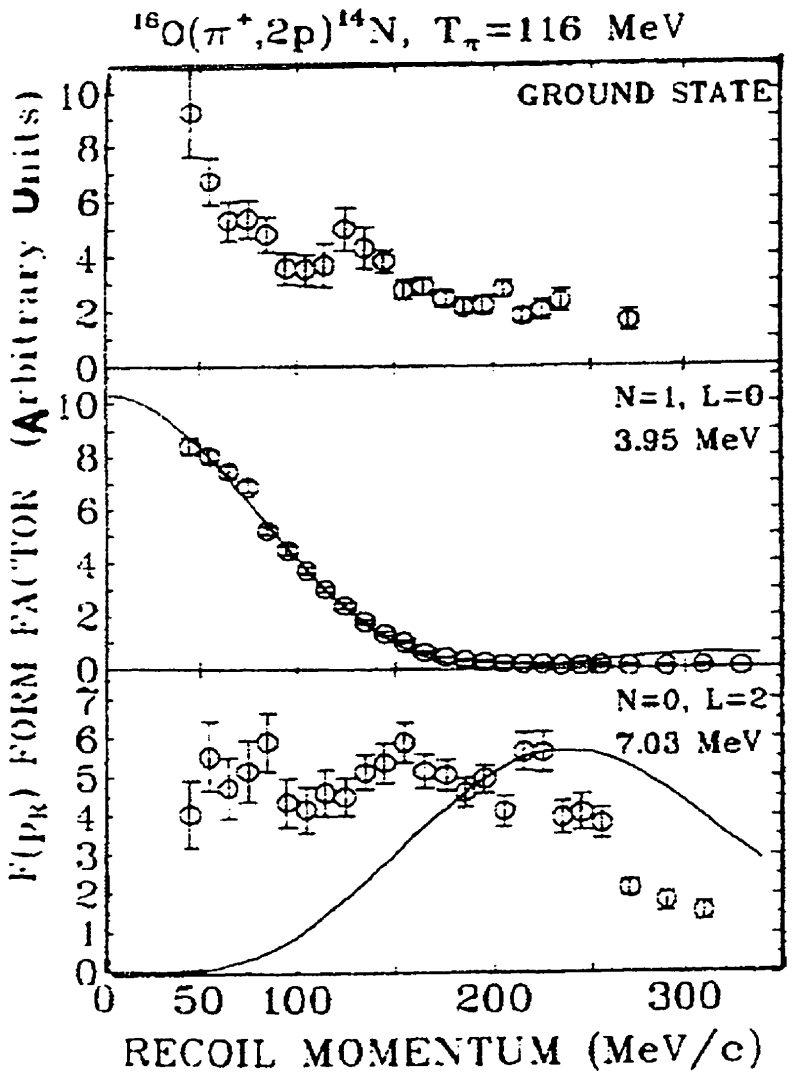

Figure 2.9: The form factor (arbitrary units) for the ground state, 3.95 MeV state and the 7.03 MeV state in ^{14}N is graphed as a function of the momentum of the recoil nucleus. The impulse approximation was assumed so that the recoil momentum of the ^{14}N nucleus is necessarily equal to the momentum distribution of the absorbing proton-neutron pair. For comparison, the predictions for the harmonic oscillator momentum space probability densities for a transferred momentum of L=0 and L=2 are displayed. The harmonic oscillator parameter was 1.17 fm. The figure is taken from Reference [11].

Chapter 3

The Experiment

3.1 Introduction

The contents of this chapter describe the photonuclear research facility and the experimental apparatus and techniques used to undertake the research presented in this thesis. The purpose of this experiment was to make a kinematically complete measurement of the $^{16}O(\gamma, pn)^{14}N_{0,1,2,..}$ reaction with sufficient excitation energy resolution to resolve the states in ^{14}N. The photon energy was determined by using the photon tagger to produce monochromatic photons. Protons were detected in high resolution CsI(Tl) detectors, while the energy of the neutrons was determined by a time-of-flight (TOF) measurement. The net excitation energy resolution, including proton energy loss in the heavy water targets, was approximately 3 MeV full width half maximum and was sufficient to resolve the excited states in the residual ^{14}N nucleus.

3.2 The facility

The research facility used to perform the experiment was the 300 MeV electron linear accelerator (linac) at the Saskatchewan Accelerator Laboratory (SAL) situated at the University of Saskatchewan. The linac is capable of producing an electron pulse of up to 1 μs in length with a repetition rate of 180 Hz. This corresponds to a duty factor of 0.018%. A recent upgrade to the linac was the implementation of a pulse stretcher ring [43] (PSR) which converts the pulsed beam of the linac into a continuous wave

(CW) electron beam. This upgrade was completed in the late 1980s and resulted in a dramatic increase in the duty factor to nearly unity. magnitude. The use of such PSRs makes possible a whole new class of low count rate coincident experiments which were not feasible with the old low duty factor pulsed machines.

The monoenergetic CW electron beam is generated in the following manner. Electrons are pulsed from a diode gun at a rate of 180 Hz. They are then accelerated through the six sections of the linac up to a maximum energy of 300 MeV. The spread in energies of the electron beam emerging from the accelerating sections is $\pm 1.0\%$ and this is then reduced to $\pm 0.1\%$ by an energy compression system [44] (ECS). Upon emerging from the ECS the electron beam is steered close to the ring orbit and then "kicked" into the PSR by electrostatic inflectors. An radio frequency (RF) accelerating section in the ring is used to keep the energy of the beam stable and to control the resonant beam extraction process. The beam when extracted from the ring has been cooled in the PSR to an energy spread of $\pm 0.01\%$. For this experiment, the duty factor was typically 70% to 80%. After extraction, the CW beam is transported to the magnetic switchyard and then into Experimental Area Number 2 (EA2). This room houses the photon tagging system used to create the monoenergetic photon beam necessary for this experiment. The layout of the experimental facility is shown in Figure 3.1.

3.3 Proton telescopes

3.3.1 Proton detectors

This double arm multiple target experiment made use of three high resolution Δ-E E telescopes. The Δ-E detector consisted of an NE-102A scintillator of dimensions 100.0 mm x 100.0 mm x 2.0 mm which was coupled to a 5.08 cm Phillips XP62

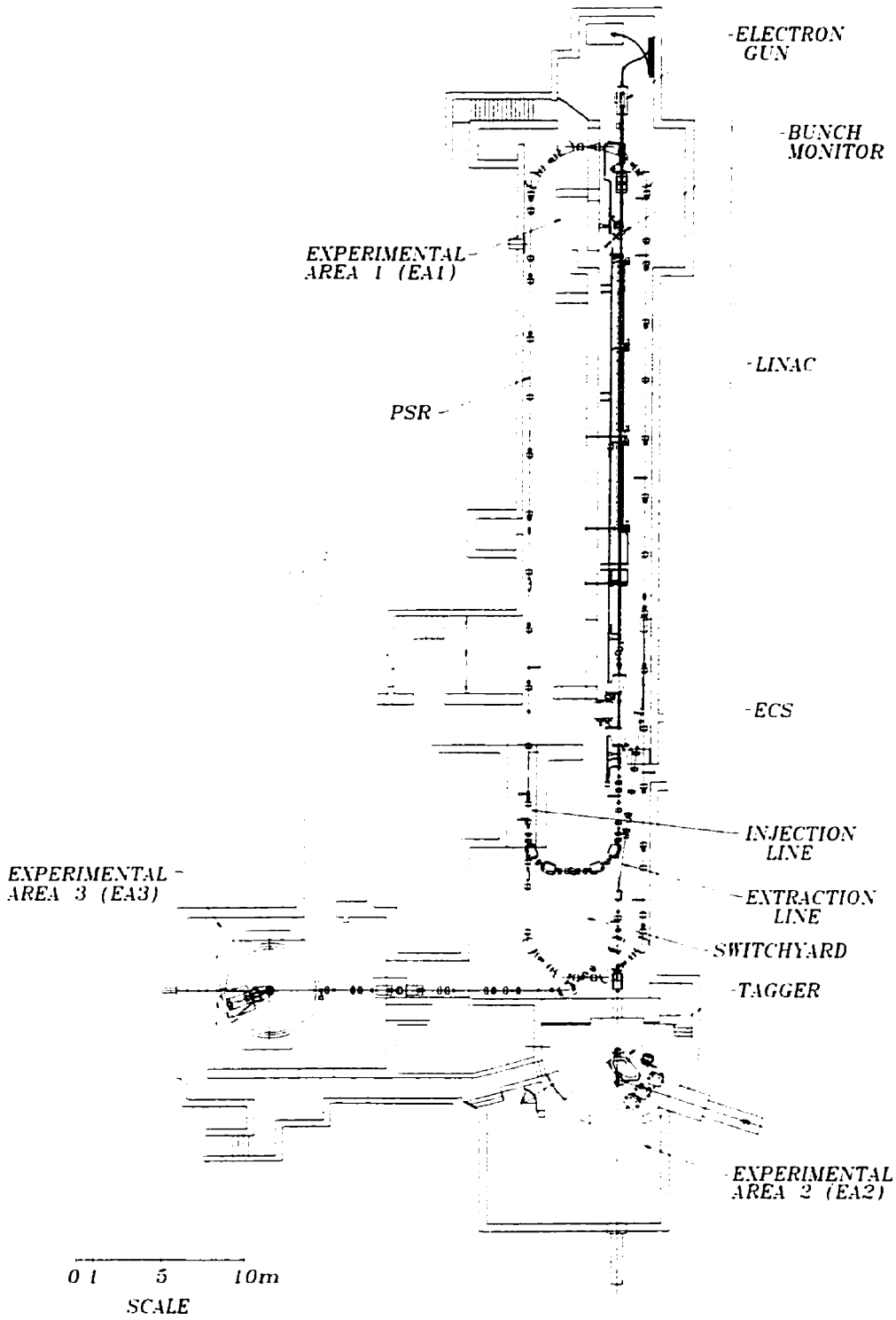

FLOOR PLAN LAYOUT OF SASKATCHEWAN ACCELERATOR LABORATORY

Figure 3.1: The Saskatchewan Linear Accelerator

photomultiplier tube with CERN bases using ultra-violet transparent Dow-Corning Q2-3067 optical gel. The 2.4 ns decay width of the scintillation light produced in the NE-102A scintillator makes it a suitable choice for most experiments where the timing resolution is of paramount importance. The start time for measuring the neutron time-of-flight was therefore derived from the Δ-E detector. The 2.0 mm thickness for the Δ-E scintillator was chosen so as to provide good particle identification in the form of a Δ-E E scatter plot while a majority of the protons to be studied would deposit most of their energy in the high resolution cesium iodide (CsI(Tl)) crystal of the E detector. The CsI(Tl) detectors used for this measurement were supplied by the University of Melbourne.

The CsI(Tl) crystal was cylindrical with a diameter of 7.61 cm and a depth of 7.61 cm. This thickness of the CsI(Tl) crystal was sufficient to stop a $\sim$ 165 MeV proton incident normally to the front face of the scintillator and the crystal therefore had adequate stopping power for even the highest energy protons encountered in this experiment. The CsI detectors were constructed by Bicron and were encased in an air-tight aluminum housing with a 4 micron aluminum window on the front face of the detector. The crystal was coupled to a 7.61 cm Burle photomultiplier tube using optical gel. The detectors were operated at a typical high voltage of -1400 Volts.

Figure 3.2 shows a front and side view of the Δ-E E CsI(Tl) telescope. The distance (in units of mm) from the center of the target to the lead collimator, Δ-E scintillator and the front face of the CsI(Tl) E detectors has been indicated. The thickness of the lead collimator was 4.4 cm and the diameter of the opening defining the solid angle was 5.0 cm.

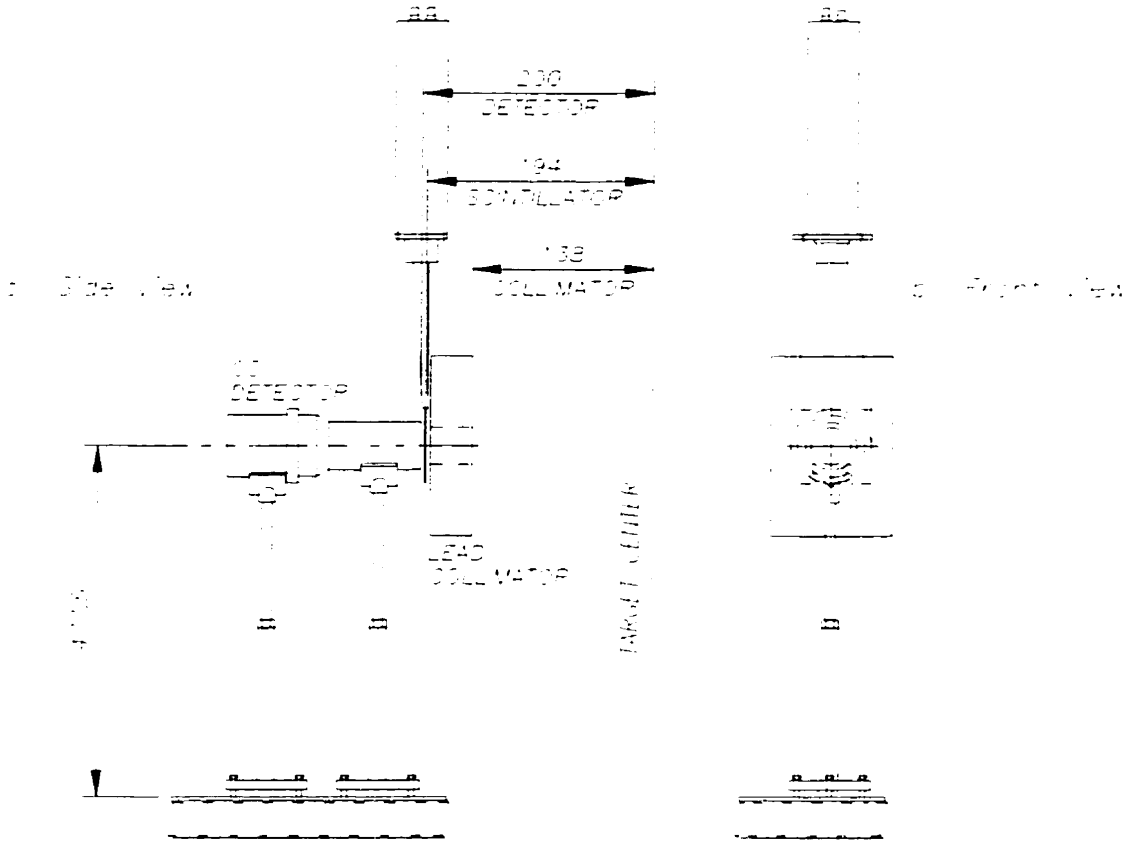

Figure 3.2: Front and side views of the proton CsI(Tl) Δ-E E telescope.

3.3.2 Pile-up

This was a one-time experiment with a fixed running time of 3 weeks. In conjunction with this the experimental set-up had a relatively limited solid angle coverage for the detection of coincident protons and neutrons and to compound this problem was the expected low count rate of the $^{16}O(\gamma, np)^{14}N_{0,1,2,3...}$ reaction. The collaboration therefore decided to run with as intense a photon flux as possible. The limiting factor in the photon flux rate was set by the intrinsically slow ($\sim$ 1μs) decay of the scintillation light produced in the CsI crystal. As the rates increased a pile-up effect was seen, as evidenced in the pedestals measured by the CsI analogue to digital

converters (ADCs). The pedestals measured by the ADCs are ideally a couple of channels in width and correspond to a zero energy measurement. A 3% loss of the proton yield leaving the residual nucleus in the discrete states under consideration, was deemed to be tolerable and was expected to be small compared to other systematic errors in the measurement. This level of pile-up was not exceeded during the course of the experiment and a corresponding correction was made to the data.

3.3.3 CsI(Tl) telescope electronics

A schematic overview of the CsI(Tl) telescope electronics is shown in Figure 3.3. The Δ-E signal is split via passive 50 ohm splitters. After the first 50 ohm split, one of the outputs is integrated by a charge integrating ADC. The other output signal is again split with one output going to a constant fraction discriminator (CFD) labeled Lo while the other output is transmitted to a CFD labeled Hi. The Lo and Hi labels for the CFD refer to the level of the analogue signal which must be exceeded at the CFD input in order for an output logic signal to be generated.

The CsI(Tl) or E-detector signal is split by a passive 50 ohm splitter. One output is charge integrated in a wide gate ADC. The other output signal is first amplified in a linear amplifier with one output going to a CFD labeled Lo while the other output is transmitted to a CFD labeled Hi. The levels of the Hi and Lo CFDs are set to produce a hardware box cut. The effect of this cut is demonstrated in Figure 4.9. At low ADC values of the E and Δ-E signals a box shape is formed, and values within this region were prevented from causing a trigger. The purpose of this cut was to reduce the copious amount of low energy particles being read out by the data acquisition computer system as well as to provide a hardware fast clear to the tagger. This enabled the trigger logic to be performed much faster than waiting the 1 μs time necessary to integrate the CsI(Tl) signal before making a decision to trigger the

electronics. If both the E and Δ-E signals were above the thresholds of the Lo CFDs then the Lo AND unit would transmit signals to a time to digital converter (TDC) as well as trigger the logic unit. If the logic unit did not have an inhibit signal from the tagger then an X-trigger was sent to the tagger. An output of this logic unit was also sent to the AND logic unit producing the hardware fast clear to the tagger electronics. If either of the Δ-E or E signals were above the CFD Hi thresholds then the OR, normally kept at a high output signal, would be transformed to a low output state. The effect is to not allow a coincidence at the AND logic unit, thereby preventing a fast clear to the tagger. If, however, neither the E or Δ-E signals were above their respective CFD(Hi) thresholds, then a coincidence would be registered at the AND logic unit and a fast clear would be sent to the tagger. This produced a hardware box cut in the Δ-E E scatter plot.

By making use of the deuterium present in the heavy water, the linearity of the electronics could be monitored on a run-to-run basis. No non-linearities were observed.

3.4 Neutron detectors

The neutron detector consisted of an array of ten bars of Bicron 408 plastic scintillator. The dimensions of each bar were 150.0 cm x 15.0 cm x 7.6 cm. Placed in front of each neutron bar was a charged particle veto detector of dimensions 150.0 cm x 15.0 cm x 0.3 cm. The neutron scintillator bars had a photomultiplier tube (PMT) coupled at each end and measured the TOF by the so-called mean timing method. A detailed description of the neutron detector has been reported elsewhere [45]. A schematic drawing of the neutron detector array is given in Figure 3.4.

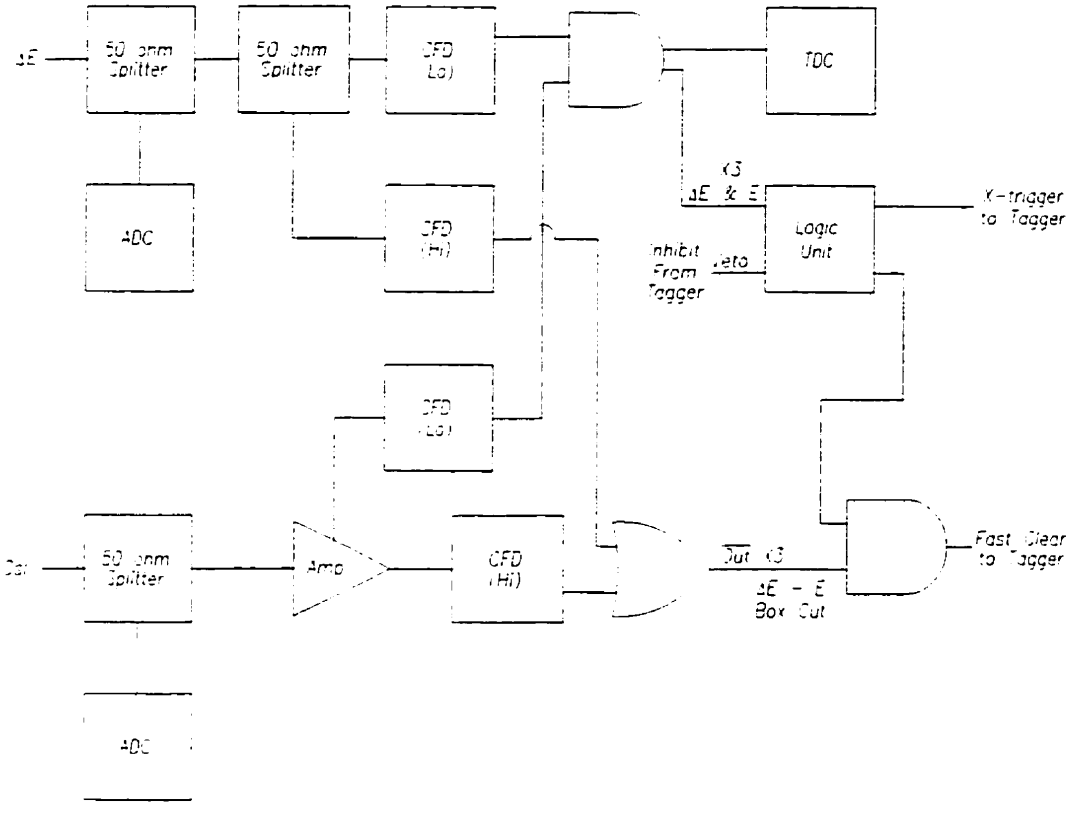

Figure 3.3: CsI(Tl) Δ-E E telescope electronics.

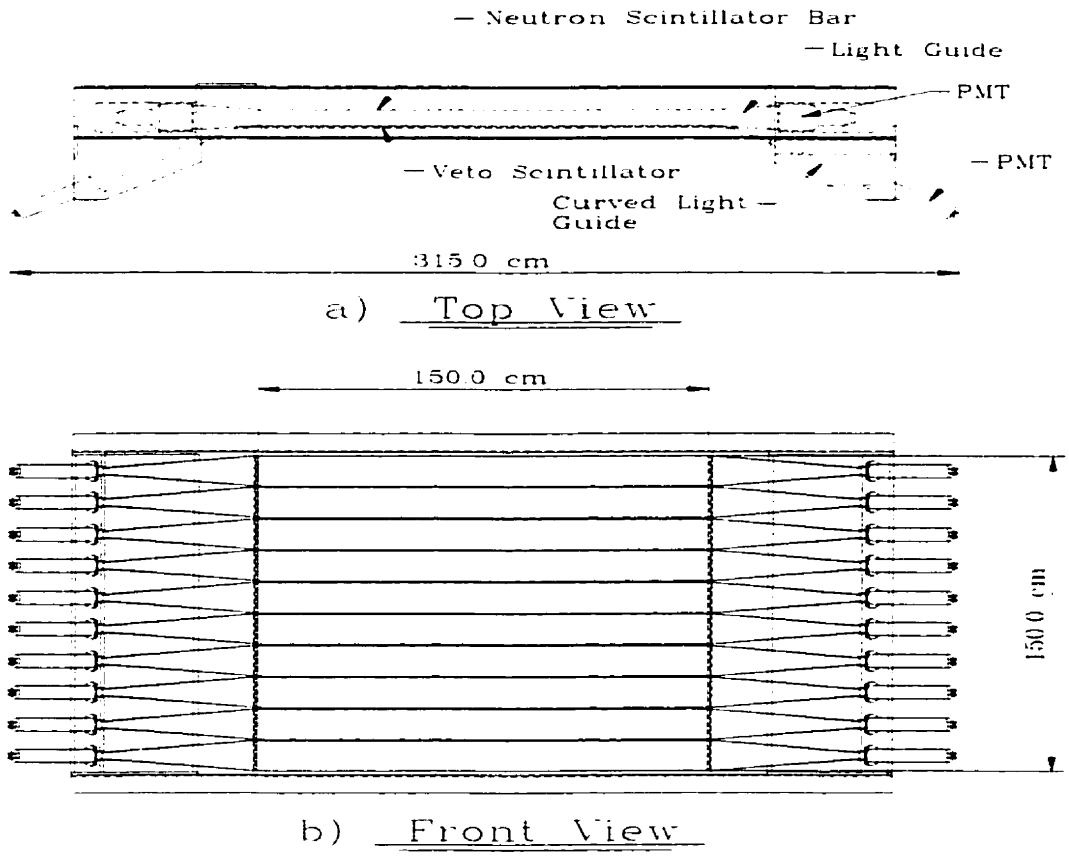

Figure 3.4: Front and side view of SAL neutron detector.

The particle TOF is then given by

$$T_{net} = 1/2(k_L TDC_L + k_R TDC_R) + f_p + Constant \tag{3.1}$$

where TDC_L, TDC_R are the TDC values (with respect to the proton Δ-E trigger signal) obtained by the left and right PMT readings respectively, k_L and k_R are the left and right TDC conversions coefficients converting the TDC channel number to time, f_p is the proton time-of-flight from the target to the proton Δ-E detector and the constant is an experimentally determined value which will be discussed in Chapter 4.

By employing the mean timing method, one obtains a factor of $1/\sqrt{2}$ better time resolution, $\sigma_{net}(TOF)$ (standard deviation of the net timing resolution), for a hit at the center of the scintillator than for a TDC signal generated by the read-out of the scintillator at only one end. The mean timing method also enables the determination of the hit position, X_D, along the length of the scintillator as given by the following equation:

$$X_D = 1/2(k_L TDC_L - k_R TDC_R)v_{eff}, \tag{3.2}$$

where v_{eff} is the effective velocity of the light propagation signal in the scintillator. The signal velocity, v_{eff}, was typically 15 cm/ns for the neutron bars and is basically dictated by the geometry of the scintillators. The standard deviation error in the determination of the hit position in the detector is given by

$$\sigma(X_D) = \sigma_{net}(TOF)v_{eff}, \tag{3.3}$$

where $\sigma_{net}(TOF)$ is given by

$$\sigma_{net}(TOF) = 1/2\sqrt{\sigma^2(T_L) + \sigma^2(T_R)}. \tag{3.4}$$

Energy resolution was of paramount importance in this experiment and the neutron energy resolution was expected to dominate the net missing energy resolution of the measured reaction. In order to optimize the neutron energy resolution obtainable via the TOF measurement, one must have a good understanding of the timing characteristics of the scintillator and PMTs. When testing the time resolution of a PMT it is desirable to have a delta-function light pulse to activate the PMT [46]. The

scintillator being used must therefore have as short a decay time as possible. Bicron 408 is an extremely fast scintillator with a decay width of 2.1 ns and so should not hinder the performance of the timing characteristics of the PMTs, although it will definitely contribute to the timing resolution obtainable. The timing obtained from the PMT is normally extracted using the rising characteristic of the output pulse (since this is typically much faster than the fall time of the pulse) so that it is more precise for fast rise times. However, the ultimate limit in a timing measurement is the pulse jitter or range of signal transit times through the PMT which is intrinsic to the PMT itself. This effect has essentially two origins. The first is the broad velocity distribution of the photoelectrons ejected from the photocathode, via the photoelectric effect, due to the characteristic range of wavelengths absorbed by the photocathode. The other effect is geometrical in that electrons ejected from different points on the photocathode must travel different distances to the first dynode. This geometrical effect dominates the timing jitter of the PMT. The contribution of these two effects to the optimal timing resolution can be minimized by applying as high a voltage as possible to the PMT. This results in larger velocities of the photoelectrons, reducing the spread of arrival times at the first dynode.

A further consideration is the number of simultaneous photoelectrons emitted by the photocathode. If N is the number of simultaneous photoelectrons emitted, then the pulse jitter is reduced by the square root of N since this is a statistical process. Both the PMT signal rise time and the number of simultaneously ejected photoelectrons improve as the high voltage is increased. It is therefore obvious that one must operate the PMT at as high a voltage as possible to obtain the best timing response of the PMT. However, due to tube noise it is normally impossible to run the tubes at the maximum rated voltage, so one must also consider this factor in setting the gain of each PMT. The PMTs used on the neutron scintillator bars were 5 inch

RCA tubes model numbers 4522 and 8854. The optimal rise time and transit time are 2.9 ns and 66 ns respectively and are quoted at a high voltage (HV) of -3000 volts which is the maximum rated voltage for the PMTs. The tubes were therefore run as close to this limit as the tube noise permitted.

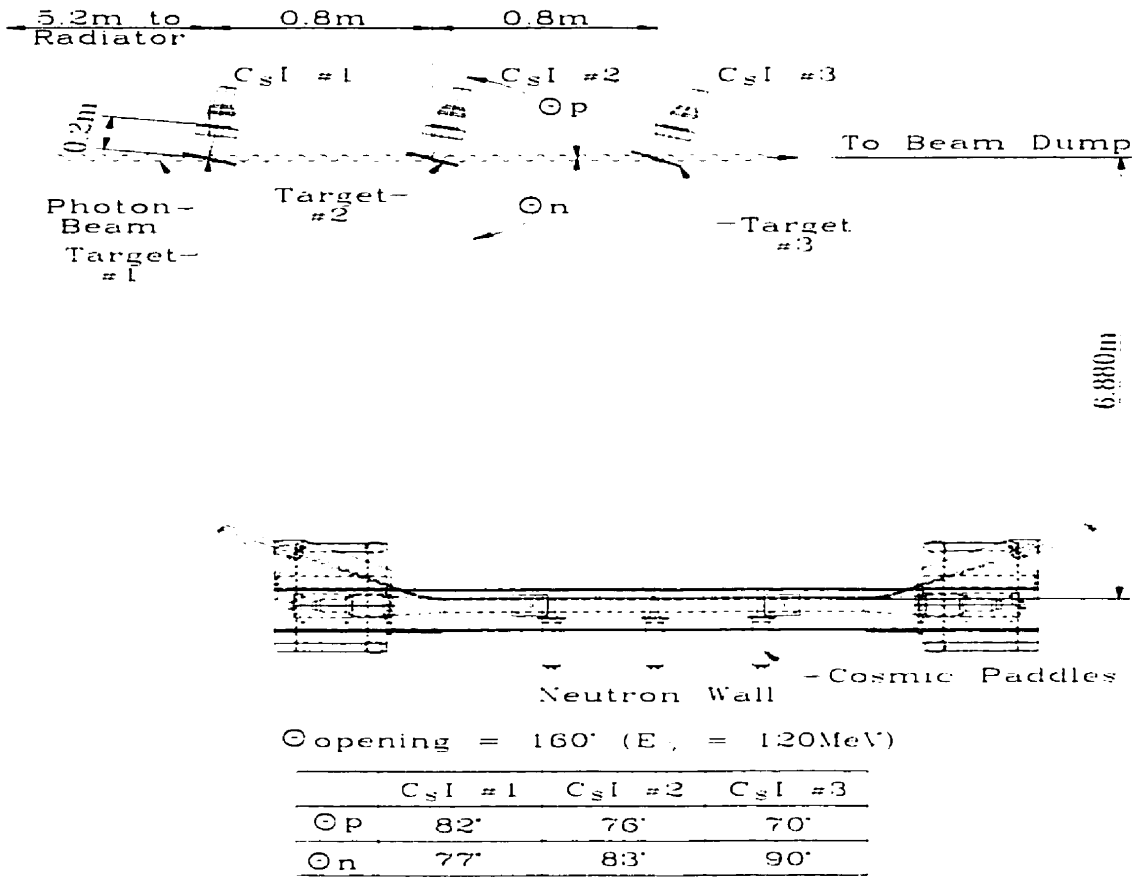

	CsI #1	CsI #2	CsI #3
⊙p	82°	76°	70°
⊙n	77°	83°	90°

Figure 3.5: General overview of experimental geometry (not to scale).

Figure 3.5 illustrates the experimental geometry for this measurement. The neutron detector was located at a distance of 6.852 m perpendicular to target number 3. The angles of the CsI detectors were chosen to meet the kinematical opening angle of $\theta_{opening} = 159.5°$, for the photodisintegration of deuterium for the photon energy of $E_\gamma = 120$ MeV. This was the center of the photon energy range selected for this

experiment.

Also shown in Figure 3.5 are the cosmic paddle detectors. These were simply scintillator detectors with a width much smaller than the expected position resolution obtained from the neutron bars. Three detectors were mounted on top of the neutron detector array while three were mounted directly beneath them. By taking coincidences between cosmic rays traversing the top and bottom paddles, the neutron detector could be calibrated in order to determine the position of impact for an incident charged particle along the length of the neutron bar. The cosmic events were also used to calibrate the energy deposition in the neutron detectors as described in the next chapter. The time resolution and therefore the position resolution could also be determined from such measurements. During the running of the experiment events triggered by cosmic rays were also recorded, so that the gain of the neutron detectors could be monitored. The gain of the detectors is important for determining the neutron detection efficiency.

3.4.1 Neutron array electronics

The electronics for the neutron detector are shown in Figure 3.6. The anode signals from the left and right PMTs were transported by 20 m RG58 cables to a passive 50 ohm splitter. This length of cable was chosen so that the delay of the signals would be closely matched to the time interval between the trigger signal and the time of arrival of the neutron detector signals at the ADCs and TDCs. One output of the 50 ohm splitter was connected to a charge integrating ADC while the other output was sent to a CFD which in turn was connected to a TDC. The signals connected to the ADC were first attenuated by typically a factor of 10 before arriving at the input. This attenuation was applied so that high energy protons from (γ, pp) events would fall in the dynamic range of the ADC. The output signal from the CFD provided

a stop for the TDC which in turn had been started by a signal from the proton arm Δ-E detector. The threshold of the CFD was set at the minimum level possible (10 mV) so that the effective hardware threshold would not cause a significant loss in the neutron detection efficiency. It was decided that the neutron detector threshold would be applied by a software cut after the level of low energy background events could be determined. The electronic circuit for the cosmic detectors mounted above and below the neutron array used to calibrate the neutron detector is not shown.

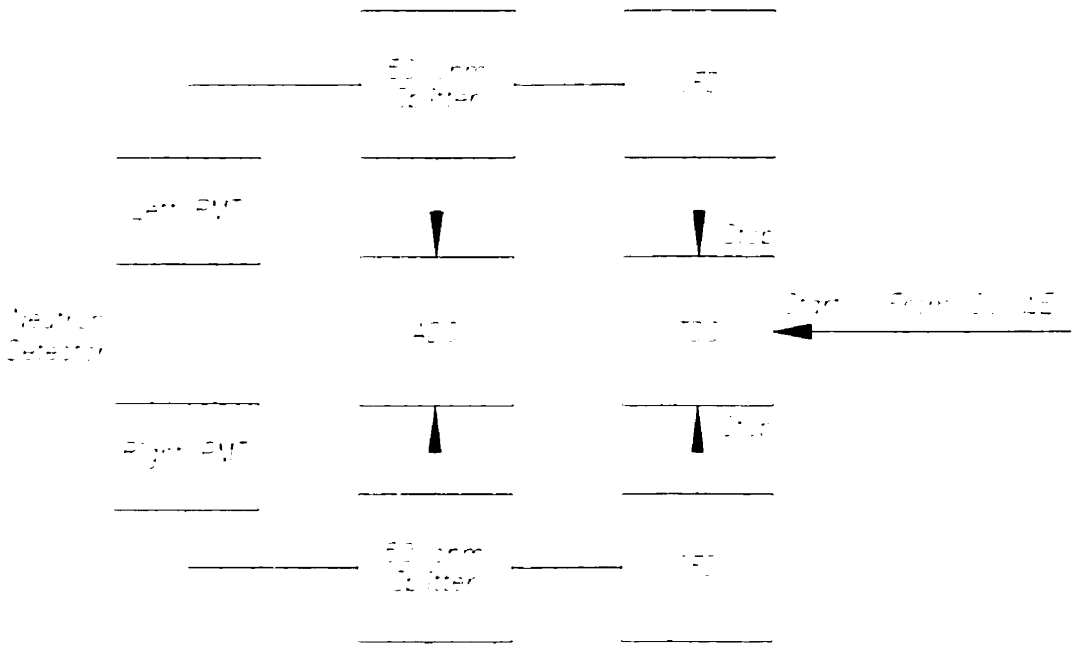

Figure 3.6: Neutron detector electronics.

3.4.2 Veto electronics

The electronics for the veto detectors are shown in Figure 3.7. The signals from the left and right PMT anodes were transported by 20 m RG58 cables and connected to the input of a CFD. The CFDs used also produced an analogue output pulse which was equal to that of the input analogue pulse with approximately a ± 10% resolution. This analogue output pulse was connected to a charge integrating ADC. An event in either the TDC left signal or TDC right signal was used to identify charge particles. It was thought that a Δ-E E scatter plot of the veto detector and the neutron bars would produce charged particle bands so that proton events could be identified. Unfortunately, the poor resolution of the ADC signals in conjunction with the large energy loss of protons on the way to the neutron array made this method of particle identification impossible. However, an alternate method using the energy deposited in the neutron scintillators and the TOF of the particle can be used to identify the species of charged particle.

3.5 Targets

The target materials used to make the ^{16}O measurement were distilled water and heavy water (D_2O). The heavy water targets allowed the simultaneous measurement of the $^{2}H(\gamma, pn)$ and $^{16}O(\gamma, pn)^{14}N_{0,1,2,..}$ reactions. The water targets were mostly used for background subtraction of the oxygen in the heavy water so that absolute yields of proton and coincident proton-neutron events from the deuterium present could be extracted. That is, protons and neutrons resulting from the oxygen in the heavy water could be removed by a measurement of the proton and neutron yields from the water target measurement. Subtracting the water background determined the proton and neutron yields from the deuterium present in the heavy water. The

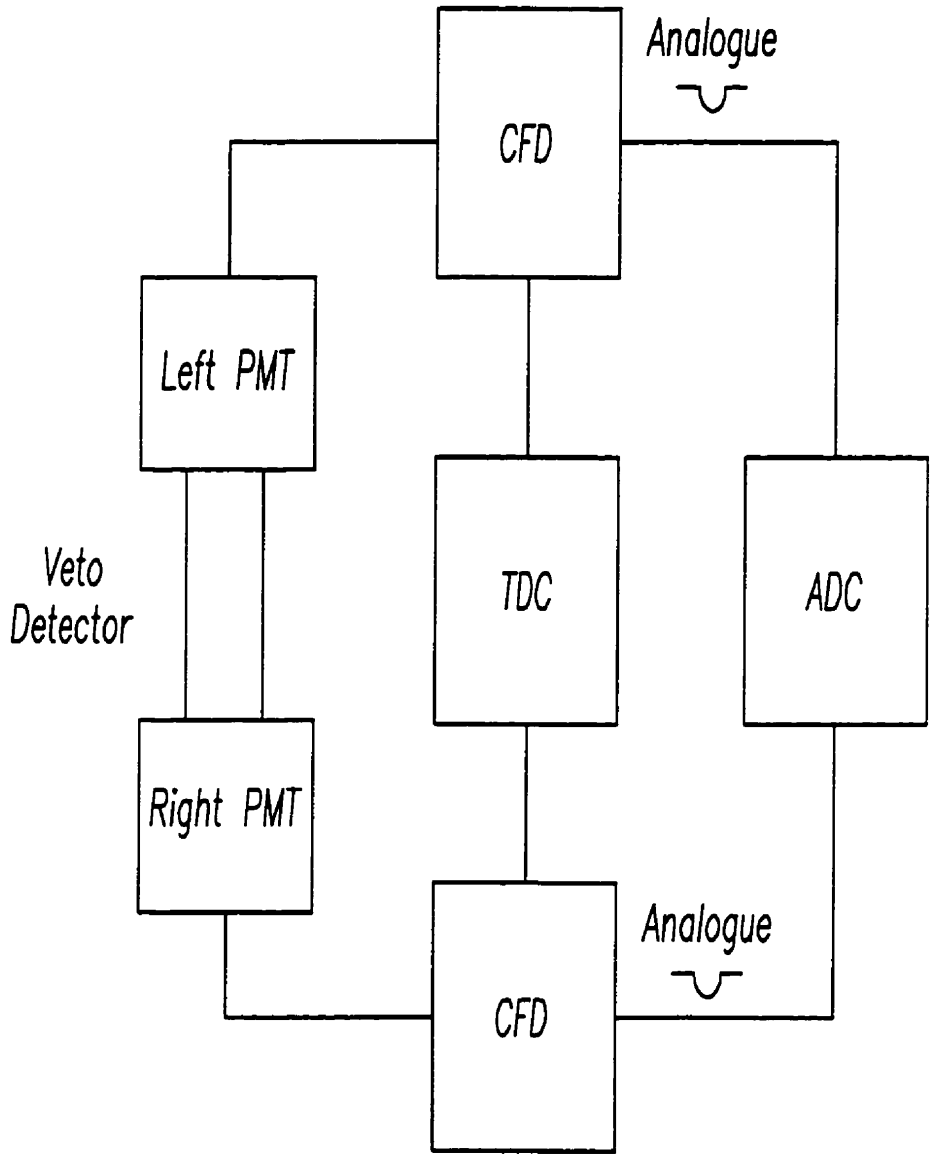

Figure 3.7: Veto detector electronics.

heavy water targets were used primarily for this measurement so that the gains of the CsI detectors could be monitored on a run-to-run basis. It was observed that the gain of the detectors did not fluctuate significantly during the course of the experiment. Another reason for running primarily with D_2O was so that the detection efficiency of the neutron array on a run-to-run basis could be determined. The composition of the heavy water is given in Table 3.1.

Table 3.1: Heavy water composition.

D_2O (%)	DHO (%)	H_2O (%)
92.30	6.75	0.90

The target materials were contained in thin oval frames machined from aluminum metal. Simulations resulted in the choice of 1 mm thick targets. This was a compromise between count rate and tolerable energy losses of the protons in the target which in turn influences the energy resolution of the detected protons. Figure 3.8 shows the dimensions of the target frames. The inner oval represents the target volume which would be filled with the liquid target material. Thin target windows (7.6 micron) made of kapton were glued to the target frames to provide a water-tight seal. The windows were made as thin as possible to minimize the energy loss of the ejected protons. The actual dimensions of the targets were dictated by the size of the beam spot produced on each target as determined by the defining collimator and the distance to each target. Furthermore, it was desirable to rotate the targets with respect to the incident photon beam. The rotation angles were chosen so that the protons exiting the targets would traverse as little target material as possible. The rotation also increased the effective target thickness with respect to the photon beam, thereby increasing the number of possible scattering centers. A final consideration was that the target rotations caused the circular beam spot to be transformed into an elliptical

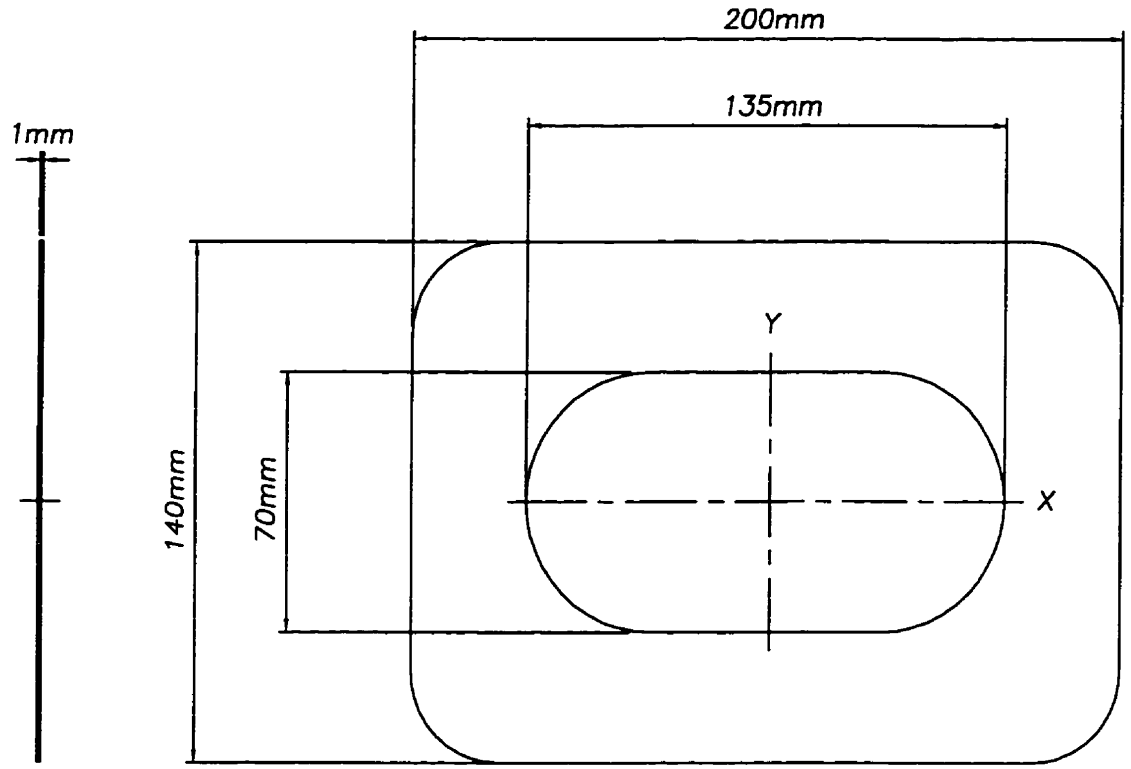

NOTE: 0.3 mil (7.6 MICRON) KAPTON (200 ANGSTROMGOLD ONE SIDE ONLY) KAPTON GLUED TO BOTH SIDES OF THE ALUMINUM TARGET FRAME.

Figure 3.8: Figure depicting the target design.

beam spot with the major axis along the x-axis and the minor axis along the y-axis (see Figure 3.8). The rotation angles were also chosen so that the targets could be kept to a reasonable size due to some technical problems with the targets as discussed below. Table 3.2 gives the dimensions of the beam spots for each of the three target positions.

Some problems were encountered with the targets. When the targets were filled with water a bulge occurred in the windows due to the pressure exerted on them by the liquid target material. A typical profile of the change from the desired 1.0 mm target thickness is shown in Figure 3.9. Also due to the thin target windows some loss

Table 3.2: Beam spot parameters for each target position.

Target Number	Distance to Collimator (m)	Beam Spot Size (cm)	Rotation Angle (°)	Major or X-axis (cm)	Minor or Y-axis (cm)
1	5.20	2.05	-24.0	5.04	2.05
2	6.00	2.37	-28.0	5.05	2.37
3	6.80	2.68	-32.0	5.05	2.68

of target material occurred, so that the targets had to be topped up daily via a syringe needle fastened to the top of the target. The rate of loss of target material remained constant throughout the experiment. Profiles of a full and a typically depleted target (usually after a 24 hour period) were made so that the target thickness as a function of time could be determined. However, after extraction of the deuterium cross sections from the experimental data taken, it was observed that the determined cross sections did not agree with previous measurements. This was taken as evidence that the target thickness was not known to the expected accuracy of the profile measurements. It was therefore necessary to normalize the target thickness by a comparison of the measured deuterium yields and the accepted values of the deuterium cross section.

Three empty targets were also constructed so that empty target runs could be performed for background subtraction of protons produced in the target windows. Figure 3.10 shows the movable target ladder.

3.6 The photon tagging technique

The method of producing monochromatic photons was first suggested independently by Camac [47] at Cornell and Koch [47] at Illinois. The possibility of determining the photon energy enables one to perform kinematically complete experiments where one of the outgoing reaction products (in a 2 or 3 body final state) is undetected. In the present experiment this corresponds to the undetected recoil nucleus.

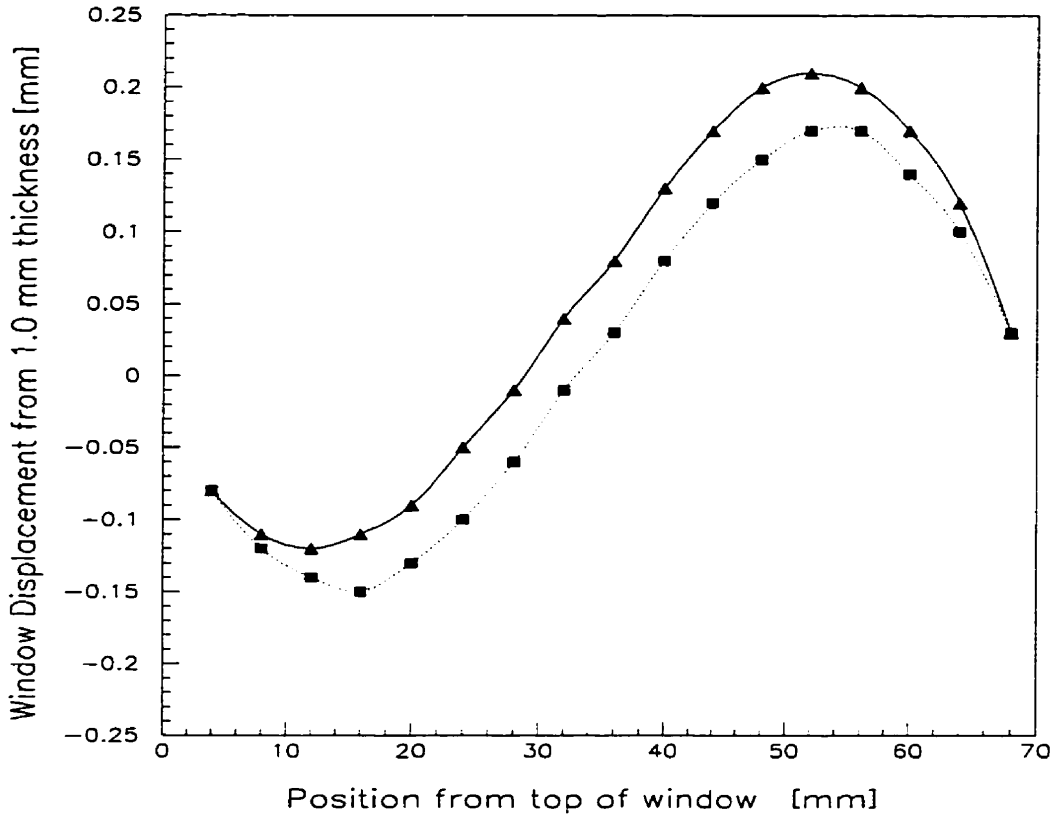

Figure 3.9: Typical heavy water target window profile measured relative to the 1.0 mm design thickness. The triangles represent the measured target profile when the target weighed 60.40 g. The squares represent the measured target profile when the target weighed 60.00 g. The latter value was typical of the loss of heavy water after a 24 hour period.

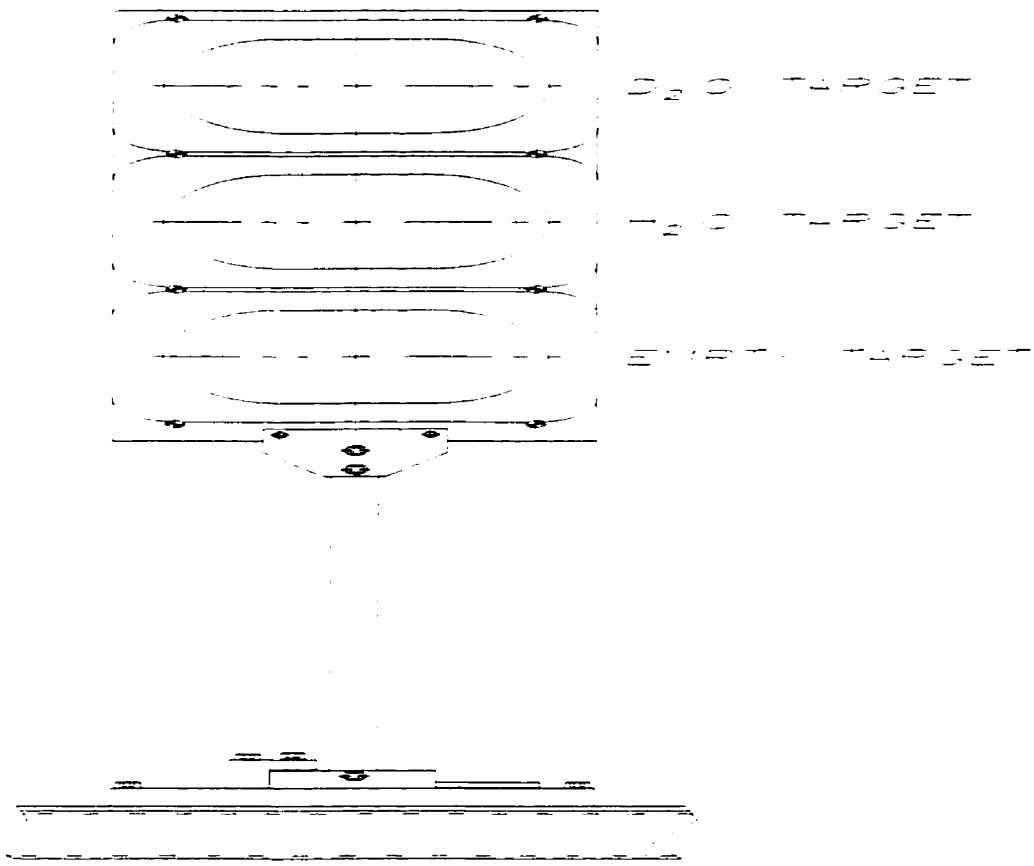

Figure 3.10: The movable target ladder.

Early photon tagging experiments were limited to a flux of $\sim 10^5$ photons/s due to the intrinsically slow electronics available at the time. The SAL photon tagging system is able to produce a flux of $> 10^8$ tagged photons/s by employing state of the art electronics.

A simplified drawing of the SAL photon tagging system is depicted in Figure 3.11. At a distance of 5.2 m from the first target ladder, electrons pass through a 115 μm aluminum radiator. At the bremsstrahlung radiator, photons are produced with a

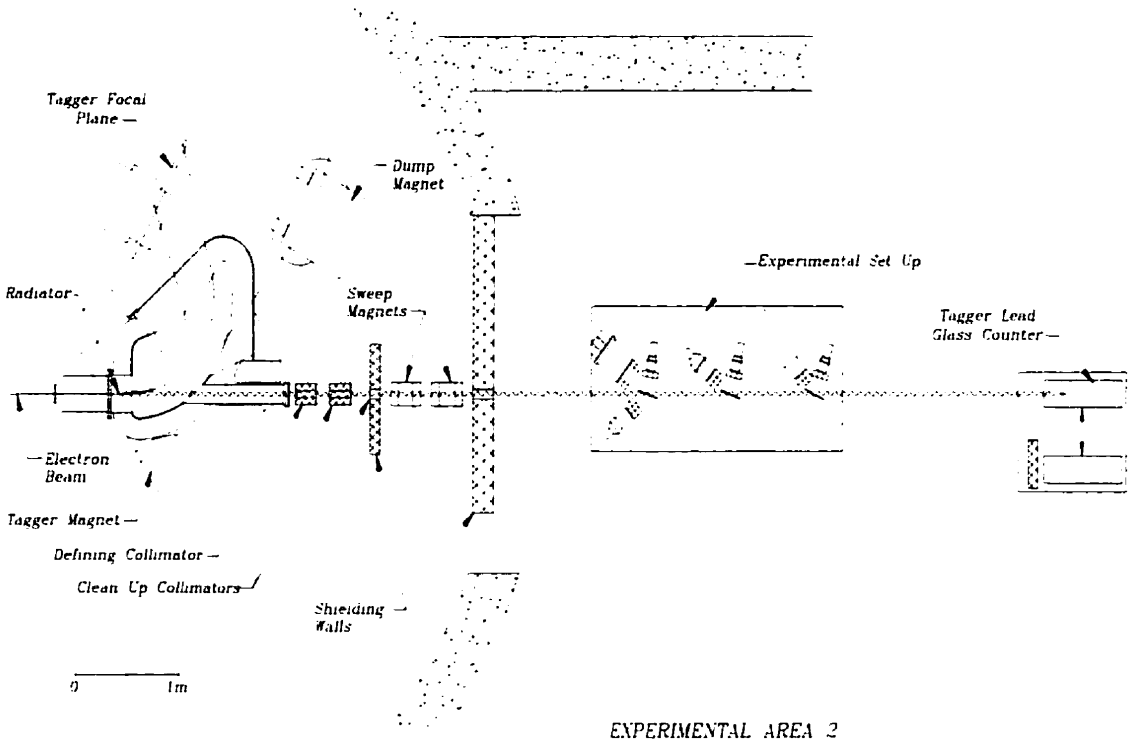

Figure 3.11: SAL Photon Tagging System

characteristic opening angle given in the relativistic limit by

$$\begin{aligned} \theta_{opening} &= \frac{1}{\gamma} \\ &= \frac{m_e}{E_e} \end{aligned}$$

where m_e is the electron mass and E_e is the electron energy. The defining collimator labeled in Figure 3.11 was chosen to be 15.0 mm in diameter. The size of the collimator defines the size of the beam spot on the targets located further down stream. This size for the defining collimator was chosen to maximize the tagging efficiency (defined

later in this section) and at the same time to produce reasonably sized beam spots on the targets. The photons able to pass through this collimator travel a further 3.3 m to the first target ladder. The recoil electrons from the bremsstrahlung process are then momentum analyzed via the photon tagging magnet and electron focal plane detectors. Electrons which do not produce bremsstrahlung photons are directed by a dump magnet to a shielded beam dump well removed from EA2.

The method of producing monochromatic photons from a bremsstrahlung source is in theory quite straightforward. If a beam of electrons is incident upon a thin radiator, some of the electrons will undergo the bremsstrahlung process and will be degraded in energy. Electrons which have been degraded in energy so as to be within the momentum acceptance of the tagging spectrometer are detected in the focal plane detectors. Since the initial electron energy (E_i) and the residual electron energy (E_f) are known, one simply has a photon produced with an energy (K) given by

$$K = E_i - E_f. \tag{3.5}$$

If a coincidence is required between the reaction product (X-arm), initiated by a photon whose residual electron was detected in the tagger focal plane, then the energy of the photon is uniquely determined.

The energy resolution of the tagged photon is determined by the physical size of the electron focal plane detectors. The tagging focal plane consists of 63 identical scintillator detectors which, due to the overlap design, results in 62 tagged photon energy bins. The tagged energy range selected for most runs was from E_γ = 98-142 MeV. However, some time was spent at the lower photon energy range from $E_\gamma = 61 - 117$ MeV. This increased the energy range of the neutrons from the two-

body $^2H(\gamma, pn)$ reaction which allowed for the determination of the neutron detection efficiency over a correspondingly larger range of neutron kinetic energies.

The photon flux had to be corrected for the tagging efficiency. The tagging efficiency for each channel of the spectrometer (defined as the ratio of the number of photons incident on the target to the number of electrons detected in the tagging focal plane detectors) was measured periodically during the course of the experiment. This measurement was made by reducing the photon flux by approximately 3 orders of magnitude, placing a lead glass detector (see Figure 3.11) directly in the photon beam and counting the photons incident on this detector. The assumptions made here are that the lead glass is 100% efficient for detecting the incident photons and that the tagging efficiency is independent of the rate of produced photons. The tagging efficiency is determined by

$$\epsilon_{TAG} = \frac{A - B}{C - D} \tag{3.6}$$

where

A = the total number of X-interrupts with the radiator-in,

B = the total number of X-interrupts with the radiator-out (normalized to the same live time as A),

C = the total number of electron counts for each tagger focal plane scaler with the radiator-in , and

D = the total number of electron counts for each tagger focal plane scaler with the radiator-out (normalized to the same live time as C).

Therefore, by multiplying the number of counts in the tagger focal plane scaler under consideration by the tagging efficiency, the photon flux incident on the target was

determined. For the electron beam energy of 206.7 MeV and a defining collimator of 15.0 mm, an average tagging efficiency of typically 53% was obtained for the photon energy range $E_\gamma = 98 - 142$ MeV.

Chapter 4

Data Analysis

4.1 Introduction

In this chapter a detailed description of the photon tagger, proton telescopes and neutron detector calibrations is presented. Due to the poor resolution of CsI detector number three, the data obtained from this telescope will be excluded. A description of the more important points of the data reduction is presented, with special emphasis on the novel method devised for the subtraction of the tagger random background. Finally, the formulae used to evaluate the single and double arm cross sections are stated, followed by a list of the systematic errors inherent to the measurement reported in this thesis.

4.2 Neutron Detector

The neutron detector is required to determine the polar angle θ_n, azimuthal angle ϕ_n and the kinetic energy T_n. Both T_n and θ_n require the timing information recorded from each end of the neutron detector while ϕ_n was determined by which detector in the array detected a neutron. The flight path of the neutron can be determined from physical measurements of the experimental geometry and by the measured angles θ_n and ϕ_n. If the time the neutron left the target is known, this information can be used with the flight path distance to determine the velocity of the neutron v_n. The kinetic

energy of the neutron is then given relativistically by the equation

$$T_n = m_n c^2 \left(\frac{1}{\sqrt{1 - v^2/c^2}} - 1\right). \tag{4.1}$$

4.2.1 Position Calibration

The neutron scintillator bars had a photomultiplier tube (PMT) coupled at each end and measured the TOF by the so-called mean timing method. The particle TOF is then given by

$$T_{net} = 1/2(k_L TDC_L + k_R TDC_R) + f_p + constant \tag{4.2}$$

where TDC_L, TDC_R are the TDC values (with respect to the proton Δ-E trigger signal) obtained from the left and right PMT readings, f_p is the proton time-of-flight from the target to the proton Δ-E detector and k_L and k_R are the TDC conversion coefficients converting the TDC channel number to time. By employing the mean timing method one obtains a better time resolution for $\sigma_{net}(TOF)$ by a factor $1/\sqrt{2}$ for a hit at the center of the scintillator than for the read-out of the scintillator at only one end.

This method also enables the determination of the incident particle's point of interaction along the length of the scintillator. Since the neutron detector timing information is required in order to determine the hit position of a particle along the length of the scintillator bar, the neutron detector TDCs were first calibrated using a cable of precisely known signal transit time. Then the difference in the TDC peaks with the cable inserted and removed provided the conversion gain between a

TDC channel and the relative time elapsed in nanoseconds. The conversion gains, k, typically ranged from 0.9 to 1.1 ns/channel.

With the TDCs calibrated, the neutron detectors could be calibrated for the position of interaction of a particle along the length of the scintillator bar by using the difference in the left and right timings of the neutron bar photomultiplier signals. These in turn triggered their respective neutron detector TDCs.

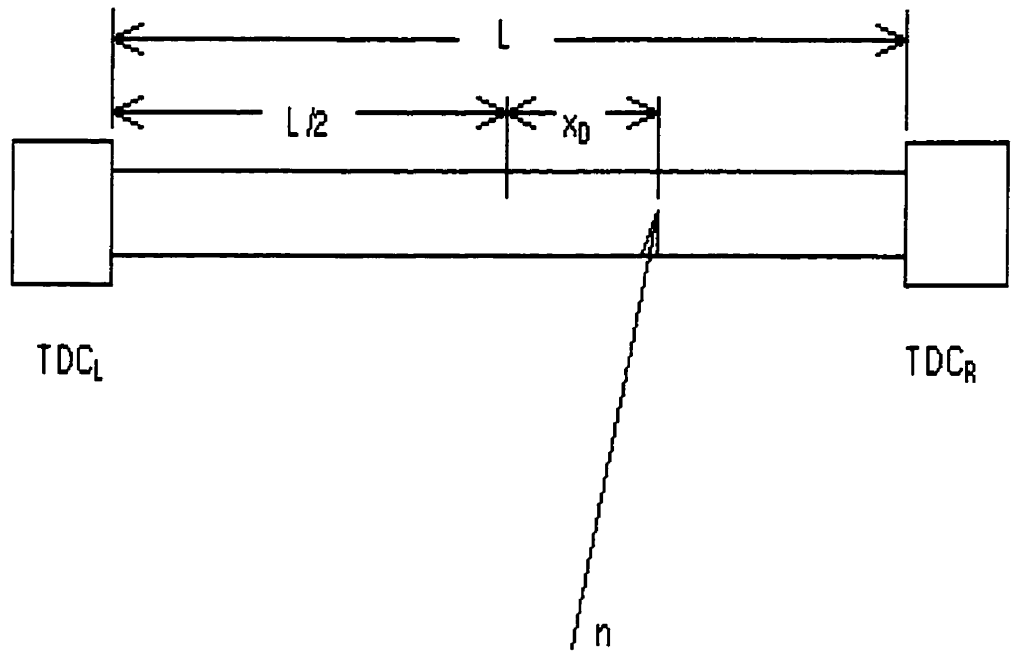

Figure 4.1: Schematic figure of the relation between the left and right TDC times and the position of the detected particle.

Figure 4.1 illustrates the relation between the left and right TDC times and the

position of the detected particle. One obtains

$$\begin{aligned}(k_L TDC_L - k_R TDC_R) &= (\frac{L}{2} + x_D)\frac{1}{v_{eff}} - (\frac{L}{2} - x_D)\frac{1}{v_{eff}} \\ &= \frac{2x_D}{v_{eff}} \end{aligned} \tag{4.3}$$

where x_D is the position of the incident particle, L is the length of the scintillator , k_i are the TDC conversion coefficients, TDC_i are the TDC channel readings of each side of the detector and v_{eff} is the effective signal velocity of the scintillation light along the length of the scintillator. The effective signal velocity, v_{eff}, is different from the speed of light in the scintillator (given by the index of refraction n = 1.58 for BC400) due to the fact that the light does not travel directly to the PMT but is actually reflected by the boundaries many times before reaching the PMT.

Inverting the above equation, the position of the particle hit along the length of the scintillator is given by

$$x_D = (k_L TDC_L - k_R TDC_R)v_{eff}/2 + C. \tag{4.4}$$

The constant C accounts for the different delays of the left and right PMT signals reaching their respective TDCs. A plot of the neutron detector TDC left minus right values as a function of the known detector positions yielded a straight line with the reciprocal of the slope equal to $\frac{1}{2}v_{eff}$. The effective signal velocity for the neutron detectors used was typically 15.0 cm/ns. With the above definition for x_D, the error determination in the hit position, σ_{x_D}, is given by

$$\begin{aligned}\sigma_{x_D} = \delta(x_D) &= \delta((k_L TDC_L - k_R TDC_R)v_{eff}/2 + C) \\ &= ((\delta k_L TDC_L + \delta k_R TDC_R)v_{eff}/2) \\ &= \sigma_{TOF} v_{eff}/2 \end{aligned} \tag{4.5}$$

where $\sigma_{TOF} = \delta(k_L TDC_L - k_R TDC_R)$ if the start time is ignored.

The neutron detector position calibration was obtained using the known position of the cosmic paddles located above and below the neutron detector as depicted in Figure 3.5. The difference in the known positions along the neutron detector and the calculated neutron position for one of the neutron detectors is given in Figure 4.2 below. The mean of -0.70 mm indicates that the position determination has been calibrated to within this accuracy and the full width half maximum (FWHM) of the position resolution of 6.3 cm is in good agreement with the typical time resolution of 0.9 ns FWHM multiplied by one half the signal velocity of 15.0 cm/ns as expected.

4.2.2 Energy Calibration

In order to calculate the kinetic energy of the neutron, via the time-of-flight method, it is necessary to know the precise time the neutron left the target. This is known as time-zero and is the reference time relative to which all neutron flight times are measured. Two independent methods were performed in order to determine time-zero.

The first, referred to as the source method, was performed at the beginning and end of the experimental run. This enabled neutron energies to be measured from the very beginning of the experiment and verified that the electronics were performing

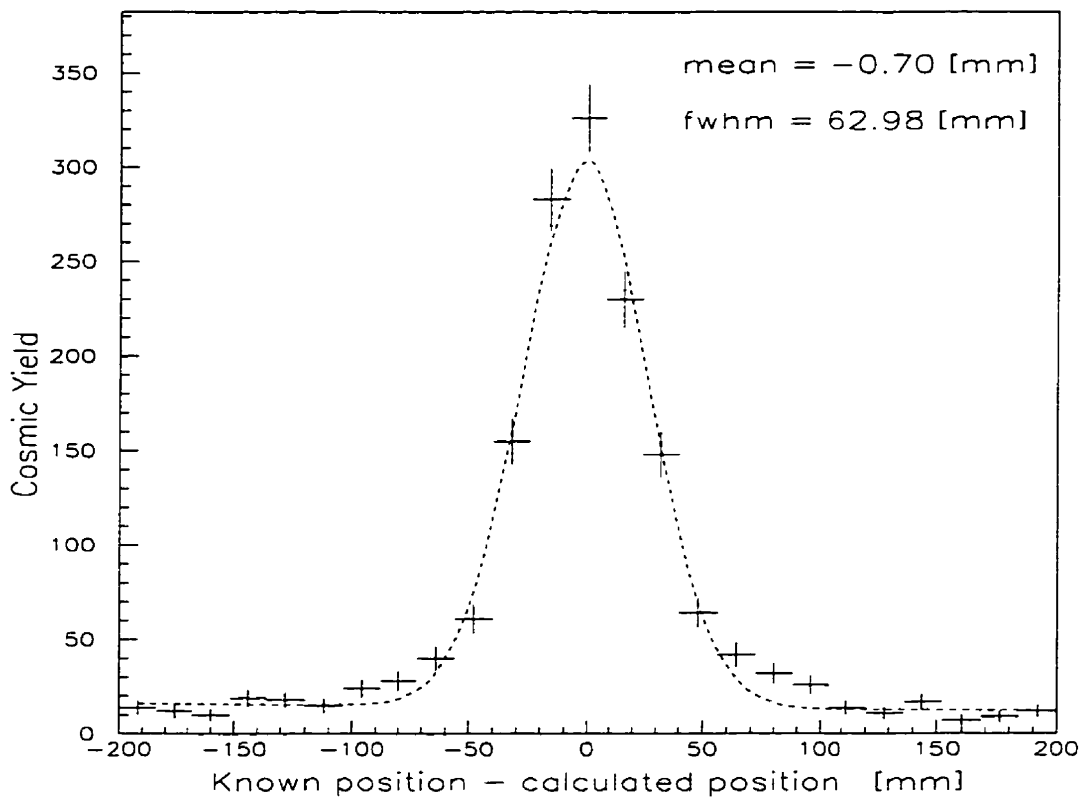

Figure 4.2: The difference in the known hit position of cosmics traversing perpendicularly through a scintillator bar and the experimentally determined hit position for three equally spaced locations along the length of the detector. Given also are the centroid and the FWHM values of a fit using a Gaussian with a quadratic background.

as expected. The source method will only be discussed briefly, as the second method was found to be able to locate time-zero more accurately. The first method simply used a ^{106}Ru source and a common timing paddle. The TDC information consisted of a coincidence between the timing paddle and proton Δ-E detectors, where each detector in turn was used to start the TDCs while the other detector was used as a stop. In conjunction with the above results, the timing paddle was used as a start of the neutron TDCs where the stop was provided by each of the neutron detectors. This information was sufficient to determine time-zero for each CsI Δ-E and neutron

bar combination. Although the source method of calibration was consistent with the second method discussed below, it was not as accurate. This was due to problems related to the relatively low-energy electrons emitted from the source, as well as to the fact that the position of the source on the Δ-E detector may not be the same as that of the particles which were incident on this detector during the data taking. This was because the Δ-E detector had a PMT coupled to only one side of the scintillator making the timing derived from this detector position dependent. Since the Δ-E detector had to be removed fron the lead collimator for calibration purposes, the positioning of the source for calibration purposes could not be ensured to be the same as the area of acceptance of the detector during the course of the experiment. This uncertainty of positioning the source for calibration purposes could cause a shift in time-zero of as much as 10 channels. This shift in turn would cause an uncertainty in the neutron energy determination of about 1 MeV for neutrons emanating from the $^2H(\gamma, pn)$ reaction for the photon energies used.

Figure 4.3 depicts the relevant time intervals necessary to determine the neutron time-of-flight via the mean timing method. These intervals are defined as follows:

f_n Time-of-flight of the neutron from the time the neutron left the target until the interaction of the neutron in the scintillator.

f_p Time-of-flight of the proton defined as the time from when the proton left the target until it was detected in the proton Δ-E detector which in turn started the neutron arm TDCs. This required that the energy of the proton be determined. For the distances involved and the typical proton energies encountered, the flight times ranged from 1.7 to 2.3 ns.

t_p The time necessary for ionization light produced to travel from the point of interaction to the proton Δ-E photomultiplier tube. Since the proton Δ-E detector was read out on only one side of the scintillator, the value t_p will not be a constant.

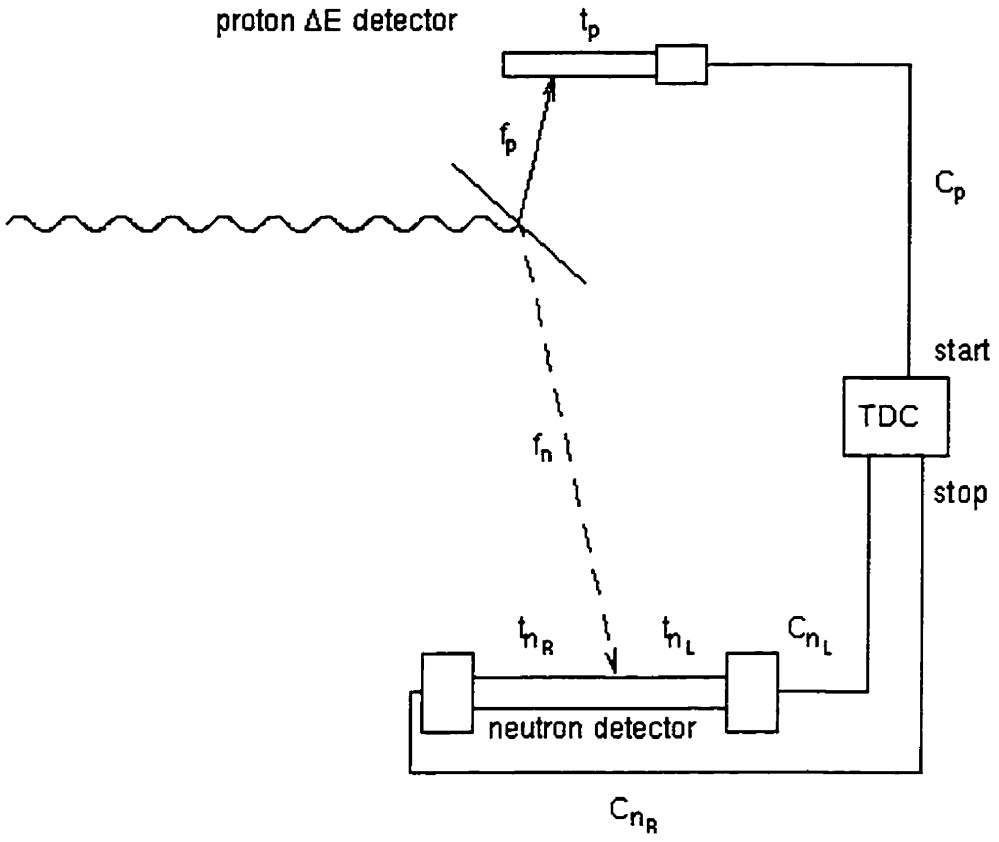

Figure 4.3: Diagram of the time intervals relevant to determine the neutron time-of-flight.

Due to the collimation of the proton telescope, the variation in time should be about 0.4 ns.

t_{n_L}, t_{n_R} The propagation time of the scintillation light to travel from the point of interaction to the left and right photomultiper tubes respectively. Note that the sum $t_{n_L} + t_{n_R}$ is a constant as a result of the mean timing methoded employed.

C_p Represents the constant delay times of the proton signal used to start the neutron TDCs. These include the light propagation in the light guide, the electron transit time in the photomultiplier tube, and the time for the signal to travel through the electronics and connecting cables.

C_{n_R}, C_{n_L} Represent the constant delay times of the neutron right, left signals used to stop the neutron TDCs. These include the light propagation in the light guide,

the electron transit time in the photomultiplier tube and the time for the signal to travel through the electronics and connecting cables.

The second method makes use of determining experimentally the measured time-zero of the reaction and is defined as follows. Time-zero is defined as the precise time the neutron left the target and is related to the constant time intervals given above as follows. The elapsed time between the start and stop of the neutron TDC is

$$t_{stop} - t_{start} = kTDC, \tag{4.6}$$

where k is the TDC conversion coefficient discussed in the preceding section and TDC is the neutron detector TDC channel. In terms of the time intervals given in Figure 4.3 we also have the relation for the left hand side of the neutron detector

$$t_{stop_L} = f_n + t_{n_L} + C_{n_L}, \tag{4.7}$$

with a similar expression for the right hand side of the neutron detector. The time intervals associated with the start signal are

$$t_{start} = f_p + t_p + C_p. \tag{4.8}$$

Combining the above equations we obtain the relation

$$t_{stop_L} + t_{stop_R} - 2t_{start} = f_n + t_{n_L} + C_{n_L} + f_n + t_{n_R} + C_{n_R} - 2(f_p + t_p + C_p)$$

$$= k_L TDC_L + k_R TDC_R. \quad (4.9)$$

Solving the above equation for the neutron time-of-flight yields

$$f_n = \frac{1}{2}(k_L TDC_L + k_R TDC_R) + f_p + \frac{1}{2}(2t_p + 2C_p - t_{n_L} - t_{n_R} - C_{n_L} - C_{n_R}). \quad (4.10)$$

Noting that $t_{n_L} + t_{n_R}$ is a constant since the propagation time in the scintillator is constant and assuming that t_p is a constant (see above definition) then the last term in parentheses in Equation 4.10 is a constant. This term corresponds to the offset relating the neutron TDCs to the flight time of the neutron f_n when account is also taken of the proton TOF, f_p. This is commonly called time-zero, t_0 and is arbitrarily chosen to be when the interaction occurs in the target. The neutron TOF is then given by

$$f_n = \frac{1}{2}(k_L TDC_L + k_R TDC_R) + f_p - t_0, \quad (4.11)$$

where time-zero is equal to

$$t_0 = \frac{1}{2}(t_{n_L} + t_{n_R} + C_{n_L} + C_{n_R} - 2t_p - 2C_p). \quad (4.12)$$

Time-zero, defined above, for the second method for calibrating the neutron detectors is realized experimentally by locating the gamma flash in the neutron TDC spectra. The gamma flash is indicated on Figure 4.4 which is a plot of the mean time-of-flight of the neutron or photon for one of the neutron detectors. Simply by

measuring the distance from the target to the detector and knowing the speed of light one can then fix time-zero or the exact time the photon left the target. For determining time-zero all particles were considered photons so that the geometrical jitter due to the different flight paths of the photons could be removed. The mean time-of-flight, in this instance for the photon, is given by $f_n = \frac{1}{2}(k_L TDC_L + k_R TDC_R) + f_p - d/c$ where d/c is the distance to the neutron detector divided by the speed of light. The difference in the position of the gamma flash derived from f_n with and without the subtraction of the term d/c then gives time-zero. The insert is a close-up of the gamma flash and it can be seen that the FWHM time resolution is about 9 channels or 0.9 ns. The structure to the right of the gamma flash corresponds to real neutron events. To the left of the gamma flash the events are purely random, as for such TOFs to exist would require that the particle have a velocity greater than the speed of light. Between the gamma flash and the onset of the real neutron events is also a region of purely random events. These values for the TOF would require neutron energies greater than those expected in the current measurement. A software threshold of the deposited energy (in units of electron-equivalent energy, MeV_{ee}) in the neutron detector of 2 MeV_{ee} (or a proton energy of about 5 MeV for BC400 plastic scintillator) was applied. This then allowed true neutron TOFs to extend up to channel 4000.

The neutron TDC start was triggered by a charged particle in the proton arm CsI Δ-E detector. The distance from the target (assumed to be a point target) to the Δ-E detector was 18.0 cm, so once the proton kinetic energy was determined, the neutron TOF was corrected for the proton target detector TOF. Knowing the distance from the target to the center of the neutron detector (the flight path increased only by about 2% to 3% for a particle hit at the corner of the neutron detector) and the speed of light enables the time of the gamma flash to be determined. So the time-of-flight

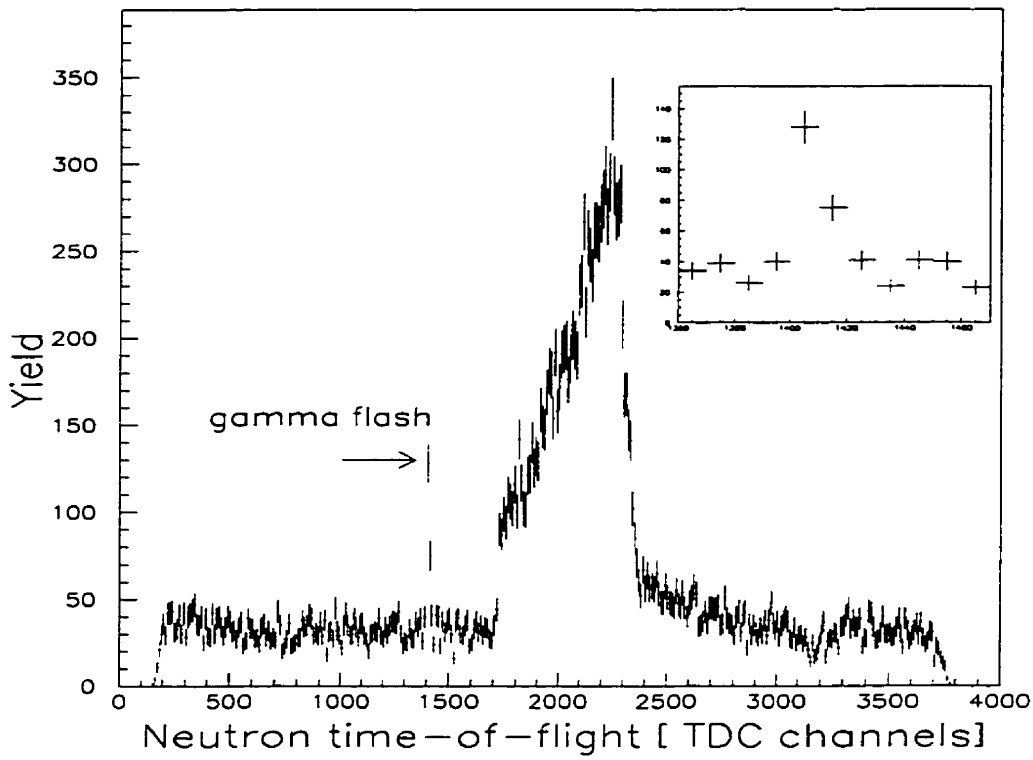

Figure 4.4: A typical neutron TDC spectrum for one of the 10 neutron detectors. The gamma flash is indicated on the figure and the insert shows an enlarged view of this peak. The FWHM of this peak is 0.9 ns.

for the neutron is given by

$$TOF_n = TOF_p + (TDC_n - TDC_{flash})/10 + T_{flash} \tag{4.13}$$

where TOF_p is the time for the proton with energy T_p to travel the 18.0 cm from the target to the Δ-E detector, TDC_n is the average TDC channel corresponding to the mean time-of-flight of the neutron, TDC_{flash} is the TDC channel location of the gamma flash (the factor of 10 converts this difference to ns) and T_{flash} is the time for the photon to travel the known distance between the target and neutron detector.

For instance, the gamma flash for CsI-1 occurred at T_{flash} =23.6 $\pm$ 0.1 ns.

4.2.3 Calibration of deposited energy

In order to obtain the deposited energy in the neutron detectors, the ADC information read out from each end is utilized. The ADC was of the charge integrating type where the digitized output was proportional to the integral of the pulse at the ADC input. Upon corrections for light attenuation, the ADC value is proportional to the light produced in the scintillator, which in turn is related to the deposited energy and therefore to the kinetic energy of the particle, if the species of particle undergoing the ionization is known.

The ADC value obtained for a single photomultiplier depends both on the deposited energy and, due to light attenuation effects within the scintillation material itself, on the point of interaction. The light attenuation is commonly approximated by an exponential decrease. The amount of light then transmitted to the right hand end of the neutron detector and charge integrated by the ADC can be written as

$$ADC_R = A_R e^{-\mu d} L \tag{4.14}$$

where μ is the light attenuation coefficient of that particular material, A_R is the conversion factor between the amount of light at the right hand edge and the ADC channel, L is the amount of scintillation light produced, and d is the distance from the point of interaction to the end of the scintillator. The conversion factor A_R is related to the gain of the photomultipler, the light collection efficiency of the optical couplings of the scintillator and the PMT, the conversion coefficient of the ADC itself, and the attenuation of the signal in the cables and attenuators. Similarly, the ADC

value measured at the left hand side of the scintillator of total length l is

$$ADC_L = A_L e^{-\mu(l-d)} L. \tag{4.15}$$

However, in order to make the ADC information independent of the point of interaction in the scintillator, the geometrical mean of the two ADCs is constructed as follows:

$$ADC_{mean} \equiv \sqrt{ADC_R \cdot ADC_L} = \sqrt{A_R A_L} e^{-\mu l/2} L. \tag{4.16}$$

The above equation shows that the ADC_{mean} is proportional to the quantity of produced scintillation light which in turn is proportional to the deposited energy.

The detectors were calibrated using the ADC information also recorded during the neutron detector position calibration (see Section 4.2.1). Given that the energy deposition for minimum ionizing cosmic ray muons is 1.955"MeV_{ee}/cm^2, the density of the plastic scintillators was 1.032 g/cm^3 and that the distance traversed by the muons was 15.0 cm, the effective gain for all detectors could be calibrated using the fact that the quantity of scintillation light produced is equal to

$$L = \frac{ADC_{mean}}{k} = 30.263 MeV_{ee} \tag{4.17}$$

where k is a constant for each detector constructed ADC_{mean} ($k = \sqrt{A_R A_L} e^{-\mu l/2}$) assuming that the high voltage applied to each photomultiplier tube base remained constant. The constant k is the gain of the PMT and relates the light output or ADC value to an energy in electron-equivalent energy (MeV_{ee}). The value then actually measured by the mean of the left and right ADCs can be used to calculate the gain

so that

$$k = \frac{ADC_{mean}}{30.263 MeV_{ee}} \tag{4.18}$$

can be determined for each neutron detector.

4.2.4 Neutron detector bias

It is common practice to calculate the deposited energy in units of electron-equivalent energy (expressed as MeV_{ee}). This is due to the fact that for minimum ionizing particles the amount of light produced is linear as a function of the particle's kinetic energy. The detection of a neutron can result, for example, by the neutron elastic scattering from a hydrogen nucleus in the scintillator, quasielastic scattering from the carbon present in the scintillator, or a capture reaction on the free proton (only resulting in a 2.225 MeV photon) and capture on the carbon nuclei as well. For elastic scattering, the scattered proton's energy can range from zero to the full incident energy of the neutron. This fact, in combination with knowing the incident neutron's energy (via TOF), would enable one to determine the neutron ADC_{mean} gains as described in the previous section. The scintillation light output for protons is not a linear function of the deposited energy. However, the energy deposited by the proton can be made linear if it is converted to electron-equivalent-energy. This can be accomplished by the use of the formula [48]

$$E_{ee} = 0.95T_p - 8.0(1 - exp(-.10T_p^{0.90})) \tag{4.19}$$

where T_p is the proton kinetic energy, and E_{ee} is the deposited energy in MeV_{ee}. The above relation is for the NE102 plastic scintillator which has very similar properties to the Bicron 408 plastic used. Since no light output data are available for Bicron 408, the characteristic light output is assumed to be the same as NE102. The gains found

using the deuterium reaction method were in agreement with the cosmic method discussed in the previous section, and served as a check of the neutron detector calibrations. The neutron detection efficiency is sensitive to the threshold applied to the neutron ADCs. Equally important in choosing the neutron detector biasing is the rejection of background neutrons which are predominantly low in energy.

Figure 4.5 depicts the correlation between the energy deposited in the neutron detector and the neutron time-of-flight. The kinematically allowed values for TOF appear as a characteristic triangular shape in the plot of the TOF versus the deposited energy. At low deposited energies, less than 2 MeV_{ee}, there is a large contribution of random neutron TOF values. This is evident since this ridge of TOF values extends well beyond the allowed values depicted by the characteristic triangular shape in the graph. The neutron bias threshold was chosen to be 2 MeV_{ee} in order to greatly reduce the number of random neutrons.

4.3 The photon beam

4.3.1 Prompt peak

It is common to use the X-arm or in this instance the proton arm to trigger the photon tagger. The tagger electronics then determined if a coincident electron was detected in the tagger focal plane within a fixed resolving time. During this time the photon tagger scalers are inhibited so that there is no dead time correction necessary for the photon flux normalization. For a real X-arm tagger coincidence this leads to a prompt peak in a spectrum of the tagger TDCs as is evident in Figure 4.6. Here all tagger channels are shown together. This is possible if all the individual peaks are aligned to a common channel, taking into account the various signal delays as well as the varying time-of-flights of the electrons to each of the focal plane detectors.

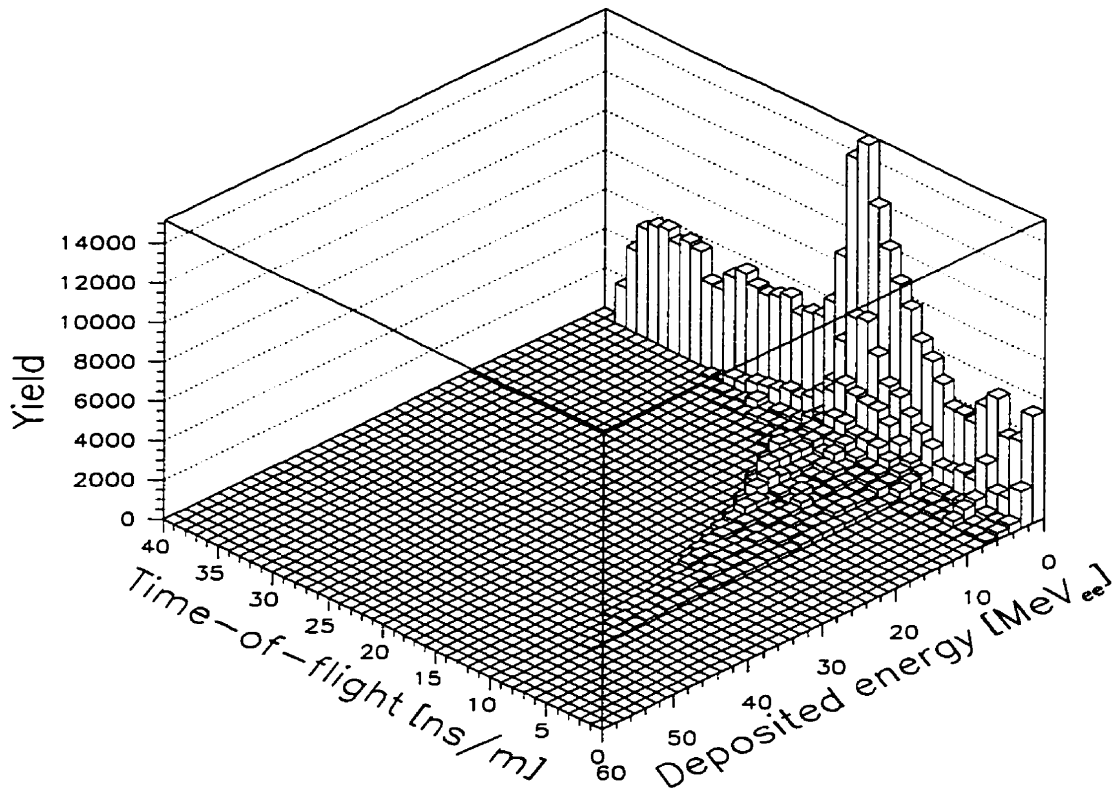

Figure 4.5: Correlation between the deposited energy in the neutron detector and the neutron time-of-flight.

The insert in this figure depicts a FWHM of 16 TDC channels or 1.6 ns. As well as the true coincidences, the prompt peak rests on a background where the electron is purely random with respect to the X-arm particle which triggered the tagger.

4.3.2 Photon energy calibration

With the neutron detector energy and position calibrated, it was possible to calibrate the energy of the tagged photon beam by analysis of the deuterium data, and by making use of the overdetermined deuterium kinematics. That is, if both the neutron kinetic energy T_n and the neutron angle θ_n are known, then the photon energy which

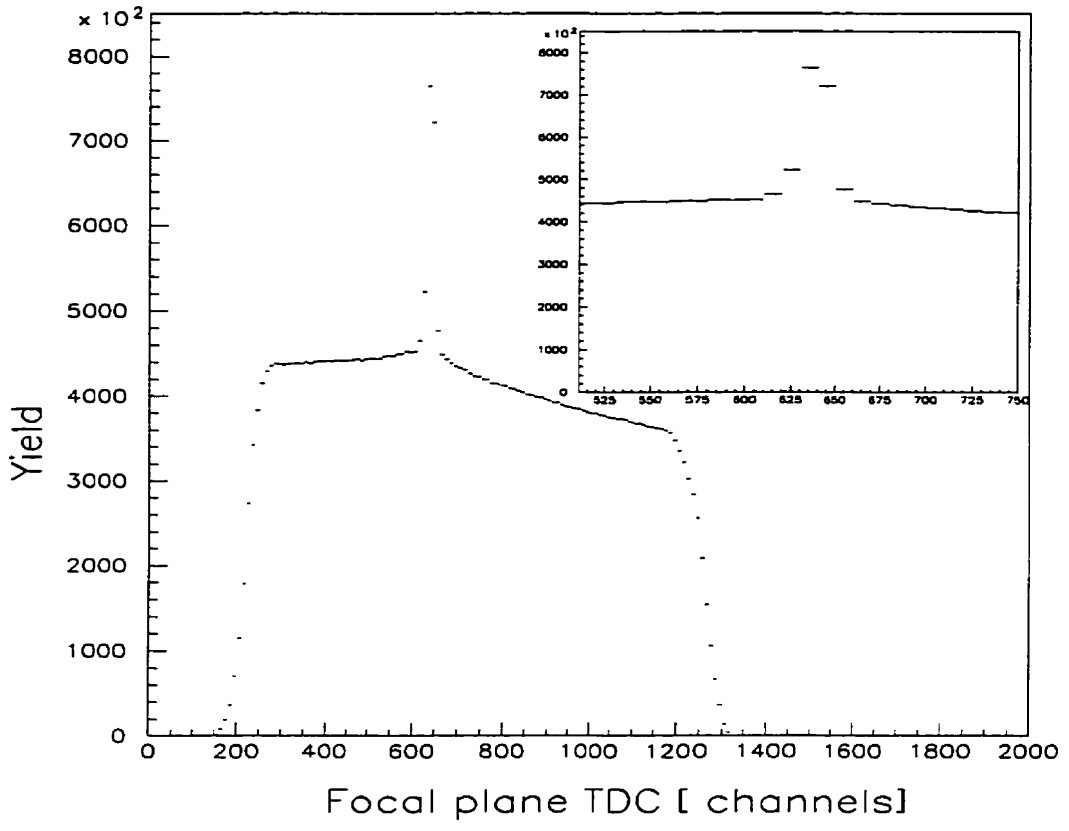

Figure 4.6: Typical tagger TDC spectra with all 62 channels aligned for one of the CsI telescopes. The insert depicts the timing resolution as about 1.6 ns FWHM.

initiated the reaction can be uniquely determined.

Each focal plane detector was calibrated by the above procedure. In order to reduce the background, a 2 MeV_{ee} deposited energy bias was applied to the neutron detectors. In order to determine the peak position and width of each focal plane detector spectrum, a Gaussian fit was applied to the data. Figure 4.7 illustrates a sample fit of one of the focal plane detectors.

Once each tagger focal plane detector was calibrated, a plot of the photon energy versus the focal plane detector number was made. A second order polynomial fit was made to the data as shown in Figure 4.8, so that by using the focal plane detector

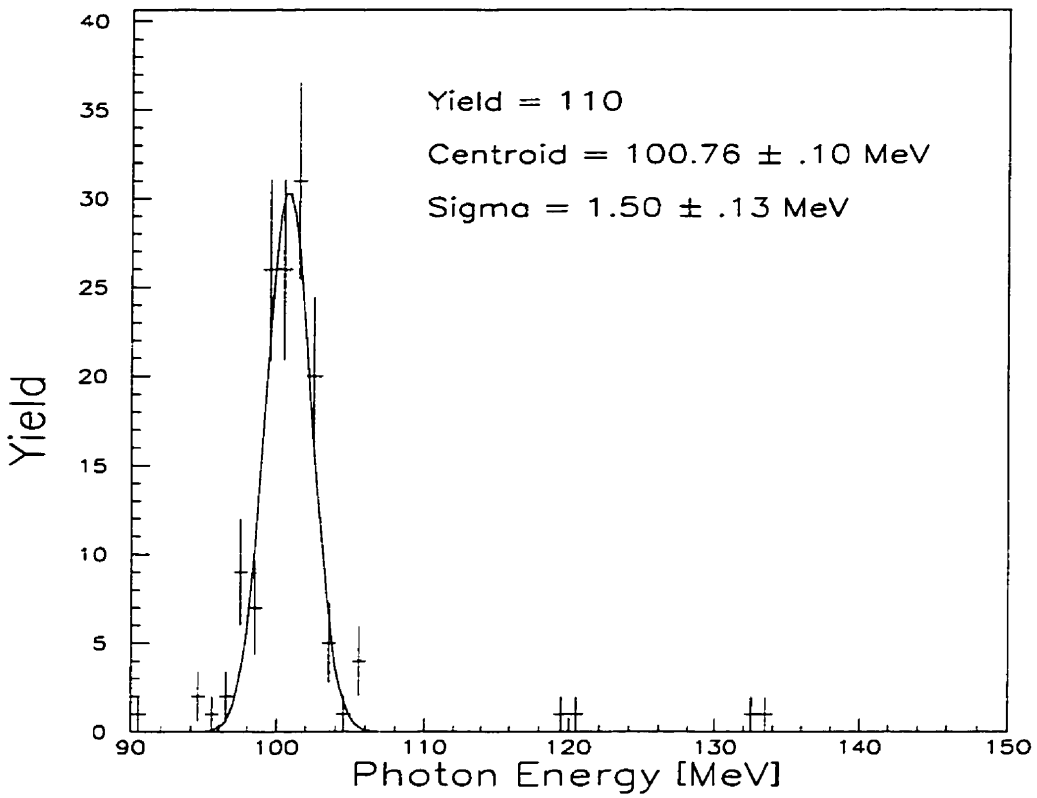

Figure 4.7: Sample fit of the energy calibration for one of the focal plane detectors.

number in the polynomial expression, the photon energy for each focal plane detector could be determined.

4.4 The proton telescopes

4.4.1 Particle identification

The particle identification was performed for the proton telescopes by making use of the fact that particles of different mass, velocity and charge lose energy at different rates as they traverse a material. This experiment was performed at sufficiently low photon energies so that any pions produced would not have sufficient energy to be detected in the CsI crystals. It was necessary to separate protons from the numerous

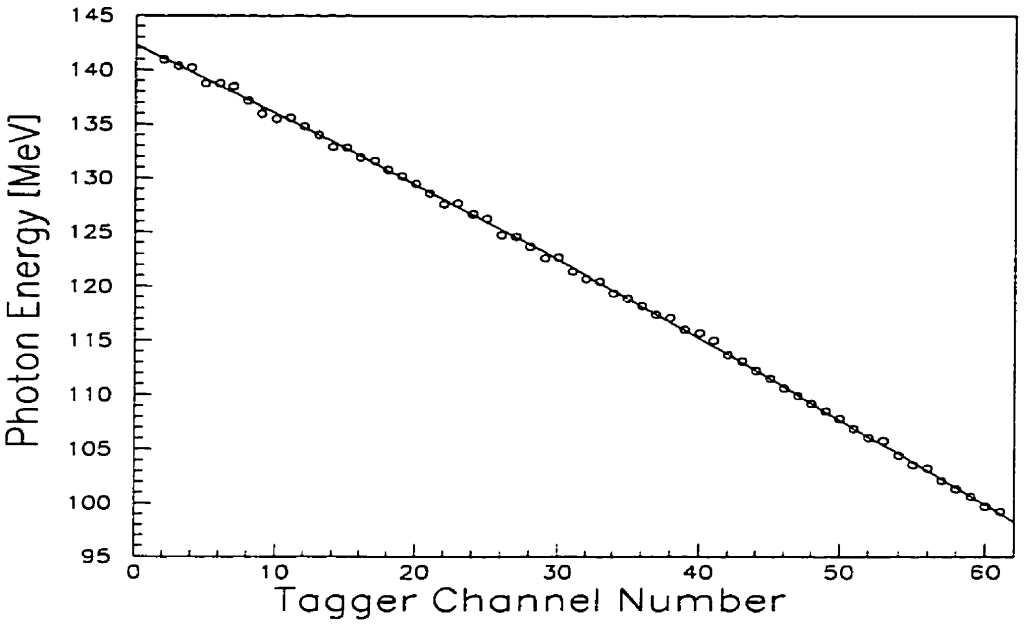

Figure 4.8: Photon energy calibration of the tagger focal plane detectors.

electrons and positrons. The main process that produces this unwanted background is that of pair production where photons are converted into electron/positron pairs in the Coulomb fields of the target nuclei. It was also required that deuterons be separated from protons, although the number of deuterons produced is dramatically less than the number of protons.

As the different species of charged particles, with the same kinetic energy, traverse the proton telescopes' Δ-E detectors, they lose different amounts of energy. They deposit the remainder of their kinetic energy in the CsI crystals. For the particles discussed above, which have for instance the same kinetic energy (all particles have a single elementary charge unit) the separation occurs on the basis of the difference in mass of the particles. This results in the characteristic particle bands seen in Figure 4.9. A cut can then be made on the proton particle band, thereby separating protons from the other particles present. Between the particle bands there is a

small amount of background resulting primarily from nuclear interactions in the CsI crystals. Consider a proton which deposited the correct amount of energy in the Δ-E detector to appear in its correct band. Now suppose the same proton underwent a nuclear interaction in the CsI detector. This results in an energy deposition in the CsI crystal less than the correct amount necessary for the proton to pass the proton band cut. This loss in energy is due to the reaction Q value as well as the production of particles and photons. This effect was studied using a GEANT Monte Carlo simulation so that a correction could be made to the data. This correction ranged from about 5% for a proton kinetic energy of 80 MeV down to about 1% for a proton energy of 25 MeV.

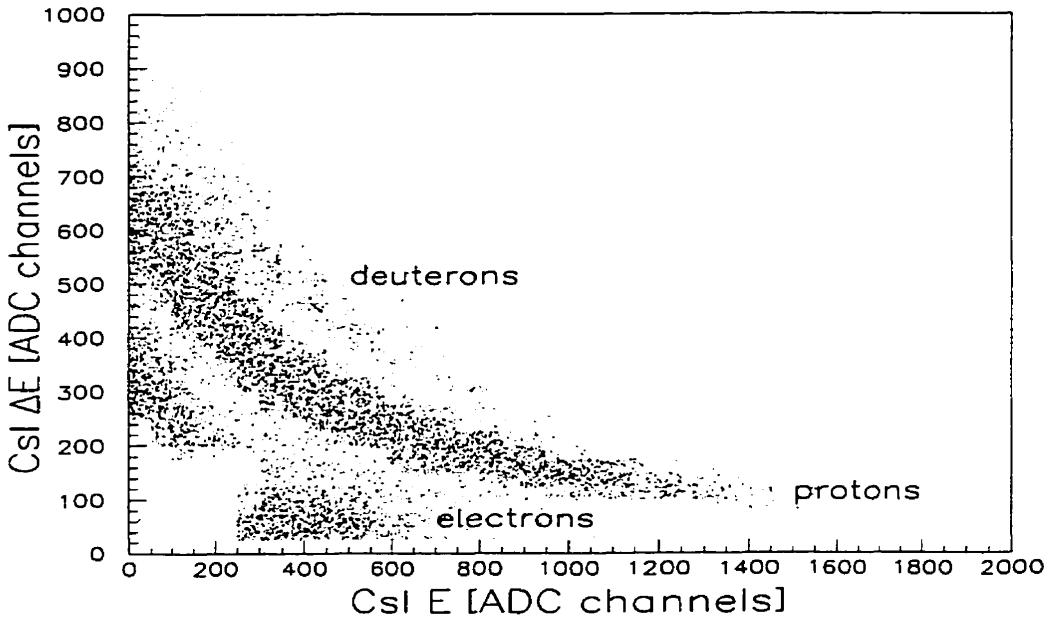

Figure 4.9: Typical scatter plot for one of the proton telescopes. The energy deposited in the Δ-E detector is plotted as a function of the energy deposited in the CsI E detector. Clear particle bands are depicted. Also shown in the bottom left hand corner of the figure is the effect of the hardware box cut.

In the bottom left hand corner a hardware box cut (see section 3.3.3) can be seen.

This eliminated the large number of low energy electron events, and thus served to greatly reduce the amount of unwanted data written to tape.

4.4.2 Proton energy calibration

With the neutron detectors calibrated it was possible to calibrate the CsI detectors by making use of the kinematically complete $^2H(\gamma, pn)$ reaction. That is, by knowing the neutron kinetic energy, T_n, and the neutron detection angle, θ_n, it is possible to determine the corresponding unique proton energy. A 2 MeV_{ee} threshold was imposed on the deposited energy in the neutron detectors in order to greatly reduce the low energy background events. A cut was imposed on the proton detector so that the particle was identified as a proton via the Δ-E E scatter plot. The angular resolution of the neutron detector was better than 1°. For a given neutron, T_n, without use of the neutron angle, θ_n, the uncertainty in the proton energy due to the finite acceptance of the proton telescope was approximately 5 MeV due to the $\pm$ 7° uncertainty in θ_p. However, making use of the neutron angle reduced the uncertainty of the proton energy to less than 0.5 MeV.

Now that the proton energy is known at the point of interaction within the target, the deposited energy in the CsI detector can be found by calculating the energy loss of the proton through all material before detection in the CsI detector. That is, the deposited energy in the CsI detector is given by

$$E_{CsI} = T_{p_{target}} - E_{target} - E_{air} - E_{\Delta-E} - E_{window} \tag{4.20}$$

where the energy loss is calculated in the sequence given in the above equation. In Eq. 4.20, E_{CsI} is the net deposited energy in the CsI crystal; $T_{p_{target}}$ is the proton

kinetic energy as given from deuterium kinematics; E_{target} is the energy deposited in the target material (assumed to originate at the center of the target) followed by the energy loss in the target's kapton window; E_{air} is the proton energy loss in the air; $E_{\Delta-E}$ is the proton energy loss in the tape and aluminum on the front face of the Δ-E detector followed by the energy loss in the 2 mm plastic scintillator and by the energy loss in the aluminum and tape as the proton exits the Δ-E detector; and E_{window} is the proton energy loss in the thin light-tight paper coating and the aluminum window of the CsI detector. The target rotation angle was chosen to minimize the proton energy loss in the target and was accounted for in the energy loss calculation. The energy losses were calculated by using the Bethe Bloch energy loss formula [49].

With the proton energy deposited in the CsI detector known, the gain as a function of the proton ADC value (pedestal subtracted) could be determined. A quadratic fit of the energy deposited, E_{CsI}, as a function of the CsI ADC channel number was found to give the best reduced chi-square fit. Since the light output produced in the CsI crystal is not a linear function of the deposited energy for protons, it is not surprising that the fit was not best described as linear. For the calibration, the proton energy ranged from approximately 45 MeV to 65 MeV. When a proton was detected from a reaction other than the $^2H(\gamma, pn)$ reaction, the above procedure was run in reverse so as to determine the proton energy assumed to be produced at the center of the target. Figure 4.10 shows the result of the fit to the proton energy calibration data for one of the CsI detectors.

4.5 Solid angle

The solid angle subtended by a circular collimator with a radius r_c at a distance d from a point is given by

$$d\Omega = 2\pi(1 - cos\phi). \tag{4.21}$$

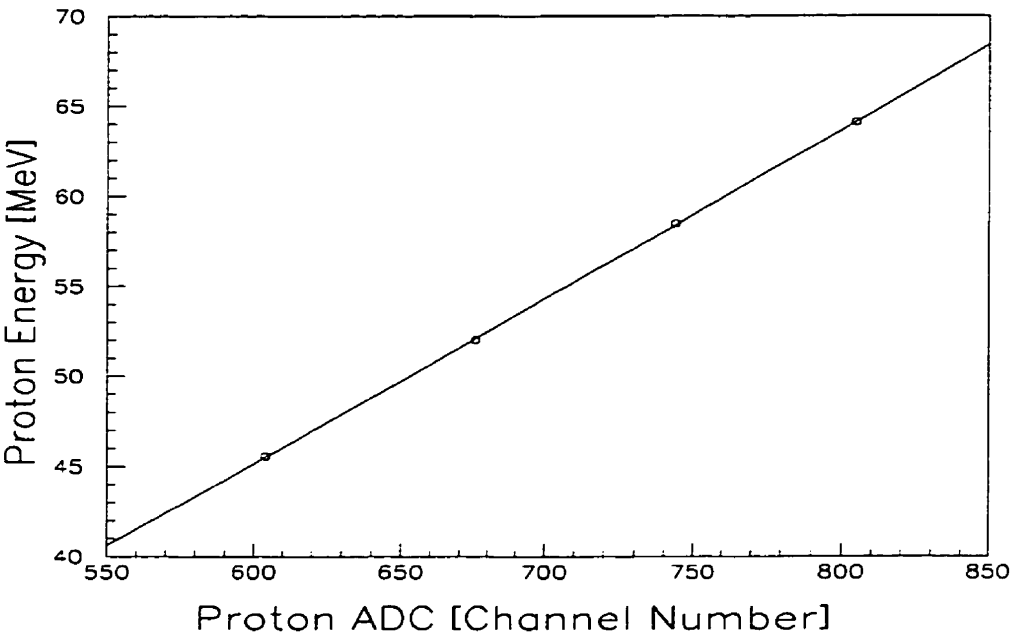

Figure 4.10: Proton energy calibration for one of the proton detectors. The error bars are smaller than the data points.

In Figure 4.11 the angle ϕ is defined as the angle between the line connecting the target to the center of the collimator and the line to the outer edge of the collimator.

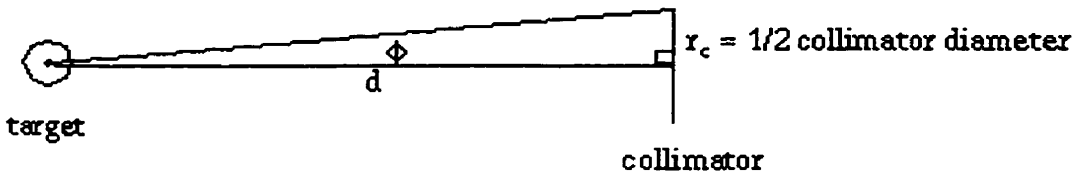

Figure 4.11: Geometry for determination of the solid angle from a point source.

The proton detector solid angle was also calculated analytically taking into account the finite size of the beam spot on the target, the target rotation angle and the collimator size. The method is described in Reference [4]. For comparison, the solid angle subtended by the proton telescope was also determined by use of a GEANT simulation, which also took into account the effects of the extended target, target rotation angle, collimator size and multiple scattering of protons in the air and target. Protons were generated so as to uniformly populate a spherical shell. A kinematical cut was applied so that protons which lost more than 1 MeV in the collimator were rejected as candidate hits.

The solid angle is given by the number of protons detected in the CsI detector divided by the number of events generated multiplied by 4π or

$$d\Omega = \frac{N_{detected}}{N_{generated}} 4\pi. \tag{4.22}$$

The statistical uncertainty of the Monte Carlo simulation was approximately 1%. The results of the point target and extended target solid angle calculations are given in Table 4.1. The analytical and Monte Carlo results are found to be in good agreement.

The neutron solid angle was calculated using a GEANT simulation in a similar manner and the results are also given in Table 4.1. The neutron solid angle for the third CsI(Tl) was not evaluated since no (γ, np) data are presented due to its poor

resolution. The neutron detector solid angle as derived from simulations (for example CsI detector number 1 $\theta_p = 82°$) can be checked by use of the equation

$$d\Omega = \frac{ab}{h(a^2 + b^2 + h^2)}. \tag{4.23}$$

This analytical expression [50] gives the solid angle subtended by a rectangle with dimensions a times b from a point which is a perpendicular distance h from the corner of the rectangle. The result of this calculation predicts the solid angle of the neutron detector to be $d\Omega = 45.0$ msr. The solid angle calculated by simulations is found to be in satisfactory agreement with that calculated using this analytical expression.

Table 4.1: Solid angle of proton telescope and neutron detector.

Detector Number	Ω^{proton}_{point} $(10^{-3}sr)$	$\Omega^{proton}_{simulation}$ $(10^{-3}sr)$	$\Omega^{proton}_{analytical}$ $(10^{-3}sr)$	$\Omega^{neutron}_{simulation}$ $(10^{-3}sr)$
1	58.5	56.5	56.9	45.3
2	58.5	56.7	56.8	47.1
3	58.5	56.3	56.6	—

4.6 Neutron detection efficiency

Since the experiment was performed with a D_2O target, the neutron detection efficiency could be determined experimentally from the photodisintegration of the deuteron. The major complication which enters into extracting the neutron detection efficiency, results from the fact that the extended beam spot on the target tends to smear the angular correlation measured by the proton and the neutron detectors. It was therefore necessary to use Monte Carlo simulations in order to extract the

absolute neutron detection efficiency which is independent from the geometrical differences in the acceptances of the proton and neutron detectors and the effects of the extended target.

For instance, if the neutron and proton detectors had an infinitely small solid angle, the target was not an extended target, the photon energy was singular and the geometrical opening angle of the proton and neutron detector was exactly matched to the deuterium kinematics for that photon energy, then the neutron detection efficiency would simply be the ratio of the number of neutrons detected in the neutron detector divided by the number of protons detected in the proton detector. When not all of these conditions are true it is necessary to use simulations to determine the true neutron detection efficiency as a function of the incident neutron energy.

The procedure to determine the neutron detection efficiency in light of the above considerations is as follows. The yield of protons, Y_p, detected by the proton detector is proportional to

$$Y_p \propto d\sigma d\Omega_p \tag{4.24}$$

where $d\sigma$ is the differential $^2H(\gamma,p)n$ cross section for the corresponding photon energy and proton detection angle. Since the proton detector was used as the trigger for the read-out of the electronics, the number of neutrons detected will depend on the kinematical angular correlation and on the finite size of the beam spot on the target. Hence the number of neutrons detected by the neutron detector is proportional to

$$Y_n \propto d\sigma d\Omega_n F_{Acc}^{extended}(E_\gamma) \tag{4.25}$$

where we define $F_{Acc}^{extended}(E_\gamma)$ as the effective reduction in the neutron solid angle due to the acceptance effects between the two detectors, which includes the fact that the

two particles are correlated. Dividing equation 4.25 by equation 4.24 and solving for $F_{Acc}^{extended}(E_\gamma)$ yields the following equation

$$F_{Acc}^{extended}(E_\gamma) = \frac{Y_n d\Omega_p}{Y_p d\Omega_n}. \tag{4.26}$$

A simulation using the exact experimental geometry with the requirement that a proton of the correct kinematics was detected and a corresponding neutron with the correct kinematics was incident on the neutron detector then yields the acceptance correction for the neutron detection efficiency $F_{Acc}^{extended}(E_\gamma)$. Deuterium kinematics was used to describe the correlation between the proton and neutron, and a two-dimension Gaussian distribution which reproduced the known tagging efficiency was used to describe the photon distribution on the extended target. The values for $F_{Acc}^{extended}(E_\gamma)$ are given in Table 4.2. For comparison, the simulation was performed for a point target so that $F_{Acc}^{point}(E_\gamma)$ was obtained and the results are also given in the Table. It can be seen from the point target results presented that the acceptance corrections to the neutron solid angle decrease systematically with E_γ as is expected for deuterium kinematics. The $F_{Acc}^{point}(E_\gamma)$ values approach the ratio of the proton and neutron solid angle ratio of 0.80 for the last two photon energy bins. This indicates that the opening angle of the proton and neutron detector for CsI detector number one is best matched for a photon energy of about 130 MeV. On the contrary, when the simulations are performed for the extended target, the acceptance is seen to decrease dramatically and the photon energy dependence is smeared out.

The neutron detection efficiency was then extracted from the measured yield of protons $Y_p^{measured}$ and neutrons $Y_n^{measured}$. These yields were obtained from histograms of excitation energy spectra using deuterium kinematics. The prompt dis-

tribution of the excitation energy spectra was corrected for the tagger random background and empty target contributions. The measured neutron detection efficiencies unfolded from the geometry of the setup, and the correlation of the proton and neutron is then given by

$$\epsilon^{unfolded} = \frac{Y_n^{measured}}{Y_p^{measured} F_{Acc}^{extended}(E_\gamma)}. \tag{4.27}$$

A 2 MeV_{ee} cut on the energy deposited in the neutron detector was imposed in obtaining $Y_n^{measured}$ and the entire neutron array was averaged together. The experimental neutron detection efficiencies are listed in Table 4.2.

Table 4.2: Parameters necessary to unfold the true neutron detection efficiency from the experimental measured efficiency for CsI detector number 1 ($\theta_p = 82°$). The errors are due to the statistical errors of the measurement only.

E_γ^{Sim} (MeV)	E_γ^{Tag} (MeV)	$F_{Acc}^{point}(E_\gamma)$	$F_{Acc}^{extended}(E_\gamma)$	Exp. (%) Efficiency	T_n^{Tag} (MeV)	Unfolded (%) Efficiency
65	67	.45	.34	6.0 ± .3	32.7	17.6 ± 0.9
75	82.5	.51	.37	5.8 ± .4	40.1	15.7 ± 1.1
85	97.4	.58	.37	5.4 ± .4	47.9	14.6 ± 1.4
95	112.9	.63	.37	5.0 ± .5	55.9	11.8 ± 1.3
105	103.7	.70	.38	4.5 ± .2	51.7	11.8 ± 0.5
115	115.6	.73	.38	4.8 ± .2	57.7	12.6 ± 0.5
125	126.7	.75	.38	4.4 ± .3	63.2	11.6 ± 0.8
135	137.4	.75	.38	4.4 ± .3	68.5	11.6 ± 0.8

Figures 4.12 and 4.13 graphically depict the results of the measured efficiencies as a function of the incident neutron energies. The extracted neutron detection efficiencies are in very good agreement with the results for the plastic scintillator given in Reference [51]. The dotted line in Figure 4.12 is the result of GEANT simulations using the FLUKA hadronic interaction code [52]. A 2 MeV_{ee} threshold was applied for the energy deposition in the neutron scintillators and careful attention

was paid to account for the difference in light output of hadrons and leptons in the simulations. All ten neutron bars were averaged together. The statistical error in the simulated results $F_{Acc}^{extended}(E_\gamma)$, needed to extract the absolute neutron detection efficiency from the measured data, was approximately 2% to 3 %. For neutron energies above 50 MeV the simulation reproduces the shape of the efficiency reasonably well; however, the simulation underpredicts the measured efficiency by approximately 25%. Below a neutron energy of 50 MeV, the simulation is seen to be in worse agreement, not predicting the correct trend in the neutron detection efficiency. The failure of the FLUKA cross section tables at low energies is perhaps not surprising since the CERN codes were developed and maintained for high energy physics applications. In a recent study of neutron transport codes [53] large discrepancies were found for the various codes. In some cases however, most of the codes seem to agree with experimental data to about the 10% level. Grobatkov and Kryuchkov [53] do, however, report some discrepancies between measurements and simulations using the FLUKA generated cross sections.

4.7 Target normalization

Although target profiles were measured at the beginning and end of the experiment, the target thicknesses were assumed to be unknown. The target thickness depends on the location of the beam spot on the target (since the target thickness was not uniform), the accuracy of the rotation angle and the amount of minute air bubbles introduced when filling the targets. Therefore, it was decided to normalize the target thickness to the well-known deuterium differential cross section. With more than 115,000 counts from the $^2H(\gamma, p)n$ reaction per detector an extremely good statistical accuracy was obtained for each proton angle. The photon energy was binned in approximately 10 MeV bins and an average of the 4 obtained target thicknesses

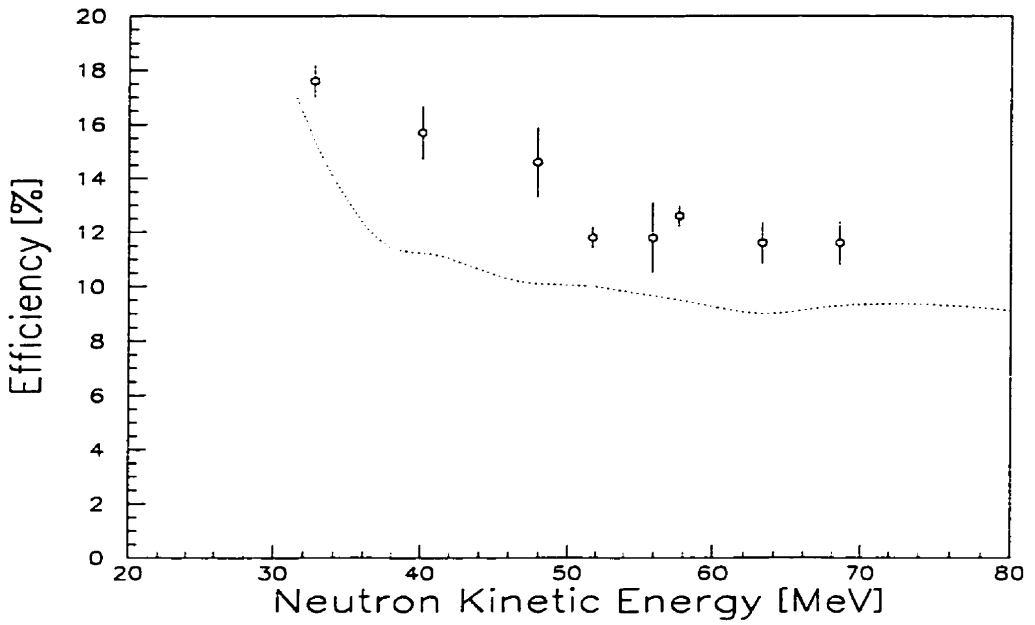

Figure 4.12: The unfolded neutron detection efficiency versus the neutron kinetic energy for CsI number 1 $\theta_p = 82°$. The error bars are statistical only.

was used. The measured cross sections were compared to a fit to the world's data performed by Rossi *et al.* [54]. The Rossi code was found to be in good agreement with the recent measurement of Crawford *et al.* [55] and references therein. The 4 target thickness determinations per target were found not to vary by more than 5% from each other. The uncertainty in the target thickness is estimated to be 7%.

4.8 Random subtraction

The procedure of random subtraction for a single arm coincidence experiment is straightforward. A peak in the tagger TDC spectrum results from a coincidence between a proton and an electron detected in the tagging focal plane (see Figure 4.6). The start of the tagger TDC is generated by a signal in the proton arm Δ-E detector while the stop is caused by an event in one of the tagger focal plane detectors.

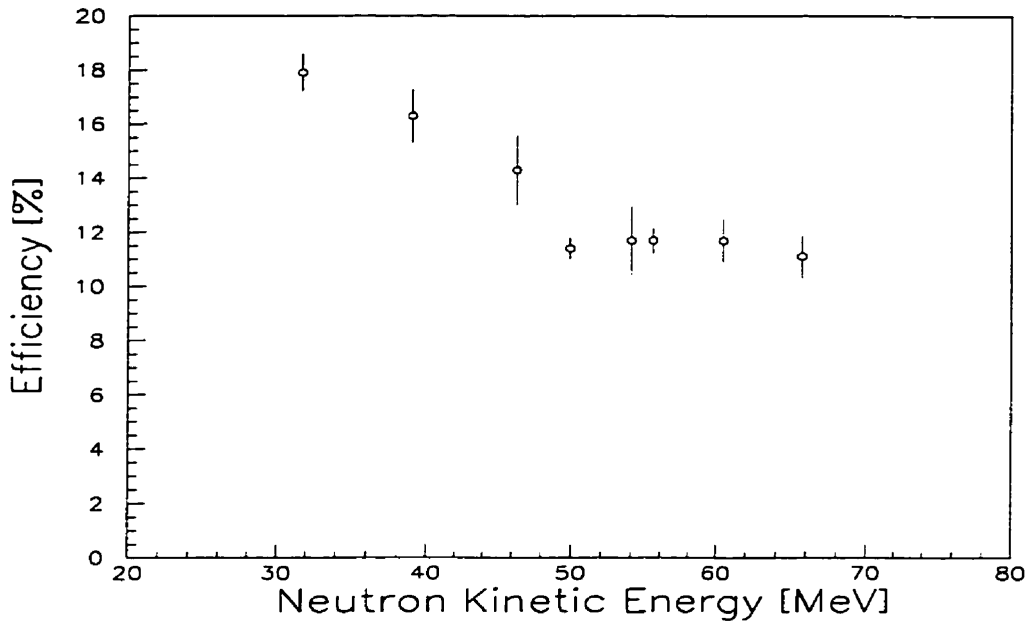

Figure 4.13: The unfolded neutron detection efficiency versus the neutron kinetic energy for CsI number 2 $\theta_p = 76°$. The error bars are statistical only.

The prompt peak rests on a random background where the electron detected in the tagging focal plane was not correlated with the detected proton. To remove these random electron events one simply makes spectra for an equal area of the tagger TDC spectrum outside the region of the prompt peak. Subtraction of the random spectrum from the prompt spectrum then results in the true yield of prompt events for an electron proton coincidence.

For a triple coincidence experiment a much more complicated situation arises. Figure 4.14 is a plot of the neutron array TOF versus the tagger TDC. This spectrum was accumulated under the condition that the energy deposited in the neutron detector be larger than 2 MeV_{ee}, which was shown to significantly reduce the level of random neutron events. In this figure prompt and various random regions exist as is discussed below. The narrow ridge positioned at a neutron TOF of 23 ns running parallel to the tagger TDC axis corresponds to the gamma flash used to calibrate the

neutron array and is not a source of background to the prompt region. Unlike the simple picture which exists for double coincidence experiments there are five combinations of correlated and uncorrelated signals for the case of a triple coincidence. The relative yield of the different classes of background depends on the ranges of tagged and untagged bremsstrahlung photons present, the acceptances of the detectors, and the background radiation in the experimental area. Experiments performed under different circumstances (such as the tagging rate, beam energy, target material, etc.) result in greatly different levels for each random event category.

The five possible combinations mentioned above are as follows. First is the true coincidence peak where all three particles are correlated, appearing as a ridge running parallel to the neutron TOF axis. This ridge starts at neutron TOF of 55 ns and continues to TOF values of 200 ns which is the dynamical range of the TDC. Second are events in which the proton and electron are correlated but the neutron is not correlated, appearing as a ridge running parallel to the neutron TOF axis and covering the entire range of neutron TOF values displayed. The level of this background is constant throughout the entire TOF spectrum. Events making up this ridge which occur before the gamma flash require velocities greater than the speed of light and must be purely random events. Analysis of this region will yield the correct level of this component of the background to be subtracted from the prompt region.

Third are events in which the neutron and proton are correlated but the electron is not correlated, appearing as a dominant ridge running parallel to the tagger TDC axis. Due to the high tagging rates in this experiment this is the dominant source of background to the prompt region. Fourth and possibly obscured by this dominant ridge of background events, are events in which the electron and neutron are correlated and the proton is not correlated. However, in previous experiments which had very clean time signatures this ridge has never been observed to be a significant source of

background. The signature for this type of random event would be a ridge running at a 45 degree angle to the random electron and random neutron ridges. Fifth and finally the entire spectrum rests on a background of events in which all three particles are uncorrelated.

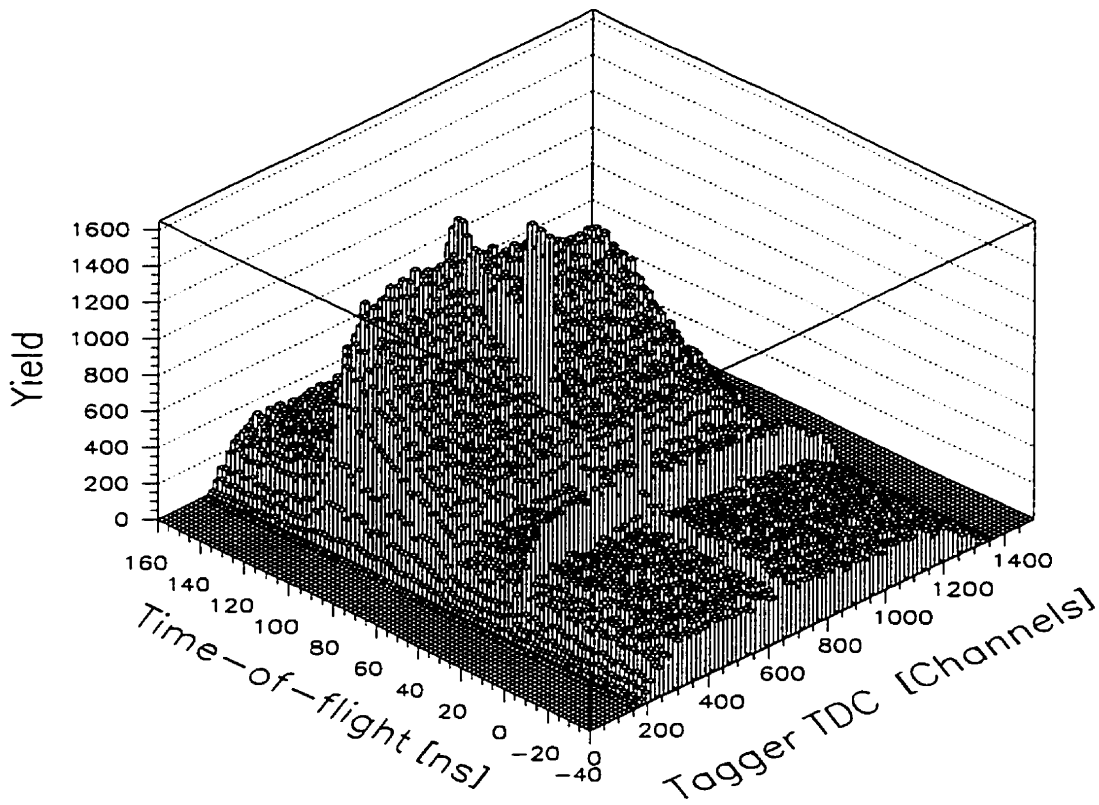

Figure 4.14: Neutron time-of-flight versus the tagger TDC showing regions of prompt and random coincidences.

The shape of these background events was determined as a function of neutron TOF values in the following manner. A tagger TDC spectrum was made for each 10 ns bin of neutron TOF values. The bin size was chosen for statistical reasons. For kinematically allowed neutron TOFs the level of the random background beneath the prompt peak was determined. To these values a constant level of background neutron

events were added by determining the prompt yield of neutrons occurring in the time region before the gamma flash where the neutrons must be random in nature. The shape of all classes of background events has now been determined as a function of neutron TOF.

For each prompt event 100 background events were generated by choosing a random neutron TOF and a random number for the background height where the choice of random height was normalized to the largest measured background level. If the randomly chosen height for that particular neutron TOF was above the corresponding measured background level the event was discarded and a new neutron TOF and random height was generated. A linear interpolation was used for level of background between each neutron TOF bin. In this way the random background shape was generated as a function of the neutron TOF and is demonstrated in Figure 4.15. For comparison, the shape of the prompt neutron TOF is given in Figure 4.16. It is obvious that the 10 ns neutron TOF bin was too large to reproduce in the random neutron TOF spectrum, the sharp rise and fall seen in the prompt neutron TOF spectrum. It was therefore necessary to impose a cut on the neutron kinetic energies so as to avoid areas of the spectrum where the sharp rise and fall of the neutron TOF spectrum did not match that of the prompt spectrum. This resulted in a kinematical acceptance of neutron energies 25 MeV $\leq T_n \leq$ 80 MeV. Considering the photon energies involved, this kinematical cut did not appreciably influence the phase space acceptance of coincident proton-neutron events, resulting from the $^{16}O(\gamma, pn)$ reaction, in which the neutron was ejected without undergoing a final state interaction (FSI).

For all random spectra which depended on the neutron kinetic energy, the TOF value was used, which reproduced the level of random background events as generated by the above procedure. For instance, excitation spectra were made in the following

manner. The excitation energy of the recoil nucleus is given by

$$E_x = E_\gamma - T_p - T_n - T_r - Q, \tag{4.28}$$

where E_x is the excitation energy of the A-2 recoil nucleus, Q is the reaction threshold, E_γ is the photon energy, and T_p, T_n and T_r are the proton, neutron and recoil nucleus kinetic energies respectively. A cut three times the width of the prompt peak was made in the random part of the tagger TDC spectrum. The recoil energy is reconstructed from the measured proton and neutron momenta. For each random event, the random proton energy was used (this is known to be the correct distribution as was demonstrated by the single arm random subtraction) and 100 random neutron energies were generated to make the excitation energy spectra for random events. The neutron energy was determined by choosing a random neutron TOF as discussed above, while the scintillator bar and hit position along the bar were chosen isotropically.

4.9 Background subtraction

In order to find the contribution of background events to the foreground, one third of the experimental run time was used for empty target runs. From these runs the contribution from the air surrounding the target and from the mylar windows could be determined, so that this unwanted background could be removed from the foreground. The analysis of the background for each reaction was performed in exactly the same way as the foreground data. The background data were then scaled so that both the foreground and background data were normalized to the same number of incident photons before subtraction of the background was performed.

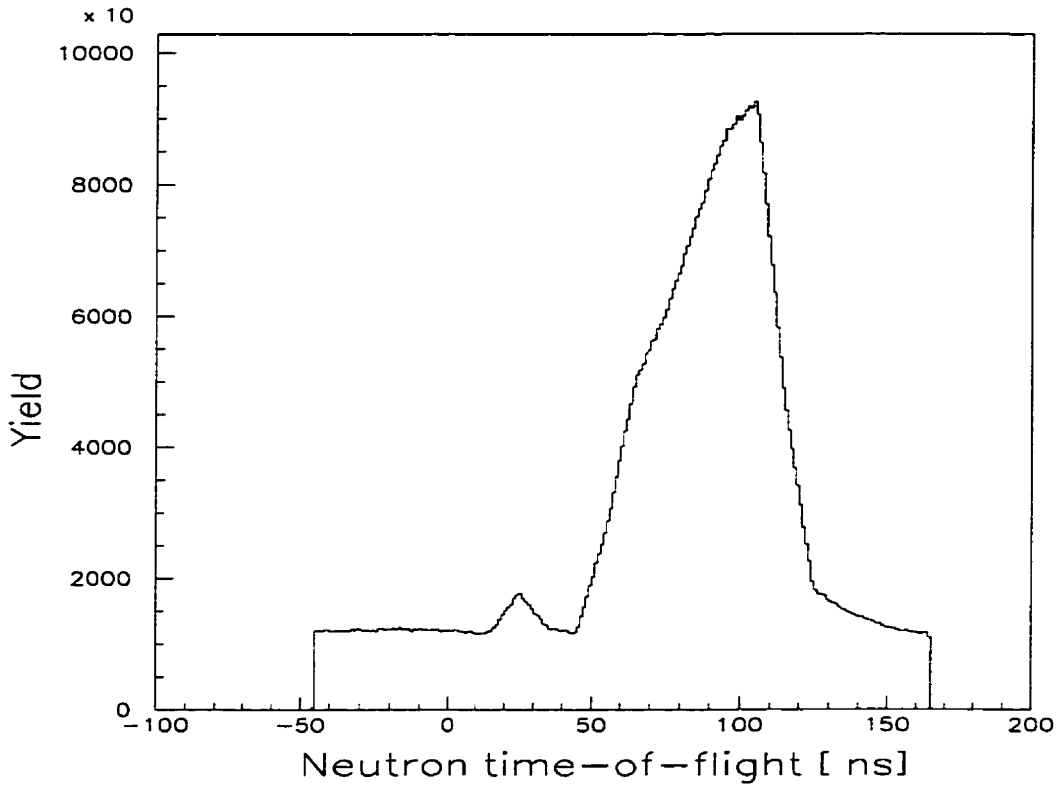

Figure 4.15: Random generated neutron time-of-flight spectrum.

4.10 Determination of the experimental cross sections

The deuterium cross section was computed using the following formula

$$(\frac{d\sigma}{d\Omega_p})_D = \frac{Y_p A sin(\theta)}{N_e d\Omega_p \varepsilon_{tag} (\rho t)_D W_D N_O \varepsilon} \tag{4.29}$$

where Y_P is the yield of protons, A is the atomic mass of the target, θ is the target rotation angle, N_e is the yield of electrons detected in the tagger focal plane, $d\Omega_p$ is the solid angle subtended by the proton detector corrected for the effects of the extended target, ε_{tag} is the tagging efficiency, ρt is the number of target nuclei per

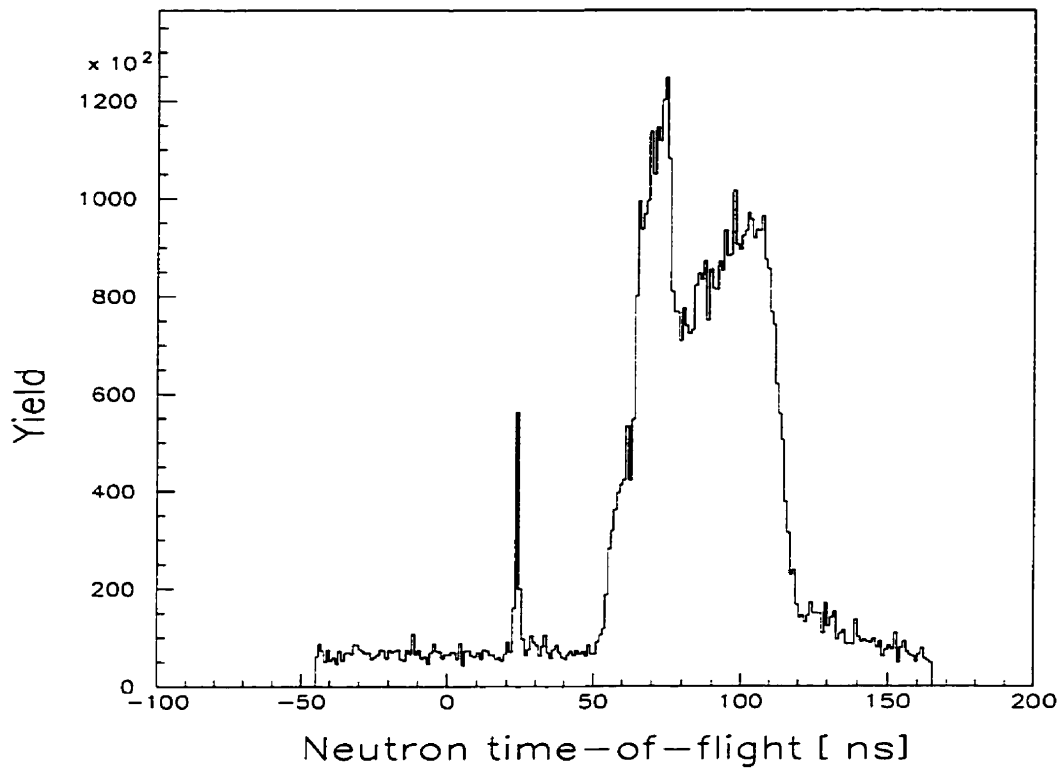

Figure 4.16: Prompt neutron time-of-flight spectrum.

cm^2 (the target thickness was assumed to be the desired 1 mm thick), W_D is the corresponding weight of deuterium atoms in the heavy water, N_O is Avogadro's number and ε accounts for the correction necessary for pile-up and nuclear interactions in the proton detector. The deuterium cross sections were then compared to the Rossi parameterization [54] of experimental data in order to determine the absolute target thickness. That is, the target thickness normalization constant, N_R, is defined via the relation $(d\sigma/d\Omega_p)_{Rossi} = N_R(d\sigma/d\Omega)_D$. For evaluation of the $^{15}N_{g.s.}$ cross section Equation 4.29 was multiplied by the constant N_R necessary for the measured deuterium cross sections to agree with the Rossi prediction and the atomic number A and the weight used, W_O, corresponded to the oxygen content present in the heavy water target.

For the exclusive $^{16}O(\gamma,pn)^{14}N_{0,1,2,..}$ the cross sections were computed by the following equation

$$\frac{d\sigma}{dE_x d\Omega_p d\Omega_n} = \frac{Y_p A sin(\theta) N_R}{N_\gamma dE_x d\Omega_p d\Omega_n \varepsilon_{eff} \varepsilon_{tag}(\rho t) W_O N_O \varepsilon} \tag{4.30}$$

where dE_x is the excitation energy bin width, ε_{eff} is the measured neutron detection efficiency, $d\Omega_n$ is the neutron detector solid angle, W_O is the corresponding weight of oxygen atoms in the heavy water and all other symbols are as defined in Eq. 4.29. Note that the product of the solid angles $d\Omega_p d\Omega_n$ is strictly correct for completely uncorrelated particles. In the following section the product of the proton and neutron solid angles, resulting from the fact that the proton and neutron have a non-isotropic angular correlation, will be evaluated.

4.11 Normalization for the $^{16}O(\gamma,pn)^{14}N_{0,1,2,..}$ measurement

Before Eq. 4.30 can be applied to determine the absolute cross section, a few normalization concerns need to be addressed. Only one discrete state was observed in the $^{16}O(\gamma,pn)^{14}N_{0,1,2,..}$ reaction for this experiment. The excitation energy spectrum for one of the CsI detectors resulting from the $^{16}O(\gamma,pn)^{14}N_{0,1,2,..}$ reaction in the photon energy range from 100 to 140 MeV is depicted in Figure 4.17. Figure 4.17 a) is the excitation energy spectrum for a cut on the tagger prompt peak. Figure 4.17 b) is the excitation energy spectrum generated for the random contribution under the tagger prompt peak as described in Section 4.8. Figure 4.17 c) is the resulting spectrum after the random contributions have been removed. Here it is evident that only the 3.95 MeV state in the residual ^{14}N nucleus is significantly populated. The unambiguous identification of this state will be demonstrated in Chapter 5. The neutron

detection efficiency has not been applied, as the energy of the random contribution is not truly known for a measurement of the particle's energy via a TOF measurement. The yield, centroid and FWHM of a Gaussian fit with an isotropic background are given in the figure caption.

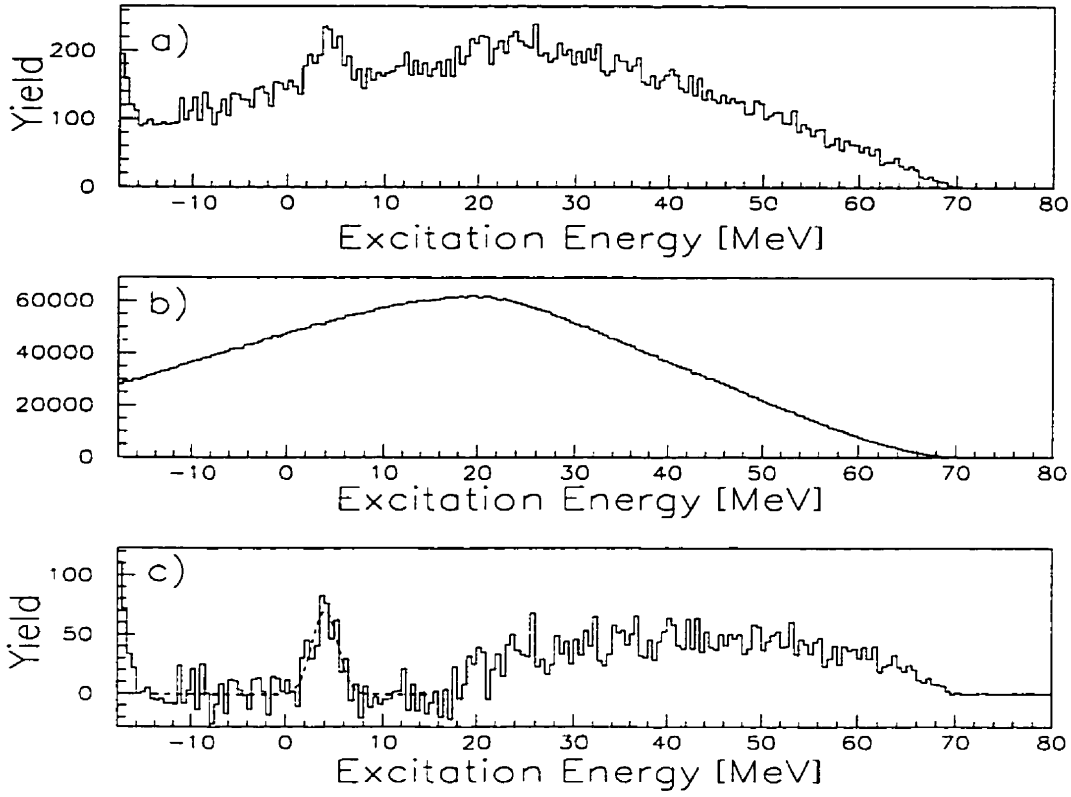

Figure 4.17: The excitation energy spectrum for the $^{16}O(\gamma, pn)^{14}N$ reaction for the photon energy range from 100 to 140 MeV. Figure a) was constructed with a cut on the photon tagger TDC prompt peak. Figure b) represents the random background contribution. Figure c) is the net missing energy yield spectrum with the random contribution subtracted. The spectra are for CsI detector number two (θ_p = 76°. The yield in the fit to the 3.95 MeV state is 470 counts. The centroid of the Gaussian fit is 4.0 ± 0.1 MeV. The FWHM of this state is 3.0 MeV.

The empty target contribution to the 3.95 MeV state is shown in Figure 4.18. The labels on Figures a) through c) have exactly the same meaning as for Figure 4.17. The

results represent the contribution to the excitation energy spectrum of Figure 4.18 resulting from the empty target. In order to obtain sufficient statistics, the background data was binned in 4 MeV bins. The background contribution to the 3.95 MeV state was then identified as the integrated yield from 0 to 8 MeV of excitation energy. The background contribution when normalized to the same photon flux as the foreground was found to be less than 5 % of the foreground.

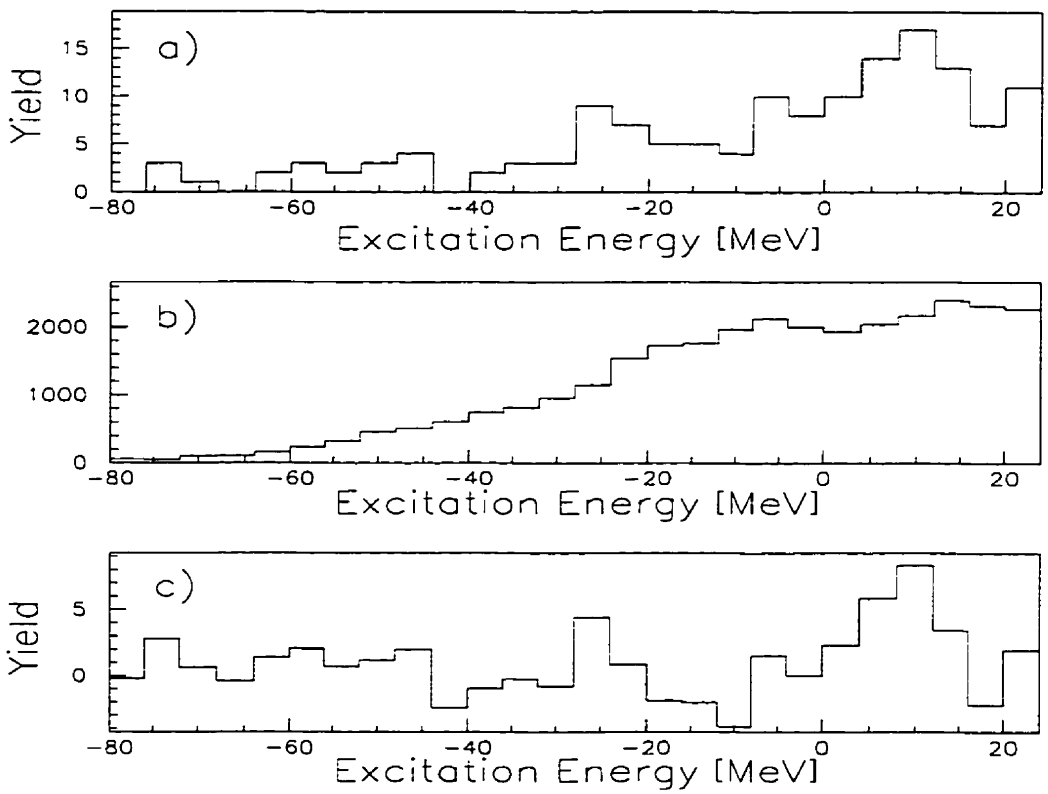

Figure 4.18: The empty target contribution to the 3.95 MeV state in ^{14}N for CsI detector number two, $\theta_p = 76°$. Figures a) - c) have the same meaning as Figure 4.17. The empty target contribution to the 3.95 MeV state is less than 5%.

It was decided to extract only the absolute cross section for the 3.95 MeV state, since in order to extract the absolute cross section, information on the angular cor-

relation of the emitted nucleons is required. In order to find the correction to the neutron detector solid angle resulting from the correlated emission of the proton and neutron, the angular correlation of the emitted nucleon pair must be known. The angular correlation information for the 3.95 MeV state in ^{14}N is known from a previous measurement [11]. Simulations assuming an isotropic cross section for the (γ, pn) reaction over the proton angular acceptance were performed. To accomplish this, deuterium kinematics were used for the photon energy range 60 to 140 MeV. The proton angle was set by deuterium kinematics and the neutron angle of emission was that expected for deuterium kinematics convoluted with the angular correlation distribution of Reference [11]. The extended target distribution (Gaussian) was used and the ratio of the number of neutrons detected to the number of protons detected gives the ratio of the effective neutron solid angle in terms of the proton solid angle. The relation between the proton solid angle and the neutron solid angle is given by

$$\frac{N_{neutrons}}{N_{protons}} = F_{Acc}^{extended}(E_\gamma) = \frac{d\Omega_n}{d\Omega_p} \tag{4.31}$$

where $F_{Acc}^{extended}(E_\gamma)$ represents the geometrical acceptance of the neutron solid angle in relation to the proton solid angle. The neutron solid angle in Eq. 4.30 should be replaced by

$$d\Omega_n = d\Omega_p F_{Acc}^{extended}(E_\gamma) \tag{4.32}$$

Due to the large extended target the geometrical factor $F_{Acc}^{extended}(E_\gamma)$ was found to be independent of photon energy. The factors $F_{Acc}^{extended}(E_\gamma)$ were found to be 0.27 and 0.25 for CsI detectors number one ($\theta_p = 82°$) and number two ($\theta_p = 76°$), respectively. The estimated systematic error in the determination of the neutron solid angle resulting from the above procedure is 5%.

The cross section evaluated for the 3.95 MeV state will be integrated over the missing energy and so will be differential in the proton and neutron solid angles where the neutron solid angle has been corrected for acceptance effects. Figures 4.19 and 4.20 show the neutron and proton energy distributions for a cut on the excitation energy spectrum from 1.0 to 7.0 MeV. These distributions represent the proton and neutron kinetic energies emitted when the ^{14}N residual nucleus is left in the 3.95 MeV state. Noting that neither the proton nor neutron distributions are affected by detector threshold effects, it is apparent that nearly all of the phase space for the solid angle coverage of the detectors has been measured. As a result, integration over the excitation energy should yield a cross section directly comparable to theoretical calculations within the statistical and systematics uncertainty of the measurement.

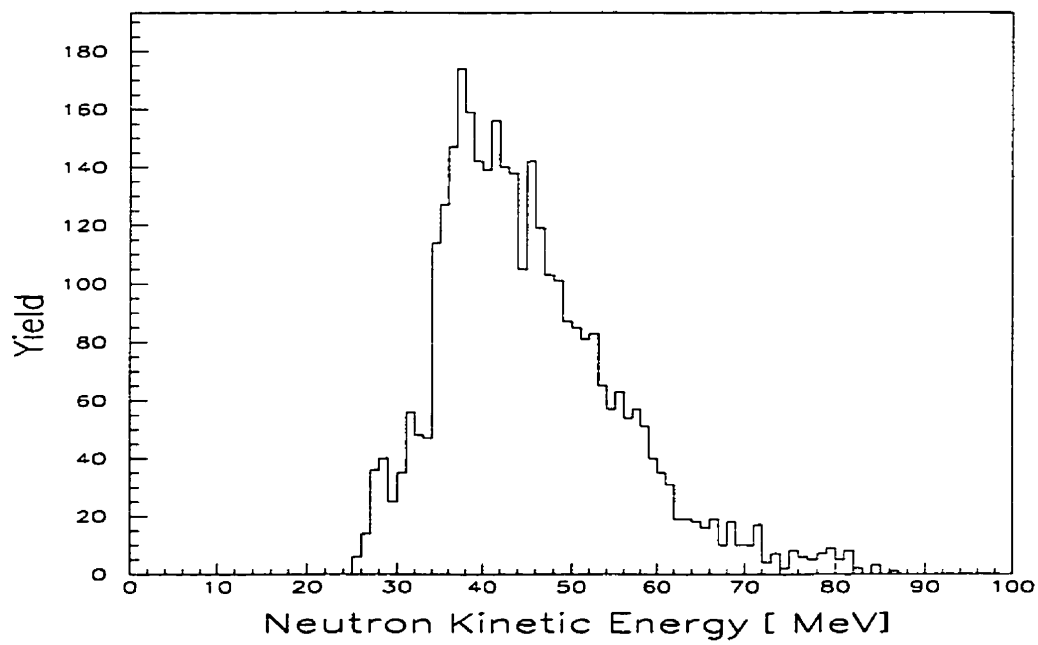

Figure 4.19: The neutron energy distribution comprising the 3.95 MeV state in ^{14}N.

The final correction to be made to the data in order to extract the absolute

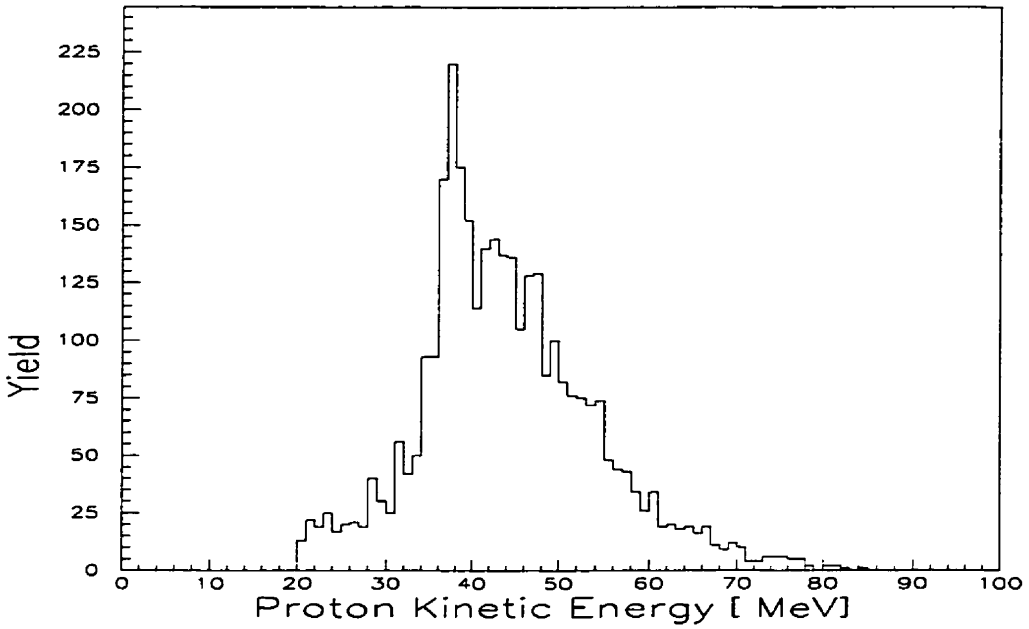

Figure 4.20: The proton energy distribution comprising the 3.95 MeV state in ^{14}N.

cross section is to account for the neutron detection efficiency for the prompt events comprising the 3.95 MeV state on an event-by-event basis. To accomplish this, the efficiency is obtained by the weighted average of the event-by-event neutron energies given in Figure 4.19. The weighted neutron efficiencies for the 3.95 MeV state were 14.4 % and 14.3 % for CsI detectors number one and two, respectively. The estimated systematic uncertainty in the neutron detection efficiency is 5%.

4.12 Estimation of systematic uncertainty

Table 4.3 lists the systematic errors for the single-arm and double-arm results of this measurement. The quadratic sums of the errors are 7.6% and 10.6% for the single-arm and double-arm results, respectively.

Table 4.3: Estimation of the systematic error of the measured cross sections

Parameter	Single arm	Double arm
Tagging efficiency	2%	2%
Number of target nuclei	7%	7%
Proton solid angle	2%	2%
Photon energy	1%	1%
Neutron solid angle	—	5%
Neutron detection efficiency	—	5%
Single arm error	7.6 %	—
Double arm error	—	10.6%

Chapter 5

Presentation and discussion of the experimental results

5.1 The $^{16}O(\gamma, p)^{15}N_{g.s.}$

5.1.1 Introduction

In a recent review article [56], the success of models based on the independent particle motion (IPM) concept in nuclear fermion systems was studied with an emphasis on electron scattering $(e, e'p)$ data. Sick, Pandharipande and Huberts [56] also studied the effects of correlations in fermion systems. From the data, the authors conclude that in $(e, e'p)$ reactions (almost exclusively performed at quasi-elastic kinematics) the IPM model allows the understanding of many features of nuclei. By extracting the spectroscopic factor S_j (the probability of the quasiparticle being a real particle) information is gained concerning the shell occupation number, n_j, which for a shell model orbital of spin j would equal $2j+1$ if $S_j = 1$. After analysis of the data, the authors conclude that for 2/3 of the time the nucleons in the nucleus act as independent particles bound in the nuclear mean field. The remaining 1/3 of the time, the nucleons are in states above the Fermi level. This is due to correlations resulting from the repulsive core and tensor parts of the nucleon-nucleon interaction.

Experimentally, correlations are inferred from the comparison of the yield of low lying states of the residual nucleus to the independent particle shell model sum rule limit. For instance, in the case of a single nucleon knocked out via the $^{16}O(e, e'p)^{15}N$ reaction, the low lying states in ^{15}N should be dominated by states with spins and parity of $\frac{1}{2}^-$ and $\frac{3}{2}^-$. Nucleon-nucleon correlations are commonly inferred from a comparison of the yield of such low lying states with the sum rule limit. The observa-

tion of positive parity states in the $^{16}O(e,e'p)^{15}N$ reaction [57] has been interpreted as protons originally in 2s or 1d shell model configurations in the ^{16}O target nucleus. Other than the depletion of the shell model occupation number for low lying states in the residual nucleus, a measurement at higher excitation energy can be used to study correlations. This is because such correlations cause a spreading of the depleted shell model states to higher excitation energies, so that integration over the excitation energy for more deeply bound shell model states should show an enhancement in the yield over the sum rule limit.

The DKO formalism, based on the IPM model for the constituent nucleons, which is successful in explaining the $(e,e'p)$ data as resulting from the direct one body interaction current (when correlations, contained in the spectroscopic factor S_j and final state interactions are accounted for) may not be expected to be as successful for the photonuclear $(\gamma, p_{0,1,2..})$ reaction. The reason is twofold. The $(e,e'p)$ reactions, which were performed in quasielastic kinematics, probe much lower momentum components of the shell model wave functions than the $(\gamma, p_{0,1,2..})$ reaction does. Also, the polarization of the virtual photon in $(e,e'p)$ is predominantly longitudinal in nature for quasielastic kinematics, whereas for real photons the polarization is purely transverse. It is therefore quite reasonable that the DKO mechanism, which is a one body interaction, may not be the only mechanism occurring in $(\gamma, p_{0,1,2..})$ reaction. It is in fact commonly accepted that the DKO mechanism accounts for only a small portion of the $(\gamma, p_{0,1,2..})$ reaction where other mechanisms such as meson-exchange currents (MECs) and short-range correlations (SRCs) dominate the photoabsorption process. The goal of the present analysis is to determine the extent to which the DKO mechanism accounts for the $(\gamma, p_{0,1,2..})$ reaction and to make an estimation of the contribution from effects such as MECs and SRCs.

5.1.2 DKO Calculations

The measured $^{16}O(\gamma,p)^{15}N_{g.s.}$ results will be compared with the DKO calculation described in Appendix A. This is a PWIA calculation using harmonic oscillator wave functions, where the oscillator parameter b=1.66 fm was used [11]. This value was found to reproduce the root-mean-square charge radius for ^{16}O derived from elastic electron scattering data using a harmonic oscillator model.

The measured results will also be compared with a DKO calculation based on the work of Boffi *et al.* [36, 2]. In these calculations, a spectral function is used to describe the overlap of the single-particle wave functions for the target and residual nuclei and a distorted wave is used to simulate FSI of the ejected nucleon. Generally, as in the case of the present calculation, the radial part of the shell model bound state wave function is calculated by solving the Schroedinger equation using a Woods-Saxon potential, including a spin-orbit and Coulomb potential, by an iterative process of matching the asymptotic (outside the potential well) part of the wave function, known analytically, with the interior wave function, derived from the potential, at the nuclear surface. Here, trial values for the binding energy are iteratively chosen until the wave function is matched at the nuclear surface. In this way, all information about the discrete energy levels of the target and the A-1 nucleus in question are contained in the wave functions. Inclusion of FSIs was accomplished via a distorted wave function for the ejected nucleon. The wave function is generated in an optical model potential with a Woods-Saxon radial distribution and with an imaginary part added to the potential to describe the removal of the nucleon from the initial reaction channel. Note that the bound state wave functions and the continuum wave function of the ejected proton are not generated in exactly the same potential, so the requirement of orthogonality between the initial and final states must be taken into consideration.

The particular code used was that of Ireland called GAMP4 [58]. A spectroscopic

factor $S_j = .57$ [59] was used to describe the depletion of the $p_{1/2}$ shell from the shell model prediction of $2j + 1$ nucleons. The inclusion of energy dependent terms in the optical potential, used to describe FSIs, necessitates that the cross section calculation must be performed in an unfactorised scheme in order to uphold orthogonality between the initial and final states. The calculation uses relativistic kinematics and takes into account center-of-mass motion, orthogonality and antisymmetry corrections. The optical model parameters were taken from Comfort and Karp [14] for a 40 MeV proton. All radii parameters were scaled by $A^{1/3}$ so as to emulate those expected for ^{15}N. A more detailed description of the calculation is given in reference [58].

Figure 5.1 shows the results of the current experimental measurement compared with other available data. Unfortunately only two closely spaced data points were obtained in this measurement, but the agreement with the previously measured results is quite good, indicating the presence of no large systematic errors. The solid curve represents the result of the PWIA calculation, as derived in Appendix A, using harmonic oscillator wave functions. The cross section predicted by the harmonic oscillator PWIA calculation performed at 64 MeV is seen to lie about a factor of two higher than the data. As discussed in Chapter two, and demonstrated in Figure 2.3, this result is consistent with the spurious contributions resulting from orthogonality and antisymmetry violation, as well as to the neglect of the center-of-mass motion. The dashed curve gives the results of the PWIA calculation for the bound state wave functions generated in a Woods-Saxon potential. This PWIA calculation has removed the spurious contributions to the cross section resulting from orthogonality and antisymmetry violation, as well as contributions due to the center-of-mass motion. For the low momentum components of the wave function (low angular range), the cross section is reduced by a factor of two from the results of the PWIA calculation (using

harmonic oscillator wave functions) as expected when the spurious contributions mentioned above are removed. At larger angles, the cross section becomes much larger than that predicted by the PWIA cross section using harmonic oscillator wave functions. This clearly demonstrates that the harmonic oscillator wave functions severely lack the high momentum components necessary to explain the data for high missing momentum or equivalently large bound state nucleon momentum. The dotted curve represents the results of the DWIA calculation [2] using the optical model parameters of Reference [14]. The predicted cross section lies about a factor of three below the measured data. This is taken as evidence that the one body current DKO reaction is not the only reaction mechanism involved in the absorption of high energy photons.

As described in Reference [38] an estimation of the contribution from two-body MECs to the absorption process can be made by taking the ratio of the PWIA calculation (dashed line) to the recalculated PWIA cross section with the inclusion of the contribution due to MECs by making use of Siegert's theorem (PWS). The ratio of PWS/PWIA then gives the approximate scaling to be applied to the DWIA calculation (dotted line) to obtain the resulting cross section for the DKO contribution added with the MEC contribution, and is shown as a dot-dashed line. The calculated cross section including MECs accounts for the magnitude of the measured cross section for the angles measured but is seen to overpredict the cross section at forward angles. It does therefore appear that the inclusion of MEC in this phenomenological way gives a better quantitative description of the measured cross sections than the predictions using only the DKO calculation. It is therefore observed that inclusion of MECs is necessary in explaining the $(\gamma, p_{0,1,2})$ reaction. However, before a contribution of SRCs to the $(\gamma, p_{0,1,2})$ reaction can be attempted, a microscopic calculation is required that includes MECs. Any disagreement with the measured cross sections may then be attributed to the effect of SRCs.

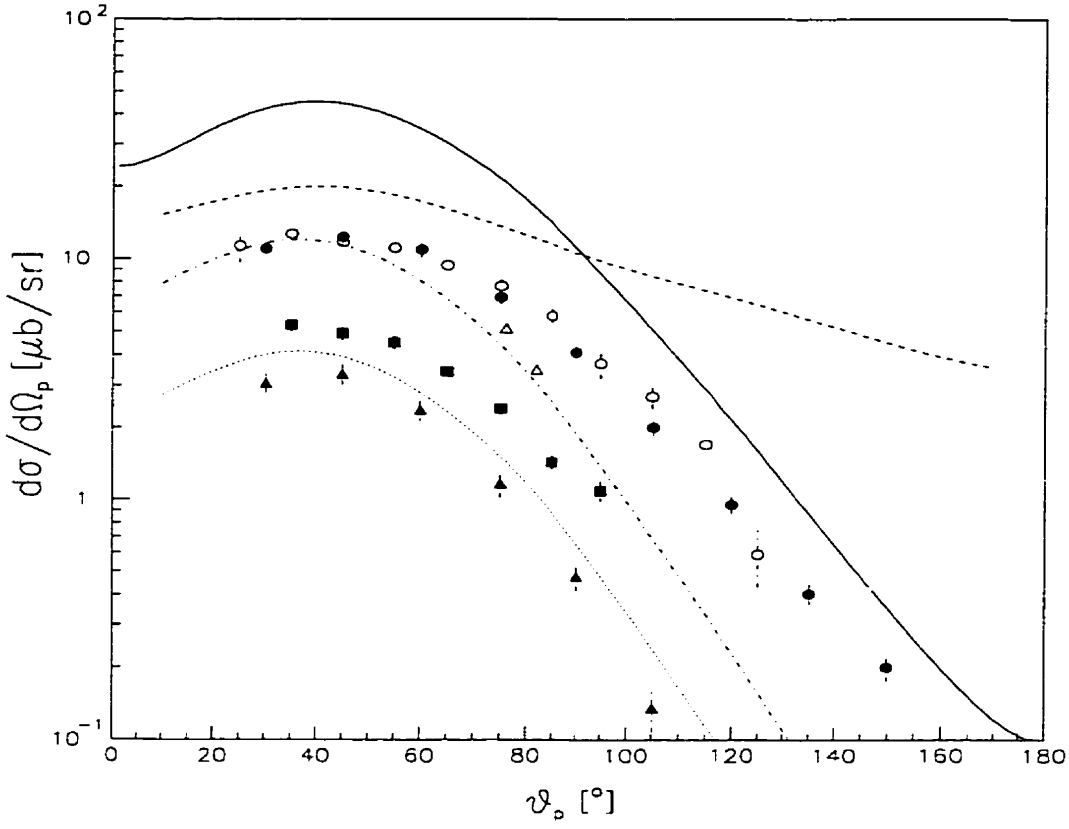

Figure 5.1: The results of the current $^{16}O(\gamma,p)^{15}N_{g.s.}$ measurement at 64 MeV (open triangles) are shown in comparison with the Findlay and Owens data [12] at 60 MeV (filled-in circles) and at 80 MeV (filled-in triangles). Also shown are the Lund data [13] measured at 70 MeV (filled-in boxes) and 60 MeV (open circles). The solid line represents the results of the PWIA calculation of Appendix A using harmonic oscillator wave functions, with harmonic oscillator parameter b = 1.66 fm, for E_γ = 64 MeV. The dashed curve presents the results of the PWIA calculation [2] using bound state wave functions generated in a Woods-Saxon potential for E_γ = 64 MeV. The dotted line is the DWIA calculation [2] using the optical model parameters of Comfort and Karp [14] for E_γ = 64 MeV. The dot-dash line represents an estimate of the two-body MEC contribution to the reaction for E_γ = 64 MeV. All error bars are statistical only.

5.2 The $^{16}O(\gamma, pn)^{14}N_{0,1,2,..}$ reaction

5.2.1 Introduction

The main purpose of this measurement was to investigate the principle quantum numbers involved in the photonuclear two-nucleon absorption process for the photon energy range from 100 to 140 MeV. It will be demonstrated, from two previous measurements in conjunction with the present measurement, that the measured yield to a discrete excitation energy state depends on the relative angular momentum transfer to the state and the phase space acceptance of the detection system. The angular momentum transfer influences the angular correlation of the emitted particles. This makes the sensitivity of the two-nucleon measurement to the L transfer, or equivalently the angular correlation, dependent on the phase space coverage of the reaction. Absorption on a quasideuteron with an L=0 transfer corresponds to an angular correlation of the pair peaked at the quasifree angle and the quasifree energy within the impulse approximation.

In the excitation energy spectrum for the $^{16}O(\gamma, pn)^{14}N_{0,1,2,..}$ reaction only one discrete state at low excitation energy was observed. In order to verify the energy calibrations and identify the state unambiguously, a check of the excitation energy difference between the deuterium peak and the low lying peak can be performed. Figure 5.2 shows the relative positioning of the two peaks. The reaction Q value for deuterium is 2.225 MeV, while that for the $^{16}O(\gamma, pn)^{14}N_{g.s.}$ is 22.96 MeV. The deuterium peak is observed to lie at -20.8 MeV in agreement with the difference in the two reaction Q values. The relative difference then unambiguously identifies the low lying peak as the 3.95 MeV state as is indicated by the excitation energy. Note that the neutron detection efficiency has not been included in this spectrum.

The primary purpose of this measurement was to verify which quantum numbers

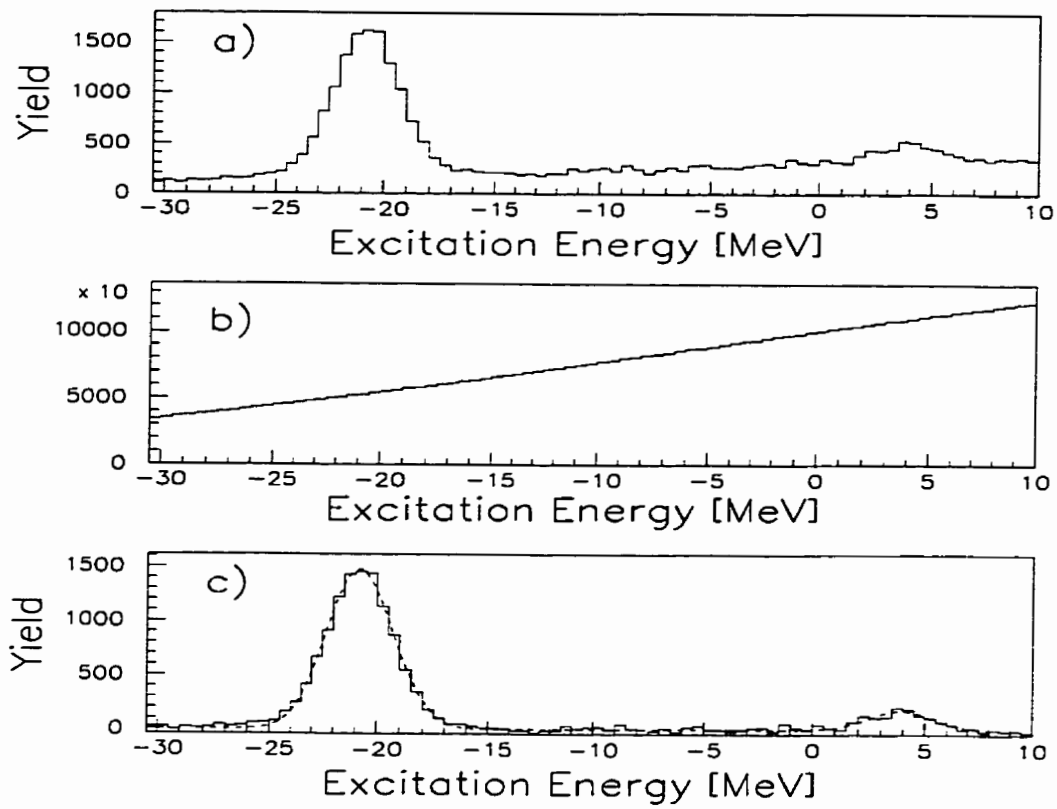

Figure 5.2: Excitation energy spectra for a) a cut on the prompt peak in the tagger TDC spectrum, b) a cut on the random region in the tagger TDC spectrum, c) the net excitation energy spectrum with the tagger random background subtracted. The kinematics used to construct the spectra was that for the $^{16}O(\gamma, pn)^{14}N_{g.s.}$ reaction. The dominant peak at -20.8 MeV is that resulting from the $^{2}H(\gamma, pn)$ reaction, while the smaller peak occurs at an excitation energy of 3.9 MeV and results from the $^{16}O(\gamma, pn)^{14}N_{2}$ reaction. The reaction Q value for deuterium is 2.225 MeV while that of $^{16}O(\gamma, pn)^{14}N_{g.s.}$ is 22.96 MeV. The excitation spectrum illustrates that the relative difference in the peak positions identifies the smaller peak as the 3.95 MeV 1^{+} state in ^{14}N.

are dominant in the two-nucleon absorption mechanism at the quasifree opening angle. The phase space acceptance of the reaction is set by the relative angular acceptance of the proton and neutron detectors. The proton detectors had an angular acceptance of $\Delta\theta_p = \pm 7°$. The neutron array had an angular acceptance of $\Delta\theta_n = \pm 6°$. The smaller angular acceptance of the neutron array dictates that the phase space acceptance for the coincident detection of a proton and a neutron is set by the neutron array's acceptance. The neutron detector is located at the opening angle expected for deuterium kinematics, matched to the center of the photon energy range used for this measurement. This is a good approximation to the opening angle for the quasifree process. The extended target also influences the phase space acceptance for the reaction. The question of the relevant quantum numbers for the absorption process is answered by noting the relative population of the low lying discrete states in ^{14}N and by a qualitative analysis of the continuum. Figure 5.3 depicts the excitation energy spectrum for the $^{16}O(\gamma, pn)^{14}N_{0,1,2,..}$ with a 20 MeV threshold for the proton detector and a 25 MeV cut for the neutron energy. The energy resolution of the 3.95 MeV $(1^+, 0)$ state is 3 MeV FWHM. This resolution is clearly sufficient to conclude that there is no significant yield to the ground state $(1^+, 0)$, 2.31 $(0^+, 1)$, 7.03 $(2^+, 0)$ and the 11.03 $(3^+, 0)$ MeV states. One of the more controversial topics is whether absorption on a proton-neutron pair in a T=1 state provides a significant contribution to the reaction mechanism. The relative yield to the 2.31 MeV $(0^+, 1)$ state is estimated from this measurement to be less than 5% of that of the 3.95 MeV $(1^+, 0)$ state, and is therefore not expected to be important in the two-nucleon absorption mechanism.

Before continuing further with the analysis of the quantum numbers involved in the two-nucleon absorption mechanism, it is instructive to compare the present measurement with the other existing high resolution two-nucleon absorption measurements. For comparison with Figure 5.3, there exist only two previous high resolution mea-

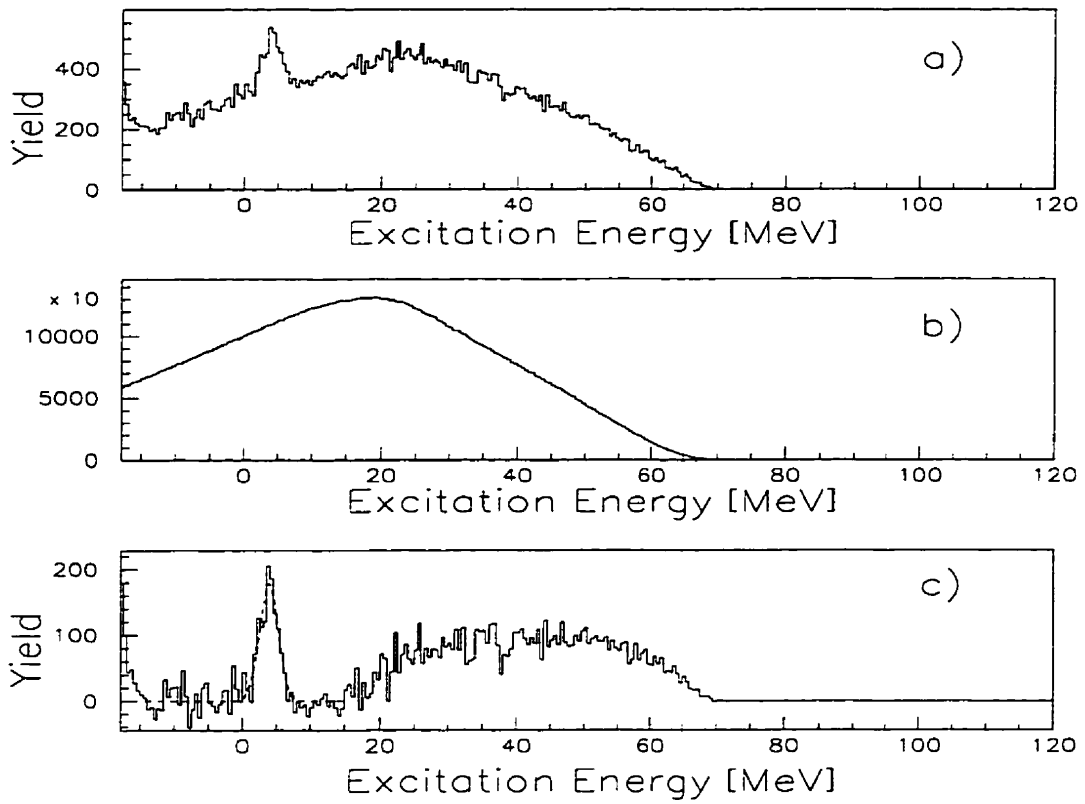

Figure 5.3: The a) prompt, b) random and c) random subtracted yield for the excitation range from -17.0 MeV to 120 MeV. The discrete state at 3.9 MeV is identified with the 3.95 MeV $(1^+, 0)$ level in ^{14}N. The yield in the peak is 1247 counts. Significant yield in the continuum begins at approximately 18 to 20 MeV and is thought to consist of removal of a p shell and of an s shell coupled nucleon pair in the (γ, pn) reaction. Accounting for the net excitation energy resolution, the results seem to indicate a clean measurement of the minimal shell removal energy for a coupled p and s shell nucleon pair. The minimal shell removal energy is estimated to be 19 $\pm$ 1 MeV.

surements which investigated the two-nucleon absorption mechanism with adequate resolution to separate the residual excited states in the residual ^{14}N nucleus.

One measurement [11] was the $^{16}O(\pi^+, pp)^{14}N_{0,1,2,..}$ reaction for T_π = 116 MeV. This measurement made a distinction between the exact quasifree kinematical angle and the phase space surrounding the quasifree opening angle between the simultaneously ejected neutron and proton. Figure 5.4 depicts the results of a two-nucleon pion absorption measurement for a) the quasifree angle of the pair and b) 20° off the quasifree angle. Figure 5.4 a) presents the relative yields of the residual excited states populated for the two-nucleon absorption mechanism at the quasifree angle of the pair. The 3.95 MeV 1^+ state dominates the excitation spectrum while the 1^+ ground state, 2^+ 7.03 and 3^+ 11.05 MeV states are each approximately 10%-12% of the yield to the 3.95 MeV state. If the $^{16}O(\gamma, pn)^{14}N_{0,1,2,..}$ is assumed to have the same relative yields as the pion absorption measurement, then one would expect about 150 counts in each of the three unobserved T=0 peaks. That is, for significant population of the ground state and the 7.03 MeV state there would be obvious yield visible in Figure 5.3 near the ground state and the 7.03 MeV state. However, no statistically significant yield was observed. The relative acceptances for the detection systems are similar in both the pion absorption measurement and in this photonuclear absorption measurement. Since both measurements are performed at the quasifree angle of the pair, there appears to be a difference between the reaction mechanism for two-nucleon absorption between the two reactions.

Figure 5.4 b) presents the results of the $^{16}O(\pi^+, pp)^{14}N_{0,1,2,..}$ measurement performed 20° greater than the quasifree angle. The detection angles are as indicated in the figure. The results of 5.4 a) and b) have been relatively normalised. The yields of the ground state, 7.03 and 11.05 MeV states are seen to be of comparable magnitude to that seen in the on-quasifree angle measurement. However, the yield of the

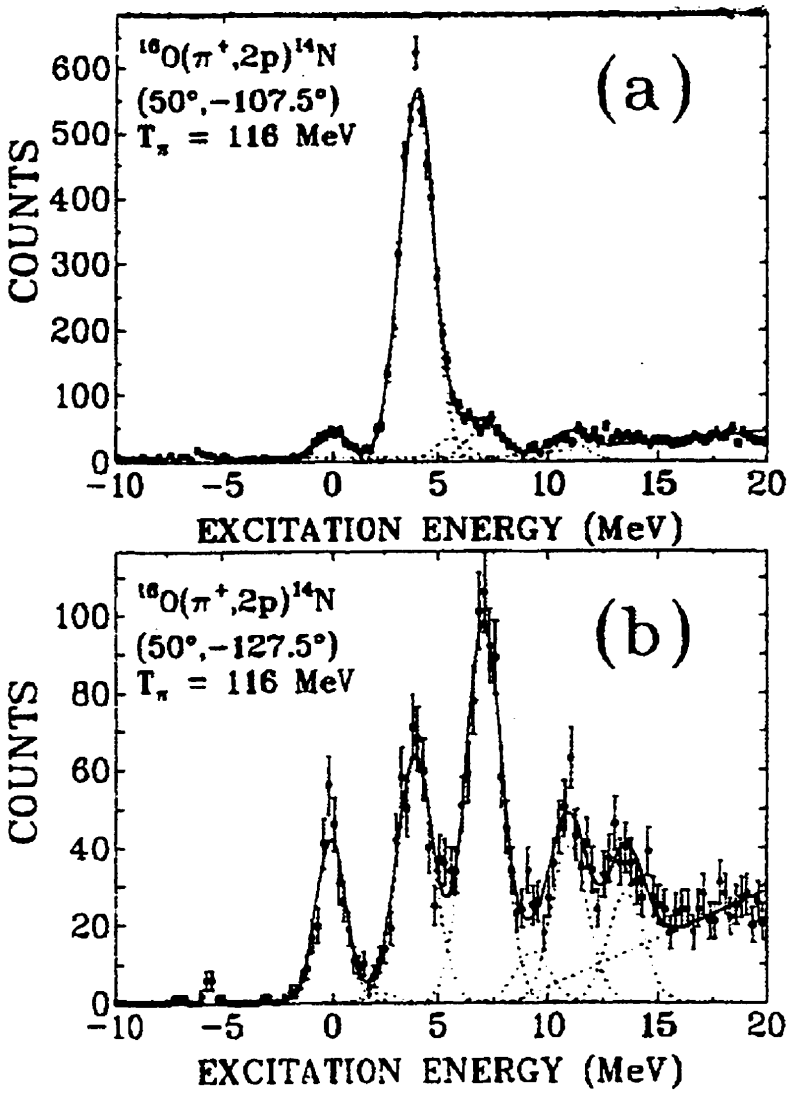

Figure 5.4: Excitation spectra for a) the quasifree angle pair and b) 20° greater than the quasifree angle. At the quasifree angle the L=0, 3.95 MeV state dominates the excitation spectrum, while at the setting away from the quasifree angle the L=2, 0.0, 7.03 and 11.05 MeV states are more prominent. The figure is taken from Reference [11].

3.95 MeV state is seen to decrease by about an order of magnitude. It is interesting to note that Reference [11] also measured the reaction at $\theta_{p1} = 50°$ and $\theta_{p2} = -87.5°$ (20 degrees less than the quasifree angle of the pair) and the results indicate that the 3.95 MeV state still dominates the reaction, being about a factor of 3 larger than the other 3 observed states.

The fact that the 3.95 $(1^+, 0)$ state, but not the ground state is populated in Figure 5.3 can be understood in terms of the spectroscopic factors calculated by Cohen and Kurath [7]. From a shell model calculation, they note that the structure of the two states differs in the preferred orbital angular momentum transfer in the reaction. The ^{14}N ground state is predominantly reached by an L=2 transfer with respect to the center of mass of the ^{14}N spectator nucleus, while the 3.95 MeV state is dominated by an L=0 transfer. The 7.03 and 11.05 MeV states, also not observed, are reached by pure L=2 transfer. Therefore, it seems apparent that for the photon energy range from 100 to 140 MeV at the quasifree opening angle, the photon interacts with the two nucleon system via a L=0 transfer with the L=2 transfer being strongly suppressed. Although a L=1 transfer is possible for this state, it is likely not significant, as experimental evidence supports the 3.95 MeV state as being populated by a predominant L=0 transfer [11, 10, 42].

The results of the pion absorption angular correlation measurement $^{16}O(\pi^+, pp)^{14}N_{0,1,2..}$ [11] presented in Figure 2.9 indicate a significant L=0 transfer to the ground state, 33 times the value predicted by Cohen and Kurath. The ground state is commonly interpreted to be reached by a dominant L=2 transfer. Furthermore, the $^{16}O(p,t)^{14}N$ [60] transfer reaction reported that the L=2 transfer is twice as large as the L=0 transfer to the residual 3.95 MeV state, so that there appear to be discrepancies between the angular momentum character for the residual states in ^{14}N between the various measurements.

It is possible from the results of this measurement to comment on the above experimentally inferred L transfers for the two states. In the previous pion absorption measurement [11], Schumacher *et al.* claim that the ground state has a significant L=0 transfer component, in contrast to the predictions of Cohen and Kurath. However, including a J dependence in the two-nucleon pion absorption formalism [6], the angular correlation distributions for the ^{14}N ground state, when reanalysed, were seen to require less L=0 transfer strength in the wave functions to reproduce the data. In the excitation spectrum Figure 5.2, it is observed that only the 3.95 MeV state is strongly populated and that the ground state is not significantly populated. Since the L=2, 7.03 MeV and 11.05 MeV states, and the predominantly L=2 ground state are not populated it seems very unlikely that much L=2 character can be ascribed to the 3.95 MeV state in contrast to the analysis of Reference [60]. If similar relative yields between the excited states for the pion absorption measurement [11] (see Figure 5.4 a) and the current $^{16}O(\gamma,pn)^{14}N_{0,1,2..}$ measurement are expected, and the L=0 contribution to the ground state is that determined from Reference [11], then one would expect to see a yield of only 30 to 40 counts. As is evident in Figure 5.3 such a yield would likely not be detected above background. The fact that only the 3.95 MeV $(1^+,0)$ state is populated is seen as model independent support that the 3.95 MeV state is predominantly L=0 transfer in nature, while the ground state, 7.03 and 11.05 MeV states are predominately L=2 transfer. This qualitatively supports the predictions of Cohen and Kurath. If it is desired to use this experimental setup to check the results of the pion absorption measurement with respect to the L=0 transfer to the ground state, then approximately 5 to 10 times more run time would be required. The experimental cross sections for the $^{16}O(\gamma,pn)^{14}N_{0,1,2..}$ measurement are presented in Table 5.1.

Another major difference in the excitation energy spectra for the pion and pho-

Table 5.1: The cross sections for the $^{16}O(\gamma, pn)^{14}N_{0,1,2..}$ reaction resulting from the current measurement are listed. The photon energy range was from 100 to 140 MeV. The data were taken at the expected quasifree opening angle of the nucleon pair. An upper estimate of the cross section for the ground state, 2.31, 7.03 and the 11.05 MeV states is given. The yields listed for the energy range 0-20, 20-45 and 45-75 are meant to represent the approximate contributions to the cross section from 2 p-shell nucleons, 1 p-shell and 1 s-shell nucleons, and 2 s-shell nucleons respectively. The * in the table is used to signify that the cross section to these states is $< 5\%$ of the value for the 3.95 MeV state. The errors stated with the measured cross sections are statistical only.

State (MeV)	$d^2\sigma/d\Omega_p d\Omega_n$ (μb/sr^2)	θ_p (°)
Ground State	*	82
2.31	*	82
3.95	26.5 $\pm$2.2	82
7.03	*	82
11.05	*	82
Excitation Energy (MeV)	Yield	θ_p (°)
0-20	682	82
20-45	2329	82
45-70	1601	82
Ground State	*	76
2.31	*	76
3.95	23.7 $\pm$ 2.2	76
7.03	*	76
11.05	*	76
Excitation Energy (MeV)	Yield	θ_p (°)
0-20	563	76
20-45	2143	76
45-70	1648	76

ton absorption reactions is that in the case of the pion absorption measurement the continuum yield is greatly suppressed compared to the removal of two p-shell nucleons. The two p-shell region is commonly taken to be from 0 to 20 MeV of excitation energy. For the photoabsorption mechanism, the continuum yield above 20 MeV is much larger than the yield of the two p-shell contribution. This difference can be understood by noting that the pion interacts hadronicly and is usually referred to as a surface probe. That is, before the pion can reach the interior shells within the nucleus, its short mean-free path in nuclear matter preferentially causes it to interact with nucleons in the outer shells. For an incident pion kinetic energy of 116 MeV, the pion is approaching the energy needed to excite the delta-resonance and is therefore near the energy where its mean-free path in nuclear matter is smallest. In the case of photoabsorption, the photon interacts weakly so that it illuminates the entire nucleus uniformly, thereby enabling it to probe the more deeply bound states.

If it is assumed that the excitation energy range from 0 to 20 MeV comprises the two p-shell contribution to the cross section, the 20 to 45 MeV region comprises the one p-shell one s-shell contribution and the 45 to 70 MeV region comprises the two s-shell contribution, then integration of the regions should give the contribution arising from the coupling of the nucleons in the stated shell model orbits. The results of these integrated yields is given in Table 5.1. In the absence of FSIs the relative population of the $(1p)^{-2}$, $(1p)^{-1}(1s)^{-1}$ and the $(1s)^{-2}$ two-hole states in ^{14}N should be roughly similar to the number of initial proton-neutron pairs in these orbitals, being $\frac{9}{16}$, $\frac{6}{16}$ and $\frac{1}{16}$, respectively. This is clearly not evident in the current measurement. FSIs cannot account for all the shifting of the expected $(1p)^{-2}$ to higher excitation energies. This measurement supports a depletion of the $(1p)^{-2}$ contribution to the measured cross section, as is evidenced by the large continuum yield above 20 MeV, and seems to indicate the presence of correlations in the ground state of ^{16}O. This

result will be discussed further in Section 5.2.2.

A recent measurement [15] of the $^{16}O(\gamma,pn)^{14}N_{0,1,2,..}$ reaction for the photon energy range 67 to 76 MeV does show that the photon absorption process is sensitive to angular momentum transfer L=2. The proton angular range was 60° to 100° while the neutrons were detected in the angular range from 81° to 103° on the opposite side of the photon beam. From Figure 5.5, it is observed that the ground state, 3.95 MeV and 7.03 MeV states are seen to be approximately equally populated. This result is likely due to the large phase space acceptance, so that most events recorded were off the quasifree angle of the absorbing pair. This is consistent with the pion absorption measurement [11]. Interestingly the 11.0 MeV state is not seen in this photoabsorption measurement. This likely results from a combination of the low photon energy and the detector thresholds.

The cross sections derived from this measurement [15] are given in Table 5.2 along with the predictions of the microscopic calculation of Ryckebusch *et al.* [5]. Threshold and acceptance effects were included via a Monte Carlo simulation where the input for the events where taken from the calculation. Unfortunately the calculation predicts neither the trend of the measured cross sections nor the magnitude. The source of the discrepancy between the calculation and measurement is unknown.

The question of the primary quantum numbers involved in the two-nucleon absorption mechanism will now be addressed. In Figure 5.3 only the 3.95 MeV 1^+ state was observed to have significant population. Cohen and Kurath predict this state to be a $(p_{1/2})^{-1}(p_{3/2})^{-1}$ shell model configuration. Furthermore, observation of the continuum yield demonstrates that absorption on proton-neutron pairs in $(p)^{-1}(s)^{-1}$ and $(s)^{-2}$ shell model configurations is also important at the quasifree opening angle of the pair. The quantum numbers for the various observed (or inferred in the case of the continuum yield) shell model states are given in Table 5.3. No significant con-

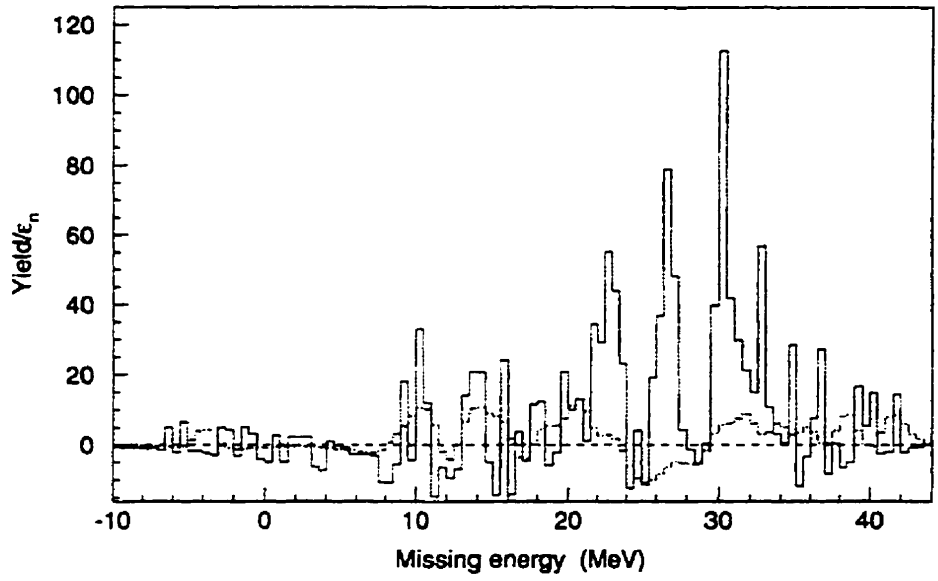

Figure 5.5: Missing energy spectrum for the $^{16}O(\gamma, pn)^{14}N_{0,1,2,..}$ reaction. The yield has been corrected for the neutron detection efficiency of approximately 13%. The solid histogram is the net yield after the tagger random and empty target subtractions. The dashed histogram is the empty target contribution. The ground state (at $E_{missing}$ = 23 MeV), 3.95 MeV (at $E_{missing}$ = 27 MeV) and 7.03 MeV (at $E_{missing}$ = 30 MeV) states are seen to be approximately equally populated. The figure is taken from Reference [15].

Table 5.2: The cross sections for the $^{16}O(\gamma,pn)^{14}N_{0,1,2..}$ reaction resulting from the recent Lund measurement [15] are listed. The photon energy range was from 67 to 76 MeV. The proton angular range was from 60 to 100 degrees and the neutron angular range was from 81 to 103 degrees. The errors are statistical only.

State (MeV)	$d^2\sigma/d\Omega_p d\Omega_n$—$_{calc}$ (μb/sr^2)	$d^2\sigma/d\Omega_p d\Omega_n$—$_{meas}$ (μb/sr^2)
Ground State	0.27	1.4 ± 0.5
2.31	0.05	—
3.95	1.00	1.7 ± 0.5
7.03	0.20	1.6 ± 0.4

tribution to the two-nucleon absorption cross section corresponding to L=2 angular momentum transfer was observed in the first 20 MeV of excitation energy. Therefore, it can be assumed that for all possible shell model configurations this quantum number is insignificant at the quasifree opening angle of the pair. Furthermore, contributions to the cross section for angular momentum transfers larger than L=2 are also assumed insignificant, as the relative yield to the cross section decreases significantly as L increases. This restriction on the angular momentum transfer L also restricts the possible values of the relative angular momentum l entering into the absorption process.

5.2.2 Correlations in the ^{16}O ground state wave function

Calculations using models based on the independent-particle motion (IPM) for the bound nucleons, such as a mean field or Hartree-Folk predict that for infinite nuclear matter the momentum distribution is identical to the momentum distribution of a free Fermi gas. This implies that all states with a momentum less than the Fermi momentum, k_F are occupied with a probability $n = 1$ while all states with momentum greater than k_F are completely unoccupied ($n = 0$). Correlations due to the tensor

Table 5.3: Principle quantum numbers involved in the two-nucleon absorption mechanism at the quasifree opening angle of the pair inferred from the current $^{16}O(\gamma, pn)^{14}N_{0,1,2,..}$ measurement.

E_x(MeV)	J^π	Configuration	T	l	S	L
3.95	1^+	$(p_{\frac{1}{2}})^{-1}(p_{\frac{3}{2}})^{-1}$	0	0	1	0
3.95	1^+	$(p_{\frac{1}{2}})^{-1}(p_{\frac{3}{2}})^{-1}$	0	1	0	1
3.95	1^+	$(p_{\frac{1}{2}})^{-1}(p_{\frac{3}{2}})^{-1}$	0	2	1	0
20-45	1^-	$(p_{\frac{3}{2}})^{-1}(s_{\frac{1}{2}})^{-1}$	0	0	1	1
20-45	1^-	$(p_{\frac{3}{2}})^{-1}(s_{\frac{1}{2}})^{-1}$	0	2	1	1
20-45	2^-	$(p_{\frac{3}{2}})^{-1}(s_{\frac{1}{2}})^{-1}$	0	0	1	1
20-45	2^-	$(p_{\frac{3}{2}})^{-1}(s_{\frac{1}{2}})^{-1}$	0	2	1	1
20-45	0^-	$(p_{\frac{1}{2}})^{-1}(s_{\frac{1}{2}})^{-1}$	0	0	1	1
20-45	1^-	$(p_{\frac{1}{2}})^{-1}(s_{\frac{1}{2}})^{-1}$	0	0	1	1
20-45	1^-	$(p_{\frac{1}{2}})^{-1}(s_{\frac{1}{2}})^{-1}$	0	2	1	1
45-70	0^+	$(s_{\frac{1}{2}})^{-2}$	0	1	0	1
45-70	1^+	$(s_{\frac{1}{2}})^{-2}$	0	0	1	0
45-70	1^+	$(s_{\frac{1}{2}})^{-2}$	0	1	0	1
45-70	1^+	$(s_{\frac{1}{2}})^{-2}$	0	2	1	0

force in the nucleon-nucleon interaction (usually referred to as long range correlations) and the more violent hard core repulsion of the nucleon-nucleon interaction (referred to as short range correlations, SRCs) cause a depletion of momentum states below k_F and an enhancement of states above k_F. Experiments such as the $^{16}O(e, e'p)^{15}N_{0,1,2,..}$ measurement [57] determine a depletion of approximately 40% for the $1p_{1/2}$ ground state and about 33% for the 6.32 MeV $p_{3/2}$ valence orbitals.

Recent theoretical studies [61, 62, 63] to determine the momentum distribution in a microscopic calculation have been performed for finite nuclei such as ^{16}O. The spectral function tells us at which excitation energies of the residual nucleus different components of the momentum distribution should be observed. The depleted valence shells, which result from the long range correlations induced by the tensor force, are

predicted to occur at low values of excitation energy of the residual nucleus. The higher momentum components, associated with short range correlations, result from the hard core repulsion of the nucleon-nucleon interaction and are expected to result in larger excitation energies of the residual nucleus. In the recent $^{16}O(e,e'p)^{15}N_{0,1,2,..}$ measurement [57], positive parity states in the recoil nucleus were observed for excitation energies up to about 20 MeV. In the absence of two-step processes, the IPM can achieve such states by protons knocked out of the $1s$ or $2s1d$ orbitals. Multipole decomposition of the momentum distribution for the positive parity 5.27 MeV ($5/2^+$) and 5.30 MeV ($1/2^+$) states, determined that the protons were knocked out of the $2s_{1/2}$ and $1d_{5/2}$ orbitals. Due to the low excitation energies of these states, the correlations are thought to be long range in nature and to result from the tensor force in the nucleon-nucleon interaction. In the present measurement, excess yield at large excitation energies could indicate the presence of SRCs in the photoabsorption process when studied using a shell model interpretation. The photon has long been thought to be an ideal probe to study SRCs, due to the large momentum mismatch of the photon. The current measurement can be expected to be more sensitive to the higher momentum components resulting from SRCs than the $(e,e'p)$ measurements.

In order to extract the spectroscopic factor S_j from the analysis of the discrete state and continuum parts of the excitation energy spectrum, a good understanding of the single particle energies and widths of the deep hole states is required for a shell model or IPM interpretation of the data. Also it is important to understand the treatment of FSIs, and where the loss in yield for the various shells will occur in the measured phase space of the reaction. Since no such microscopic calculation exists, only an estimate of S_j for the 1 p-shell nucleons will be made using a phenomenological approach. Some assumptions simplify this qualitative discussion. It is assumed that the FSIs are independent of the nucleon kinetic energy for the range of energies

encountered in this experiment. The actual nucleon attenuation factor increases by about 20% [64], as the nucleon energy decreases, for nucleon kinetic energies ranging from 25 MeV to 70 MeV. This effect would predict a greater loss due to FSIs for the ejected nucleons which result in $(1p)^{-1}(1s)^{-1}$ two-hole excitations compared to those leaving a $(1p)^{-2}$ configuration. It is also assumed that contributions to the continuum resulting from nucleons initially bound in a $(1p)^{-2}$ configuration undergoing a FSI will not contribute much to the $(1p)^{-1}(1s)^{-1}$ excitation phase space which is assumed to correspond to the excitation energy range from 20 to 45 MeV. This should be a reasonable assumption, since events in which one or both of the nucleons have undergone a FSI should predominantly lie at high excitation energies. The neutron detection efficiency is assumed to be constant as a function of the neutron energy. If this were properly corrected for, it would increase the yield of the $(1p)^{-2}$ compared to that resulting from the $(1p)^{-1}(1s)^{-1}$ by about 10%. Corrections due to the phase space acceptance of the detectors, resulting from the angular correlation differences for nucleons ejected from the different shell couplings, are also ignored. This correction, if performed, would increase the $(1p)^{-1}(1s)^{-1}$ contribution compared to that resulting from the $(1p)^{-1}(1s)^{-1}$. From the current measurement it was inferred that events resulting from proton-neutron pairs in a $(1p)^{-1}(1s)^{-1}$ configuration are reached solely by an $L = 1$ angular momentum transfer. This in turn predicts a broader angular correlation compared to events resulting from a $(1p)^{-2}$ configuration which results from an $L = 0$ transfer.

Noting that the 1 s-shell and 1 p-shell wave functions largely overlap enables one to infer that the relative strengths of the residual excitations should be in the approximate ratio, 9/16 : 6/16 : and 1/16 corresponding to the $(1p)^{-2}$: $(1p)^{-1}(1s)^{-1}$: and $(1s)^{-2}$ two-hole states in the residual ^{14}N nucleus. Therefore, in a simple IPM formalism, the ratio of the yield from $(1p)^{-2}$ configuration to that from the $(1p)^{-1}(1s)^{-1}$

configuration should be 1.5 in the absence of correlations, implying $S_j = 1$. If the approximations discussed in the preceding paragraph are assumed to be small, then the ratio of the experimental yields for the excitation energy range from 0 to 20 MeV (Y_{pp}) to that for the 20 to 45 MeV (Y_{ps}) should be 1.5. From Table 5.1 it is clear that the ratio (Y_{pp}) to (Y_{ps}) is much less than 1.5. If the depleted yield which results primarily from the 3.95 MeV state (no other states were significantly populated), is assumed to be predominantly spread over the excitation energy range from 20 to 45 MeV, a method for determining S_j is suggested. By an iterative process of choosing S_j^2 (two p-shell nucleons are involved in the absorption process) and correcting the $(p)^{-2}$ yield given in Table 5.1 by dividing by the factor S_j^2, the yield for this nucleon configuration in the absence of SRCs may be obtained. Next, this contribution due to correlations contained in the choice of S_j^2 needs to be removed from the $(p)^{-1}(s)^{-1}$ yield given in Table 5.1. The result is that in order to obtain the expected IPM yield of $Y_{pp}/Y_{sp} = 1.5$ a value of $S_j = 0.62$ is required.

Chapter 6

Concluding remarks on photonuclear reaction mechanisms at intermediate energies

6.1 Conclusions reached for the $^{16}O(\gamma,p)^{15}N_{g.s.}$ reaction

The purpose of the present measurement was to study the reaction mechanisms for intermediate energy photons interacting with ^{16}O. For the photon energy of 64 MeV, the $^{16}O(\gamma,p)^{15}N_{g.s.}$ cross sections were measured for the proton detection angles of 76° and 82°. The measured cross sections were compared with PWIA and DWIA calculations. The failure of the DWIA calculation to explain the magnitude of the measured cross section (the results of the calculation are low by a factor of about 3 to 4) is taken as evidence that photoabsorption mechanisms, other than the one body direct knockout mechanism, are involved in this reaction. Two-body MECs were added to the results of the DKO calculation in a phenomenological way by the inclusion of Siegert's theorem to the interaction Hamiltonian. Better quantitative agreement between the calculation and the measured cross sections was observed, indicating that the DKO contribution to the (γ,p) reaction is not the dominant mechanism at work, but that other two-body interactions play a larger role. More microscopic theoretical calculations including two-body currents are required. The inclusion of the dominant MEC interaction leads to a natural description of the near equality of the (γ,p) and (γ,n) cross sections in the photon energy range from about 40 MeV to 200 MeV.

6.2 Conclusions reached for the $^{16}O(\gamma, pn)^{14}N_{0,1,2,..}$ reaction

The main goal of this experiment was to determine the principle quantum numbers involved in the $^{16}O(\gamma, pn)^{14}N_{0,1,2,..}$ reaction at the quasifree opening angle of the outgoing neutron-proton pair for the photon energy range from 100 to 400 MeV. Only the 3.95 MeV (1^+,0) low lying state was observed to be populated. This result was interpreted as showing the dominance of L=0 angular momentum transfer for two-nucleon absorption at the quasifree opening angle of the pair. Since L=2 transfer is strongly suppressed in this reaction, and since the contribution to the calculated cross section decreases with increasing L transfer, only L=0 and L=1 transfer are expected to be important for this reaction. The relative angular momentum values l=0,1,2 are deemed to provide the most significant contribution to the cross section and follow directly from limiting the angular momentum transfer to be only L=0,1. The cross sections determined for the 3.95 MeV (1^+,0) state in ^{14}N for the photon energy range E_γ = 100 to 140 MeV are 26.5 $\pm$ 3.3 μb and 23.7 $\pm$ 2.2 μb for θ_p = 82° and 76°, respectively. No significant population of the 2.31 MeV (0^+,1) state was observed, so that absorption on a proton-neutron pair in an isospin triplet configuration (T=1) is strongly suppressed.

Interpretation of the $(1p)^{-1}(1s)^{-1}$ continuum yield compared to the $(1p)^{-2}$ 3.95 MeV yield is seen as strong evidence for the presence of SRCs due to the hard core repulsion of the nucleon-nucleon force. Analysis of the ratio of the yields of the different shell couplings was performed in an *ad hoc* fashion due to the lack of microscopic calculations available. From this analysis, the spectroscopic factor representing the depletion of 1 p-shell nucleons due to SRCs was determined to be S_j=0.62 in reasonable agreement with previous measurements. However, due to the numerous assumptions made in obtaining S_j and the obvious suppression of the $(1p)^{-2}$ yield compared to the $(1p)^{-1}(1s)^{-1}$ yield there is a need for more microscopic calculations to be performed

in order to make certain whether the present measurement is truly sensitive to SRC's.

On a technical note, the neutron detection efficiency for a 7.6 cm thick BC400 plastic scintillator was measured for the neutron energy range from about 30 MeV to 70 MeV. A 2 MeV_{ee} detection threshold was applied where it was assumed that the light output for BC400 was the same as that for NE102A. The results are found to be in good agreement with the NE102A and the 97% polystyrene plastic scintillator neutron detection efficiencies reported in Reference [51]. The results of the neutron detection efficiencies were also compared with GEANT Monte Carlo simulations using the FLUKA hadronic interaction code [52]. The results of the simulations using a 2 MeV_{ee} threshold on the energy deposited predicted neither the magnitude nor the trend in the measured efficiencies for the neutron kinetic energy range from 30 to 70 MeV. Therefore the FLUKA hadronic interaction code [52] is not accurate for the neutron kinetic energy range cited above.

6.3 Conclusions reached for the $^{12}C(\gamma, p)X$ reaction

The inclusive $^{12}C(\gamma, p)X$ measurement reported on in Appendix B complements the present exclusive $^{16}O(\gamma, pn)^{14}N_{0,1,2,..}$ reaction currently measured. The important results of the inclusive measurement will now be presented. For this reaction, inclusive proton energy spectra were obtained for the detection angles $\theta_p = 51°$, 81°, 109° and 141° for the photon energy range E_γ = 177 to 217 MeV. Although at the forward detection angles, quasifree pion production (QFPP) was evident in the structure of the proton spectra, the two-nucleon absorption mechanism was still the dominant photoabsorption process at these energies. Structure, characteristic of two-nucleon absorption kinematics, was observed in the proton energy spectra at backward detection angles, $\theta_p > 90°$, at the photon energy of 212 MeV. This is the first time that this important feature has been observed in a photoabsorption measurement.

The total two-nucleon absorption cross section predicted by Levinger's original QD [40] model, at the photon energy of $E_\gamma = 212$ MeV, was 825 μb when the Levinger constant L = 4.9 is used. This value comes from a recent calculation (Rereference 33 of Appendix B) rather than from a fit to the data. The result of Levinger's prediction is supported by the measured 925 μb total cross section. This lower limit of the total cross section was obtained by integration of the proton energy spectra back to the detector threshold after which a Legendre polynomial fit was used to extract the total absorption cross section for $E_\gamma = 212$ MeV. Most of this lower limit of the total cross section can be attributed to the two-nucleon photoabsorption process.

The total cross section predicted by Levinger's original formula is in reasonable agreement with the approximate 1.0 mb prediction of Laget [64] based on a meson-exchange QD model and with the 0.96 mb result of the microscopic calculation of Oset and Carrasco [65]. However, the RPA calculation of Ryckebusch *et al.* [66] predicts the total two-nucleon absorption cross section to be approximately 0.28 mb. This result is about a factor of 3 less than the other results given above.

The total cross section predicted by Levinger's QD model, and supported by this inclusive $^{12}C(\gamma,p)X$ measurement, is in good agreement with that of Laget and that of Oset and Carrasco. However, when the Gottfried factorized QD calculation [30] is used to predict the angular distribution of the photoprotons, it is found to give an unsatisfactory description of the measured two-nucleon absorption angular distribution. This failure to reproduce the angular distribution is related to the choice of using the off-shell $^2H(\gamma,p)n$ cross section. As was demonstrated in Figure 2.4, the on-shell deuterium cross section, when scaled to fit the height of the two-nucleon absorption peak at one angle, provides a good description of the two-nucleon absorption cross section at all detection angles. The choice of using on-shell cross sections to describe the two-nucleon absorption process is common practice in the pion absorption measurements

[11, 8] and is found to be in good agreement with the measured data. However, as mentioned above, the Gottfried factorized model using off-shell cross sections is not able to reproduce the measured angular distribution. This is seen as evidence that the use of the off-shell cross sections, driven by the momentum dependence of the absorbing proton-neutron pair contained in the form factor $F(P_{qd})$, does not seem justified. Gottfried had originally questioned the validity of using the off-shell cross section, especially for values far off the energy shell. The results of this measurement do seem to support Gottfried's original concern with the choice of using off-shell cross sections to describe the two-nucleon photoabsorption process.

References

[1] J. Ahrens, Nucl. Phys. **A446**, 229c (1985).

[2] S. Boffi, R. Cenni, C. Giusti, and F. Pacati, Nucl. Phys. **A420**, 38 (1984).

[3] J. Eden *et al.*, Phys. Rev. **C44**, 753 (1991).

[4] K. Garrow, High Energy Photoprotons from ^{12}C, Master's thesis, Queen's University, 1991.

[5] J. Ryckebusch *et al.*, Phys. Rev. **C49**, 2704 (1994).

[6] N. Chant and P. Roos, Phys. Rev. **C39**, 957 (1988).

[7] S. Cohen and D. Kurath, Nucl. Phys. **A141**, 145 (1970).

[8] D. Mack *et al.*, Phys. Rev. **C45**, 1767 (1992).

[9] I. MacGregor *et al.*, Nucl. Phys. **A533**, 269 (1991).

[10] A. V. D. Woude and R. J. D. Meijer, Nucl. Phys. **A258**, 199 (1975).

[11] R. Schumacher *et al.*, Phys. Rev. **C35**, 2205 (1988).

[12] D. Findlay and R. Owens, Nucl. Phys. **A279**, 385 (1977).

[13] G. Miller *et al.*, Nucl. Phys. **A586**, 125 (1995).

[14] J. Comfort and B. Karp, Phys. Rev. **C21**, 2162 (1980).

[15] L. Isaksson, *High-Resolution Measurement of the* $^{16}O(\gamma, pn)$ *Reaction*, PhD thesis, Lund University, 1995.

[16] B. Schoch, Phys. Lett. **109B**, 11 (1982).

[17] B. Schoch, Phys. Lett. **97B**, 41 (1980).

[18] B. Schoch, Phys. Lett. **41**, 80 (1978).

[19] B. Schoch, Nucl. Phys. **A229**, 93 (1974).

[20] B. Schoch, Nucl. Phys. **A384**, 414 (1982).

[21] P. Harty *et al.*, Phys. Rev. **C37**, 13 (1988).

[22] G. Jacob and T. A. Maris, Rev. Mod. Phys. **38**, 121 (1966).

[23] G. Jacob and T. A. Maris, Rev. Mod. Phys. **45**, 6 (1973).

[24] D. F. Jackson, **4**, 1 (1971).

[25] M. Barton and J. Smith, Phys. Rev. **95**, 573 (1954).

[26] H. Myers *et al.*, Phys. Rev. **99**, 1621 (1954).

[27] A. Odion *et al.*, Phys. Rev. **102**, 837 (1956).

[28] A. Wetterberg *et al.*, Phys. Rev. **104**, 1710 (1956).

[29] M. Barton and J. Smith, Phys. Rev. **110**, 1143 (1958).

[30] K. Gottfried, Nucl. Phys. **5**, 557 (1958).

[31] S. Hyman *et al.*, Phys. Rev. **C47**, 1184 (1993).

[32] I. Sick and J. Macarthy, Nucl. Phys. **A150**, 631 (1970).

[33] J. Londergan and G. Nixon, Phys. Rev. **C39**, 631 (1970).

[34] B.-E. Anderson *et al.*, Phys. Rev. **C51**, 2553 (1995).

[35] C. degli Atti, in *Intermediate Energy Nuclear Physics*, p. 65, Singapore, 1982, World Scientific Publishing Co Pte. Ltd.

[36] S. Boffi, C. Giusti, and F. Pacati, Nucl. Phys. **A359**, 91 (1981).

[37] S. Boffi, F. Pacati, C. Giusti, and F. Pacati, Nucl. Phys. **A436**, 438 (1985).

[38] D. G. Ireland and G. van der Steenhoven, Phys. Rev. **C49**, 2182 (1994).

[39] J. Johansson, H. Sherif, and G. Lotz, Nucl. Phys. **A605**, 517 (1996).

[40] J. Levinger, Phys. Rev. **84**, 43 (1951).

[41] H. Bethe, Rev. Mod. Phys. **9**, 223 (1937).

[42] D. Fleming, J. Hardy, and J. Cerny, Nucl. Phys. **A162**, 225 (1971).

[43] L. O. Dallin, PhD thesis, University of Saskatchewan, 1990.

[44] R. Laxdal, Master's thesis, University of Saskatchewan, 1980.

[45] K. Helgason, A large-area neutron detector, Master's thesis, University of Saskatchewan, 1995.

[46] B. Industries, *Photomultiplier Handbook*, Burle Technologies Inc., Lancaster Pennsylvania, 1980.

[47] J. Weil, Phys. Rev. **92**, 391 (1953).

[48] R. Cecil, D. Anderson, and R. Madey, Nucl. Instrum. Methods **161**, 439 (1979).

[49] K. Krane, *Introductory Nuclear Physics*, John Wiley and Sons Inc., New York, 1988.

[50] H. Gotoh and H. Yagi, Nucl. Instrum. Methods **96**, 485 (1971).

[51] A. D. Guerra, Nucl. Instrum. Methods **135**, 337 (1976).

[52] G. 3.21, *Cern program library W5013*, CERN Geneva, 1993.

[53] D. Grobatkov and V. Kryuchkov, Nucl. Instrum. Methods **A374**, 95 (1996).

[54] Rossi *et al.*, Phys. Rev. **C40**, 2412 (1989).

[55] R. Crawford *et al.*, Nucl. Phys. **A603**, 303 (1996).

[56] V. Pandharipande, I. Sick, and P. deWitt Huberts, Rev. Mod. Phys. **69**, 981 (1997).

[57] M. Leuschner *et al.*, Phys. Rev. **C49**, 995 (1994).

[58] A. Rauf, *Study of Photoproton Reactions*, PhD thesis, Lund University, 1995.

[59] M. Bernheim *et al.*, Nucl. Phys. **A375**, 381 (1982).

[60] C. Hoot *et al.*, Nucl. Phys. **A203**, 339 (1973).

[61] K. Amir-Azimi-Nili *et al.*, Nucl. Phys. **A625**, 633 (1997).

[62] A. Ramos, A. Polls, and W. Dickhoff, Nucl. Phys. **A503**, 1 (1989).

[63] H. Muther, G. Knehr, and A. Pols, Phys. Rev. **C52**, 2955 (1995).

[64] E. Tomusiak, H. Caplan, and E. Dressler, *New Vistas in Electro-Nuclear Physics*, Plenum Press, New York, 1988.

[65] R. Carrasco and E. Oset, 1994.

[66] J. Ryckebusch, L. Machneil, M. Vanderhaeghen, and M. Waroquie, Nucl. Phys. **A568**, 828 (1994).

Appendix A

Derivation of the (γ, p) and (γ, n) cross section in the direct knock-out formalism

In the following derivation the units are normally chosen so that $\hbar = c = 1$ and the vector notation is that letters with an arrow over the top refer to 3-vectors, while vectors in normal type are reserved for 4-vectors.

The amplitude for a transition from an initial state $\mid i >$ to a final state $\mid f >$ can be computed in the Hamiltonian Interaction picture via the scattering matrix or S-matrix and is given by

$$\begin{aligned} S_{fi} &= < f \mid S \mid i > \qquad (A.1) \\ &= lim_{t\to-\infty}^{t\to+\infty} < f \mid \sum_{n=0}^{\infty} \frac{1}{(i\hbar c)^n n!} \int_{t_i}^{t_f} d^4x_1 .... d^4x_n T\Big[H^I_{int}(x_1) .... H^I_{int}(x_n)\Big] \mid i > . \end{aligned}$$

In the above equation T is the time ordered product of the interaction Hamiltonian density operators $H^I_{int}(x_n)$ where in the case of photo-nuclear interactions

$$H^I_{int} = -\frac{1}{c} A_\mu(x) J^\mu(x) \qquad (A.2)$$

where A_μ is the quantized electromagnetic free field operator, J^μ is the total nuclear current and the repeated index μ signifies a four-vector inner product. The electromagnetic free field operator is given by

$$A_\mu(x) = \frac{1}{\sqrt{8\pi^3}} \sum_\lambda \int \frac{d^3k_\gamma}{\sqrt{2E_\gamma}} [\epsilon^\lambda_\mu a_{(\lambda)}(\vec{k}_\gamma) e^{-ik_\gamma \cdot x} + \epsilon^{\lambda *}_\mu a^\dagger_{(\lambda)}(\vec{k}_\gamma) e^{ik_\gamma \cdot x}] \qquad (A.3)$$

where $a_{(\lambda)}(\vec{k}_\gamma)$ and $a^\dagger_{(\lambda)}(\vec{k}_\gamma)$ are the annihilation and creation operators for a photon of polarization λ and momentum $\vec{k}_\gamma$. Inserting $H^I_{int}(x_n)$ and the electromagnetic free field operators (while retaining only the photon annihilation operator of the electromagnetic field) into S_{fi} yields to first order (n=1)

$$S_{fi} = -\frac{1}{i\sqrt{8\pi^3}} \frac{1}{\sqrt{2E_\gamma}} \int d^4x e^{-ik_\gamma \cdot x} < f, \vec{k_N} \vec{k}_{A-1} \mid \int d^3k_\gamma \epsilon^\lambda_\mu \cdot J^\mu(x) a_{(\lambda)}(\vec{k}_\gamma) \mid i, \vec{k}_A \vec{k}_\gamma > \qquad (A.4)$$

where $\vec{k}_A$ is the initial target 3-momentum, $\vec{k}_\gamma$ represents the photon momentum in a polarization state λ, $\vec{k}_N$ is the ejected nucleon 3-momentum and $\vec{k}_{A-1}$ is the 3-momentum of the A-1 recoil nucleus. One can separate the time and space compo-

nents of the nuclear current operator obtaining

$$S_{fi} = -\frac{1}{i\sqrt{8\pi^3}}\frac{1}{\sqrt{2E_\gamma}}\int d^4(x)e^{-ik_\gamma\cdot x} < f,\vec{k}_N\vec{k}_{A-1} \mid \int d^3k_\gamma\epsilon_\mu^\lambda\cdot e^{i\hat{p}\cdot x}J^\mu(0)e^{-i\hat{p}\cdot x}a_{(\lambda)}(\vec{k}) \mid i,\vec{k}_A\vec{k}_\gamma > \tag{A.5}$$

where $\hat{p}$ is the energy-momentum operator acting between the initial and final nuclear states. Using these operators as well as the photon annihilation operators and integrating over all photon momenta gives

$$\begin{aligned} S_{fi} &= -\frac{1}{i\sqrt{8\pi^3}}\frac{1}{\sqrt{2E_\gamma}}\int d^4(x)e^{-ik_\gamma\cdot x}\frac{e^{i(k_{A-1}+k_N)\cdot x}}{8\pi^3} \\ &\quad < f,\vec{k}_N\vec{k}_{A-1} \mid \epsilon_\mu^\lambda\cdot J^\mu(0) \mid i,\vec{k}_A > \frac{e^{-ik_A\cdot x}}{\sqrt{8\pi^3}} \\ &= -\frac{1}{i(2\pi)^6}\frac{1}{\sqrt{2E_\gamma}}\int d^4(x)e^{i(k_{A-1}+k_N-k_\gamma-k_A)\cdot x} \\ &\quad < f,\vec{k}_N\vec{k}_{A-1} \mid \epsilon_\mu^\lambda\cdot J^\mu(0) \mid i,\vec{k}_A > . \end{aligned} \tag{A.6}$$

If one assumes the impulse approximation and that the photon interacts with only a single nucleon then the A-1 recoil nucleus acts purely as a spectator. In this instance it is sufficient to consider only the one-body nuclear current operator acting on the struck nucleon and absorbed photon. Now consider an explicit form for the nuclear current operator $\vec{J}^\mu(\vec{x})$ such as

$$\begin{aligned} \vec{J}^\mu(\vec{x}) = -e\sum_{j=1}^{j=A}\Bigg\{ &\frac{1+\tau_3(j)}{i2M}\delta^3(\vec{x}_j-\vec{x})(\overrightarrow{\nabla}_j - \overleftarrow{\nabla}_j) \\ &-(\frac{1+\tau_3(j)}{2}+\frac{1-\tau_3(j)}{2})\delta^3(\vec{x}_j-\vec{x})\frac{\mu_j}{2M}\vec{\sigma}(j)\times\overrightarrow{\nabla}_j\Bigg\} \end{aligned} \tag{A.7}$$

and therefore,

$$\begin{aligned} \vec{J}^\mu(0) = -e\sum_{j=1}^{j=A}\Bigg\{ &\frac{1+\tau_3(j)}{iM}(\overleftarrow{\nabla}_j\delta^3(\vec{x}_j-0)+\delta^3(\vec{x}_j-0)\overrightarrow{\nabla}_j) \\ &-(\frac{1+\tau_3(j)}{2}+\frac{1-\tau_3(j)}{2})\delta^3(\vec{x}_j-0)\frac{\mu_j}{2M}\vec{\sigma}(j)\times\overrightarrow{\nabla}_j\Bigg\} \end{aligned} \tag{A.8}$$

In equations A.7 and A.8 the sum runs over all A target nucleons , τ_3 is the isospin operator for the j^{th} nucleon (= +1 for protons and -1 for neutrons), M is the mass of the nucleon, μ is the magnetic moment of the nucleon in nuclear magnitons, $\vec{\sigma}(j)$ is the Pauli spin operator, the complex variable i is to make sure the convection (the first term above) and the magnetic (second term in the above equation) terms of the

nuclear current add incoherently into the cross section and ∇ is the momentum operator $-i\hbar\frac{d}{d\vec{x}}$ where the arrow to the left implies complex conjugation of this operator. The two way acting gradient is necessary to make the convection current part of the nuclear current operator hermitian.

Now consider the convective part of the nuclear current operator acting on the plane waves of the absorbed photon in the initial state and the ejected nucleon in the final state, or more clearly one must evaluate

$$e^{i(E_N x_0 - \vec{k}_N\cdot\vec{x})} J^{\mu}_{conv}(0)\vec{\epsilon}^{\lambda}_{\mu} e^{-i(k_\gamma x_0 - \vec{k}_\gamma\cdot\vec{x})} = e^{i(E_N x_0 - \vec{k}_N\cdot\vec{x})}(-)e\sum_{j=1}^{j=A}\frac{1+\tau_3(j)}{i2M}$$
$$(\overleftarrow{\nabla}_j\delta^3(\vec{x}_j - 0) + \delta^3(\vec{x}_j - 0)\overrightarrow{\nabla}_j)\vec{\epsilon}^{\lambda}_{\mu} e^{-i(k_\gamma x_0 - \vec{k}_\gamma\cdot\vec{x})} \quad \text{(A.9)}$$

The gradient operating to the right can be turned into a gradient operating to the left using the following vector identity

$$\begin{aligned}\int_S f\vec{A}\cdot\hat{n}ds &= \int_V \vec{\nabla}\cdot(f\vec{A})d^3x \\ &= \int \vec{\nabla}f\cdot\vec{A}d^3x + \int(\vec{\nabla}\cdot\vec{A})fd^3x. \end{aligned} \quad \text{(A.10)}$$

Noting that the surface integral $\int_S f\vec{A}\cdot\hat{n}ds = 0$, since well-behaved wave functions must vanish at $\pm\infty$, and identifying $\vec{A}$ in Eq. (10) with $\vec{\epsilon}e^{i\vec{k}_\gamma\cdot\vec{x}}$ one can write

$$\begin{aligned}\overrightarrow{\nabla}_j\cdot\vec{\epsilon}e^{i\vec{k}_\gamma\cdot\vec{x}} &= -\overrightarrow{\nabla}_j e^{-i\vec{k}_N\cdot\vec{x}} \\ &= e^{-i\vec{k}_N\cdot\vec{x}}\overleftarrow{\nabla}_j \end{aligned} \quad \text{(A.11)}$$

where the fact that $\overrightarrow{\nabla}_j = -\overleftarrow{\nabla}_j$ has been used. Therefore the convective part of the nuclear current operator acting on the plane wave, $e^{i(E_0 x_0 - \vec{k}_N\cdot\vec{x})}$, assumed for the struck nucleon which is ejected by the interaction with a photon, yields a result

$$e^{i(E_N x_0 - \vec{k}_N\cdot\vec{x})} J^{\mu}_{conv}(0)\vec{\epsilon}^{\lambda}_{\mu} e^{-i(k_\gamma x_0 - \vec{k}_\gamma\cdot\vec{x})} =$$
$$e^{i(E_N x_0 - \vec{k}_N\cdot\vec{x})}\frac{-2e}{2iM}\vec{k}_N\cdot\vec{\epsilon}^{\lambda} e^{-i(k_\gamma x_0 - \vec{k}_\gamma\cdot\vec{x})}. \quad \text{(A.12)}$$

Now consider the magnetic part of the nuclear current operator acting between the initial photon plane wave and the plane wave representing the ejected nucleon. That is

$$e^{i(E_N x_0 - \vec{k}_N\cdot\vec{x})} J^{\mu}_{mag}(0)\cdot\vec{\epsilon}^{\lambda}_{\mu} e^{-i(E_\gamma x_0 - \vec{k}_\gamma\cdot\vec{x})} =$$
$$e\sum_{j=1}^{j=A} e^{i(E_N x_0 - \vec{k}_N\cdot\vec{x})}\left(\frac{1+\tau_3(j)}{2} + \frac{1-\tau_3(j)}{2}\right)\delta^3(\vec{x}_j - 0)$$
$$\frac{\mu_j}{2M}\sigma(\vec{j})\times\overrightarrow{\nabla}_j\cdot\vec{\epsilon}^{\lambda}_{\mu} e^{-i(E_\gamma x_0 - \vec{k}_\gamma\cdot\vec{x})}. \quad \text{(A.13)}$$

Carrying out the gradient to the right and reversing the order of the curl one obtains

$$e^{i(E_N x_0 - \vec{k}_N \cdot \vec{x})} J^{\mu}_{mag}(0) \cdot \vec{\epsilon}^{\lambda}_{\mu} e^{-i(E_\gamma x_0 - \vec{k}_\gamma \cdot \vec{x})} = (-) e^{i(E_N x_0 - \vec{k}_N \cdot \vec{x})} \frac{\mu_N \vec{k}_\gamma \times \vec{\sigma} \cdot \vec{\epsilon}^{\lambda}_{\mu}}{2m} e^{-i(E_\gamma x_0 - \vec{k}_\gamma \cdot \vec{x})}. \tag{A.14}$$

Using the results of equations (A.7) through (A.14) in Eq. (A.6) yields

$$\begin{aligned} S_{fi} &= \frac{1}{i(2\pi)^6} \frac{-e}{\sqrt{2k_\gamma}} \int d^4(x) e^{i(k_{A-1} + k_N - k_\gamma - k_A)\cdot x} \\ &\quad \left\{ \frac{\vec{k}_N \cdot \vec{\epsilon}^{\lambda}}{im} + \frac{\mu_N \vec{k}_\gamma \times \vec{\sigma} \cdot \vec{\epsilon}^{\lambda}_{\mu}}{2m} \right\} < f, \vec{k_N} \vec{k_{A-1}} \mid i, \vec{p}_A > \\ &= \frac{1}{i(2\pi)^6} \frac{-e}{\sqrt{2k_\gamma}} (2\pi)^4 \delta^4(k_{A-1} + k_N - k_\gamma - k_A) \\ &\quad \left\{ \frac{\vec{k}_n \cdot \vec{\epsilon}^{\lambda}}{im} + \frac{\mu_N \vec{k}_\gamma \times \vec{\sigma} \cdot \vec{\epsilon}^{\lambda}_{\mu}}{2m} \right\} < f, \vec{k_N} \vec{k_r} \mid i, \vec{p}_A > . \end{aligned} \tag{A.15}$$

Now the laboratory differential cross section is obtained by averaging over the initial photon polarizations, summing over the spins of the outgoing nucleon and bound nucleon, integrating over outgoing proton and recoil A-1 spectator nucleus, dividing by the various flux factors and VT so that

$$\begin{aligned} d\sigma &= \frac{1}{2} \sum_{\lambda} \sum_{\sigma m_s} \frac{|S_{fi}|^2}{VT(\eta)(\rho)} d^3 k_N d^3 k_{A-1} \\ &= \frac{1}{2} \sum_{\lambda} \sum_{\sigma m_s} \frac{(2\pi)^6 |S_{fi}|^2}{(2\pi)^4 \delta^4(k_N + k_{A-1} - k_A - k_\gamma)} \end{aligned} \tag{A.16}$$

where $VT = (2\pi)^4 \delta^4(k_N + k_{A-1} - k_A - k_\gamma)$, η is the flux density of photons in the lab equal to $\frac{1}{(2\pi)^3}$ and ρ is the target density equal to $\frac{1}{(2\pi)^3}$.

Since the convection part of the nuclear current contains no spin operators it is sufficient to carry out only the sum over the photon polarizations for the convection current and this is computed as follows.

$$\begin{aligned} \sum_{\lambda} \left| \vec{k}_N \cdot \vec{\epsilon}_\lambda \right|^2 &= \left| \vec{k}_N \cdot \vec{\epsilon}_+ \right|^2 + \left| \vec{k}_N \cdot \vec{\epsilon}_- \right|^2 \\ &= \frac{1}{2} \left| \vec{k}_N \cdot (\hat{\epsilon}_x + i\hat{\epsilon}_y) \right|^2 + \frac{1}{2} \left| \vec{k}_N \cdot (\hat{\epsilon}_x - i\hat{\epsilon}_y) \right|^2 \\ &= \frac{1}{2} \left| \vec{k}_{N_x} + i\vec{k}_{N_y} \right|^2 + \frac{1}{2} \left| \vec{k}_{N_x} - i\vec{k}_{N_y} \right|^2 \\ &= \frac{1}{2}(k^2_{N_x} + k^2_{N_y}) + + \frac{1}{2}(k^2_{N_x} + k^2_{N_y}) \end{aligned}$$

$$
\begin{aligned}
&= k_{N_x}^2 + k_{N_y}^2 \\
&= k_N^2 - k_{N_z}^2 \\
&= k_N^2 - k_N^2 \cos^2(\theta_{\gamma,N}) \\
&= k_N^2 \sin^2(\theta_{\gamma,N})
\end{aligned} \tag{A.17}
$$

where the identity $\epsilon_\pm = \mp\frac{1}{\sqrt{2}}(\hat{\epsilon}_x \pm i\hat{\epsilon}_y)$ has been used and note that for real photons $\epsilon_0 = 0$ reflects their pure transverse nature.

Since the magnetic part of the nuclear current is a pure spin flip transition, as mentioned previously the matrix element S_{fi}^{mag} must be evaluated between the spinors of the final outgoing nucleon $(\chi^{\frac{1}{2}}_{m_s})^\dagger$ and the initial bound nucleon $\chi^{\frac{1}{2}}_{m_l}$. More precisely this requires evaluation of

$$
\sum_\lambda \left| (\chi^{\frac{1}{2}}_{m_s})^\dagger \vec{k}_\gamma \times \vec{\sigma} \cdot \vec{\epsilon}_\lambda \chi^{\frac{1}{2}}_{m_l} \right|^2 . \tag{A.18}
$$

Consider first the sum over the transverse photon polarization states so one can write

$$
\sum_\lambda \left| \vec{k}_\gamma \times \vec{\sigma} \cdot \vec{\epsilon}_\lambda \right|^2 = \left| \vec{k}_\gamma \times \vec{\sigma} \cdot \epsilon_+ \right|^2 + \left| \vec{k}_\gamma \times \vec{\sigma} \cdot \epsilon_- \right|^2 \tag{A.19}
$$

where if the incident photon direction is chosen so that $\vec{k} = \left|\vec{k}\right| \hat{z}$ then the above equation reduces to

$$
\vec{k}_\gamma \times \vec{\sigma} = k_z \sigma_x \hat{y} - k_z \sigma_y \hat{x}. \tag{A.20}
$$

Using Eq. (A.20) in Eq. (A.19) yields

$$
\begin{aligned}
\sum_\lambda \left| \vec{k}_\gamma \times \vec{\sigma} \cdot \vec{\epsilon}_\lambda \right|^2 &= \left| k_z(\sigma_x \hat{y} - \sigma_y \hat{x}) \cdot \frac{-1}{\sqrt{2}}(\hat{x} + i\hat{y}) \right|^2 + \left| k_z(\sigma_x \hat{y} - \sigma_y \hat{x}) \cdot \frac{1}{\sqrt{2}}(\hat{x} - i\hat{y}) \right|^2 \\
&= \left| \frac{-k_z}{\sqrt{2}}(-\sigma_y + i\sigma_x) \right|^2 + \left| \frac{k_z}{\sqrt{2}}(-\sigma_y - i\sigma_x) \right|^2 .
\end{aligned} \tag{A.21}
$$

Recalling the form of the spin flip operators

$$
\sigma_\pm = \mp\frac{1}{\sqrt{2}}(i\sigma_x \pm \sigma_y) \tag{A.22}
$$

and therefore

$$
i\sigma_\pm = \mp\frac{1}{\sqrt{2}}(i\sigma_x \mp \sigma_y) \tag{A.23}
$$

and identifying this form in Eq. (21) one can now rewrite Eq. (21) in terms of the

spin flip operators as

$$\sum_{\lambda} \left| \vec{k}_\gamma \times \vec{\sigma} \cdot \vec{\epsilon}_\lambda \right|^2 = |k_z i\sigma_+|^2 + |-ik_z\sigma_-|^2 . \tag{A.24}$$

If one assumes that both the bound nucleon and ejected nucleon have equal probability of being in a spin up or spin down state, then carrying out the sum over the initial and final proton spinors yields

$$\begin{aligned}
\sum_{\lambda\sigma m_s} \left| (\chi^{\frac{1}{2}}_{\sigma})^\dagger \vec{k}_\gamma \times \vec{\sigma} \cdot \vec{\epsilon}_\lambda \chi^{\frac{1}{2}}_{m_s} \right|^2 &= \left| \frac{1}{\sqrt{2}} \Big[(01) + (10) \Big] i k_z \sigma_+ \frac{1}{\sqrt{2}} \left[\begin{pmatrix} 1 \\ 0 \end{pmatrix} + \begin{pmatrix} 0 \\ 1 \end{pmatrix} \right] \right|^2 + \\
&\quad \left| \frac{1}{\sqrt{2}} \Big[(01) + (10) \Big] - i k_z \sigma_- \frac{1}{\sqrt{2}} \left[\begin{pmatrix} 1 \\ 0 \end{pmatrix} + \begin{pmatrix} 0 \\ 1 \end{pmatrix} \right] \right|^2 \\
&= \left| \frac{1}{\sqrt{2}} \Big[(01) + (10) \Big] \frac{-ik_z}{\sqrt{2}} \begin{pmatrix} 02 \\ 00 \end{pmatrix} \frac{1}{\sqrt{2}} \left[\begin{pmatrix} 1 \\ 0 \end{pmatrix} + \begin{pmatrix} 0 \\ 1 \end{pmatrix} \right] \right|^2 + \\
&\quad \left| \frac{1}{\sqrt{2}} \Big[(01) + (10) \Big] \frac{-ik_z}{\sqrt{2}} \begin{pmatrix} 00 \\ 20 \end{pmatrix} \frac{1}{\sqrt{2}} \left[\begin{pmatrix} 1 \\ 0 \end{pmatrix} + \begin{pmatrix} 0 \\ 1 \end{pmatrix} \right] \right|^2 \\
&= \left(\frac{k_z}{2} + \frac{k_z}{2} \right)^2 \\
&= k_\gamma^2
\end{aligned} \tag{A.25}$$

where the fact that $|\vec{k}_\gamma| = k_z$ has been used in the last line of the above equation.

Next, using the results of Equations (A.17) and (A.25) as well as the explicit form of S_{fi} given in Equation (A.15) one can rewrite the differential cross section of Equation (A.16) as

$$\begin{aligned}
d\sigma &= \frac{e^2 (2\pi)^8 \left| \delta(k_{A-1} + k_N - k_\gamma - k_A) \right|^2 (2\pi)^6 \left| < f, \vec{k}_{A-1} \mid i, \vec{k}_A > \right|^2}{(2\pi)^{12} (2\pi)^4 \delta(k_{A-1} + k_N - k_\gamma - k_A)(2) 2k_\gamma} \\
&\quad \cdot \left[\frac{k_p^2}{m^2} \sin^2(\theta_{\gamma,p}) + \frac{k_\gamma^2}{2m^2} \mu_p^2 + \frac{k_\gamma^2}{2m^2} \mu_n^2 \right] d^3k_{A-1} d^3k_N \\
&= \frac{e^2 \delta(k_{A-1} + k_N - k_\gamma - k_A) \left| < f, \vec{k}_{A-1} \mid i, \vec{k}_A > \right|^2}{(2\pi)^2 (2) 2k_\gamma} \\
&\quad \cdot \left[\frac{k_p^2}{m^2} \sin^2(\theta_{\gamma,p}) + \frac{k_\gamma^2}{2m^2} \mu_p^2 + \frac{k_\gamma^2}{2m^2} \mu_n^2 \right] d^3k_{A-1} d^3k_N .
\end{aligned} \tag{A.26}$$

Next consider the integration over the A-1 recoil nucleus and the ejected nucleon, that is

$$\delta(\vec{k}_{A-1} + \vec{k}_N - \vec{k}_\gamma - \vec{k}_A) \delta(E_{A-1} + E_N - \left| \vec{k}_\gamma \right| - E_A) d^3k_{A-1} d^3k_N . \tag{A.27}$$

The integration over the A-1 recoil sets momentum conservation and noting that in

the lab system $\vec{k}_A = 0$ and therefore $E_A = m_A$ the above equation reduces to

$$\delta(E_{A-1} + E_N - \left|\vec{k}_\gamma\right| - E_A) d^3k_N \tag{A.28}$$

where now the momentum conservation in the form of

$$\vec{k}_{A-1} + \vec{k}_N = \vec{k}_\gamma \tag{A.29}$$

must be enforced. One is now left with the integration over the outgoing nucleon and the energy conserving delta function. Noting the result

$$\int f(x)\delta(g(x))d^3x = \frac{f(x)x^2 d\Omega_x}{\left|\frac{d}{dx}g(x)\right|} \tag{A.30}$$

Equation (A.28) becomes

$$\delta(E_{A-1} + E_N - \left|\vec{k}_\gamma\right| - m_A)d^3k_N = \frac{k_N^2 d\Omega_{k_N}}{\left|\frac{d}{d_{k_N}}(E_{A-1} + E_N - \left|\vec{k}_\gamma\right| - m_A)\right|}. \tag{A.31}$$

Using the momentum conservation stated in Eq. (29) and noting that only $E_f = E_{A-1} + E_N$ is a function of k_N one can write

$$\begin{aligned}
\left|\frac{dE_f}{d_{k_N}}\right| &= \left|\frac{d}{d_{k_N}}(E_{A-1} + E_N - \left|\vec{k}_\gamma\right| - m_A)\right| \\
&= \left|\frac{d}{d_{k_N}}(\frac{k_{A-1}^2}{2m_{A-1}} + m_{A-1} + \frac{k_N^2}{2m_N} + m_N)\right| \\
&= \left|\frac{d}{d_{k_N}}(\frac{k_\gamma^2 + k_N^2 - 2k_\gamma k_N \cos(\theta_{\gamma,N})}{2m_{A-1}} + m_{A-1} + \frac{k_N^2}{2m_N} + m_N)\right| \\
&= \left|\frac{m_N(k_N - k_\gamma\cos(\theta_{\gamma,N})) + m_{A-1}k_N}{m_{A-1}m_N}\right|
\end{aligned} \tag{A.32}$$

where the momentum conservation requirement $\vec{k}_{A-1} = \vec{k}_\gamma - \vec{k}_N$ set in Eq. (A.29) has been used. Using the result of Equations (A.27) through (A.32) one can now rewrite the differential cross section given in Eq. (A.26) as

$$\begin{aligned}
\frac{d\sigma}{d\Omega} = \frac{e^2}{16\pi^2}\frac{k_N^2}{k_\gamma}\frac{dk_N}{dE_f}&\left|< f, \vec{k}_{A-1} \mid i, \vec{k}_A >\right|^2 \\
&\cdot\left[\frac{k_p^2}{m^2}\sin^2(\theta_{\gamma,p}) + \frac{k_\gamma^2}{2m^2}\mu_p^2 + \frac{k_\gamma^2}{2m^2}\mu_n^2\right]
\end{aligned} \tag{A.33}$$

where $\frac{dk_N}{dE_f}$ is equal to the reciprocal of Eq. (A.32) or

$$\begin{aligned}\left|\frac{dk_N}{d_{E_f}}\right| &= \frac{1}{\left|\frac{dE_f}{dk_N}\right|} \\ &= \left|\frac{m_{A-1}m_N}{m_N(k_N - k_\gamma\cos(\theta_{\gamma,N})) + m_{A-1}k_N}\right|. \end{aligned} \tag{A.34}$$

If the overlap matrix element between initial and final states is defined by taking the Fourier transform with respect to the initial bound state nucleon momentum which in the plane wave impulse approximation (PWIA) is $\vec{q} = -\vec{k}_{A_1} = \vec{k}_N - \vec{k}_\gamma$ then one can write

$$\begin{aligned}\phi_{nljm}(\vec{q}) &= \int e^{i\vec{q}\cdot\vec{r}} < f, \vec{k}_{A-1} \mid\mid i, \vec{k}_A > d^3r \\ &= \int e^{i\vec{q}\cdot\vec{r}}\phi_{nljm}(\vec{r})d^3r \\ &= C^{l\frac{1}{2}j}_{m_l m_s m}\int d^3r e^{i\vec{q}\cdot\vec{r}}R_{nl}(r)Y_{lm}(\hat{r})\chi^{\frac{1}{2}}_{m_s} \\ &= NC^{l\frac{1}{2}j}_{m_l m_s m}R_{nl}(r)Y_{lm}(\hat{q})\chi^{\frac{1}{2}}_{m_s} \end{aligned} \tag{A.35}$$

where N is a normalization constant to be determined later and the explicit form of $\phi(\vec{q})$ will be derived later. Now the differential cross section will be proportional to the square of Eq. (35) summed over the bound nucleon $\chi^{\frac{1}{2}}_{m_l}$ and ejected nucleon $\chi^{\frac{1}{2}}_{m_s}$ spinors. This requires the evaluation of

$$\begin{aligned}\sum_m |\phi_{nljm}(\vec{q})|^2 = \sum_{mm_s} C^{l\frac{1}{2}j}_{m-m_s,m_s,m}C^{l\frac{1}{2}j}_{m-m_s,m_s,m}\sum_{m_l}\left|(\chi^{\frac{1}{2}}_{m_s})^\dagger\chi^{\frac{1}{2}}_{m_l}\right|^2 \\ Y^*_{lm-m_s}(\hat{q})Y_{lm-m_s}(\hat{q})\,|R_{nl}(q)|^2 \end{aligned} \tag{A.36}$$

where the substitution $m_l = m - m_s$ has been used. Next using the relation

$$Y^*_{lm}(\hat{r}) = (-)^m Y_{l-m}(\hat{r})$$

as well as the fact

$$\begin{aligned}\sum_{m_l}(\chi^{\frac{1}{2}}_{m_s})^\dagger\chi^{\frac{1}{2}}_{m_l} &= (\chi^{\frac{1}{2}}_{m_s})^\dagger\chi^{\frac{1}{2}}_{m_l}\delta_{m_s m_l} \\ &= (\chi^{\frac{1}{2}}_{m_s})^\dagger\chi^{\frac{1}{2}}_{m_s} \\ &= 1 \end{aligned}$$

Equation (A.36) becomes

$$\sum_m |\phi_{nljm}(\vec{q})|^2 = \sum_{mm_s} C^{l\frac{1}{2}j}_{m-m_s,m_s,m}C^{l\frac{1}{2}j}_{m-m_s,m_s,m}$$

$$(-)^{m-m_s} Y_{lm_s-m}(\hat{q}) Y_{lm-m_s}(\hat{q}) \, |R_{nl}(q)|^2 \, . \qquad \text{(A.37)}$$

Next using the addition theorem for spherical harmonics which states

$$Y_{l_1 m_1}(\hat{r}) Y_{l_2 m_2}(\hat{r}) = \frac{\hat{l}_1 \hat{l}_2}{\sqrt{4\pi}\hat{l}_3} C^{l_1 l_2 l_3}_{000} C^{l_1 l_2 l_3}_{m_1 m_2 m_3} Y_{l_3 m_1+m_2}(\hat{r})$$

in Eq. (A.37) one obtains

$$\begin{aligned} \sum_m |\phi_{nljm}(\vec{q})|^2 \;\; = \;\; & \sum_{m m_s l_3} C^{l\frac{1}{2}j}_{m-m_s,m_s,m} C^{l\frac{1}{2}j}_{m-m_s,m_s,m} (-)^{m-m_s} \frac{\hat{l}\hat{l}}{\sqrt{4\pi}\hat{l}_3} \\ & C^{lll_3}_{000} C^{lll_3}_{m-m_s,m_s-m,0} Y_{l_3 0}(\hat{q}) \, |R_{nl}(q)|^2 \, . \end{aligned} \qquad \text{(A.38)}$$

Next it is required to get the summation index m_s freed from the phase factor and to perform the sum over m_s. To do this we make use of the relation

$$\sum_\beta C^{abe}_{\alpha\beta} C^{edc}_{\alpha+\beta,\delta} C^{bdf}_{\beta\delta} = \hat{e}\hat{f} W(abcd;ef) C^{afc}_{\alpha,\beta+\delta} \qquad \text{(A.39)}$$

where $W(abcd;ef)$ is the Racah coefficient. If we identify $C^{eba}_{-\alpha-\beta,\beta,-\alpha}$ with $C^{l\frac{1}{2}j}_{m-m_s,m_s,m}$ then the required form is

$$C^{abe}_{\alpha\beta} = (-)^{\frac{1}{2}+m_s} \frac{\hat{j}}{\hat{l}} C^{j,\frac{1}{2}l}_{-m,m_s,m_s-m} \qquad \text{(A.40)}$$

where the Clebsch Gorden relation

$$C(j_1 j_2 j_3 m_1 m_2 m_3) = (-)^{j_2+m_2} \frac{\hat{j}_3}{\hat{j}_1} C(j_3 j_2 j_1 \, -m_3 m_2 - m_1)$$

has been used. Next identifying $C^{dbf}_{\delta\beta}$ with $C^{l\frac{1}{2}j}_{m-m_s,m_s,m}$ then the required form is

$$C^{bdf}_{\beta\delta} = (-)^{\frac{1}{2}+l-j} C^{\frac{1}{2}lj}_{m_s,m-m_s,m} \qquad \text{(A.41)}$$

where the Clebsch Gorden relation

$$C(j_1 j_2 j_3 m_1 m_2 m_3) = (-)^{j_1+j_2-j_3} C(j_2 j_1 j_3 m_2 m_1 m_3)$$

has been used. Finally, identifying $C^{edc}_{-\alpha-\beta,-\delta}$ with $C^{lll_3}_{m-m_s,m_s-m,0}$ then the required form is

$$C^{edc}_{\alpha+\beta,\delta} = (-)^{l+l-l_3} C^{lll_3}_{m_s-m,m-m_s,0} \qquad \text{(A.42)}$$

where the Clebsch Gorden relation

$$C(j_1 j_2 j_3 m_1 m_2 m_3) = (-)^{j_1+j_1-j_3} C(j_1 j_2 j_3 - m_1 - m_2 - m_3)$$

has been used. Using the rearrangements of the three Clebsch Gorden coefficients we can now write Eq. (A.38) as

$$\begin{aligned}\sum_m |\phi_{nljm}(\vec{q})|^2 &= \sum_{m_s m l_3} (-)^{m-m_s} (-)^{\frac{1}{2}+m_s} \frac{\hat{j}}{\hat{l}} C^{j\frac{1}{2}l}_{-m,m_s,m_s-m} \\ &\quad (-)^{\frac{1}{2}+l-j} C^{\frac{1}{2}lj}_{m_s,m-m_s,m} (-)^{l+l-l_3} C^{lll_3}_{m_s-m,m-m_s,0} \\ &\quad \frac{\hat{l}\hat{l}}{\sqrt{4\pi}\hat{l}_3} C^{lll_3}_{000} Y_{l_3 0}(\hat{q}) \, |R_{nl}(q)|^2 \end{aligned} \tag{A.43}$$

and now employing the Racah relation of Eq. (A.39) the above equation can be rewritten as

$$\begin{aligned}\sum_m |\phi_{nljm}(\vec{q})|^2 &= \sum_{m l_3} \frac{\hat{l}\hat{l}}{\sqrt{4\pi}\hat{l}_3} C^{lll_3}_{000} Y_{l_3 0}(\hat{q}) \, |R_{nl}(q)|^2 \\ &\quad (-)^{m+1+3l-j-l_3} \frac{\hat{j}}{\hat{l}} \hat{l}\hat{j} W(j\tfrac{1}{2} l_3 l; lj) C^{jjl_3}_{-m,m,0} \end{aligned} \tag{A.44}$$

where W is the Racah coefficient and can be written in terms of a phase and a 6-j coefficient using

$$W(abcd; ef) = (-)^{-a-b-c-d} \left\{ \frac{abe}{dcf} \right\}$$

and using this result in Eq. (A.44) gives

$$\begin{aligned}\sum_m |\phi_{nljm}(\vec{q})| &= \sum_{m l_3} \frac{\hat{l}^2 \hat{j}^2}{\sqrt{4\pi}\hat{l}_3} Y_{l_3 0}(\hat{q}) C^{lll_3}_{000} \, |R_{nlj}(q)|^2 \\ &\quad (-)^{m+1+3l-j-l_3} (-)^{-j-\frac{1}{2}-l_3-l} \left\{ \frac{j\frac{1}{2}l}{ll_3 j} \right\} C^{jjl_3}_{-m,m,0} \\ &= \sum_{m l_3} \frac{\hat{l}^2 \hat{j}^2}{\sqrt{4\pi}\hat{l}_3} Y_{l_3 0}(\hat{q}) C^{lll_3}_{000} \, |R_{nlj}(q)|^2 \\ &\quad (-)^{m+\frac{1}{2}-2j+2l-2l_3} \left\{ \frac{j\frac{1}{2}l}{ll_3 j} \right\} C^{jjl_3}_{-m,m,0}. \end{aligned} \tag{A.45}$$

Next to remove the m dependence in phase one can make use of

$$1 = C^{j0j}_{m,0,m}$$

$$= \hat{j}(-)^{j-m} C^{jj0}_{m,-m,0}$$
$$= \hat{j}(-)^{j-m}(-)^{j+j-0} C^{jj0}_{-m,m,0}$$

where the Clebsch Gorden relations

$$C(j_1 j_2 j_3 m_1 m_2 m_3) = (-)^{j_1 - m_1} \frac{\hat{j}_3}{\hat{j}_2} C(j_1 j_3 j_2 m_1 - m_3 - m_2)$$

and

$$C(j_1 j_2 j_3 m_1 m_2 m_3) = (-)^{j_1 + j_2 - j_3} C(j_2 j_1 j_3 m_2 m_1 m_3)$$

were used. So inserting this result in the above equation gives

$$\sum_m |\phi_{nljm}(\vec{q})| = \sum_{ml_3} \frac{\hat{l}^2 \hat{j}^2}{\sqrt{4\pi}\hat{l}_3} Y_{l_3 0}(\hat{q}) C^{lll_3}_{000} |R_{nlj}(q)|^2$$
$$(-)^{m+\frac{1}{2}-2j+2l-2l_3} \left\{ \begin{matrix} j & \frac{1}{2} & l \\ l & l_3 & j \end{matrix} \right\} C^{jjl_3}_{-m,m,0} \hat{j}(-)^{j-m}(-)^{j+j-0} C^{jj0}_{-m,m,0}. \qquad \text{(A.46)}$$

Noting that

$$\sum_m C^{jjl_3}_{-m,m,0} C^{jj0}_{-m,m,0} = \delta_{l_3 0}$$

and using the fact $Y_{00} = \frac{1}{\sqrt{4\pi}}$

$$\sum_m |\phi_{nljm}(\vec{q})| = \sum_{l_3} (-)^{\frac{1}{2}+2l+j} \frac{\hat{l}^2 \hat{j}^3}{4\pi} C^{ll0}_{000} |R_{nlj}(q)|^2 \qquad (-)^{\frac{1}{2}+j+2l} \left\{ \begin{matrix} j & \frac{1}{2} & l \\ l & 0 & j \end{matrix} \right\}. \qquad \text{(A.47)}$$

One also can make use of the results

$$C^{ll0}_{000} = (-)^l \frac{1}{\hat{l}} \qquad \text{(A.48)}$$

and

$$\left\{ \begin{matrix} j & \frac{1}{2} & l \\ l & 0 & j \end{matrix} \right\} = (-)^{j+\frac{1}{2}+l} \frac{1}{\hat{j}\hat{l}} \qquad \text{(A.49)}$$

where the following relation was used for the above result

$$\left\{ \begin{matrix} j_3 & j_1 & j_2 \\ j_2 & 0 & j_3 \end{matrix} \right\} = (-)^{j_1+j_2+j_3} \frac{1}{\hat{j}_2 \hat{j}_3}.$$

So that inserting equations (A.49) and (A.50) into Eq. (A.48) one obtains

$$\begin{aligned}\sum_m |\phi_{nljm}(\vec{q})| &= (-)^{\frac{1}{2}+2l+j}\frac{\hat{l}^2\hat{j}^3}{4\pi}(-)^l\frac{1}{\hat{l}}|R_{nlj}(q)|^2(-)^{\frac{1}{2}+j+2l}(-)^{j+\frac{1}{2}+l}\frac{1}{\hat{j}\hat{l}} \\ &= (-)^{1+2j+4l}\frac{\hat{j}^2}{4\pi}|R_{nlj}(q)|^2. \qquad \text{(A.50)}\end{aligned}$$

Since 2j must be an integer the phase $(-)^{1+2j+4l}$ will be even so that

$$\sum_m |\phi_{nljm}(\vec{q})| = \frac{\hat{j}^2}{4\pi}|R_{nlj}(q)|^2. \qquad \text{(A.51)}$$

Next the question of the form of $|R_{nlj}(q)|^2$ will be discussed.

$$\int d^3r e^{i\vec{q}\cdot\vec{r}}R_{nl}(r)Y_{lm}(\hat{r}) = R_{nl}(q)Y_{lm}(\hat{q}). \qquad \text{(A.52)}$$

Let

$$R_{nl}(r)Y_{lm}(\hat{r}) = RY.$$

Now consider

$$\int d^3r e^{i\vec{q}\cdot\vec{r}}\left[\frac{-\hbar^2}{2m}\vec{\nabla}_r^2 + \frac{1}{2}m\omega^2r^2\right]RY = \int d^3r e^{i\vec{q}\cdot\vec{r}}ERY. \qquad \text{(A.53)}$$

Now one can integrate by parts twice in order to transfer $\vec{\nabla}_r^2$ to $\vec{\nabla}_q^2$. so that the above Schroedinger equation becomes

$$\frac{\hbar^2q^2}{2m}\int e^{i\vec{q}\cdot\vec{r}}RY\,d^3r + \frac{1}{2}m\omega^2\int r^2e^{i\vec{q}\cdot\vec{r}}RY\,d^3r = E\int e^{i\vec{q}\cdot\vec{r}}RY\,d^3r. \qquad \text{(A.54)}$$

Noting the definition of $\phi(\vec{q})$ and that $\vec{\nabla}_q^2e^{i\vec{q}\cdot\vec{r}} = -r^2$ the above equation can be rewritten as

$$\frac{\hbar^2q^2}{2m}\phi(\vec{q}) - \frac{1}{2}m\omega^2\vec{\nabla}_q^2\phi(\vec{q}) = E\phi(\vec{q}). \qquad \text{(A.55)}$$

Now recall that the Schroedinger equation is

$$(\vec{\nabla}_r^2 - \frac{m_2\omega^2r_2}{\hbar^2})RY = \frac{-2m}{\hbar^2}ERY \qquad \text{(A.56)}$$

where it is common to define $\alpha = \frac{m\omega}{\hbar}$ and $E = N\hbar\omega$ so the Schrodinger equation above becomes

$$(\vec{\nabla}_r^2 - \alpha^4r^2)RY = -\alpha^2(2N)RY. \qquad \text{(A.57)}$$

Rewriting Eq. (A.54) above into this form we obtain

$$(\vec{\nabla}_q^2 - \frac{1}{\alpha^4}q^2)\phi(\vec{q}) = -\frac{1}{\alpha^2}2N\phi(\vec{q}). \tag{A.58}$$

Therefore, by analogy with the solution of the Schroedinger equation the radial wave function piece in $\phi(\vec{q})$ will have the same form as the solution of the Schroedinger equation with α replaced by $\frac{1}{\alpha}$ and the angular Y_{lm} is of course the same.

Now the question of the normalization of $\phi(\vec{q})$ previously mentioned in Eq. (A.35) will be determined. We know

$$N R_{nlj}(q)Y_{lm}(\hat{q}) = \int d^3r e^{i\vec{q}\cdot\vec{r}} R_{nlj}(r)Y_{lm}(\hat{r}) \tag{A.59}$$

so that squaring each side and integrating by d^3q one obtains

$$\int N^2 |R_{nlj}(q)|^2 q^2 dq \int Y_l^*m(\hat{q})Y_lm(\hat{q})d\Omega \;=\; \int d^3r d^3r' d^3q e^{i\vec{q}\cdot(\vec{r}-\vec{r}')} R_{nlj}(r)R_{nlj}(r')Y_l^*m(\hat{r})Y_lm(\hat{r}') \tag{A.60}$$

Now by definition of the spherical harmonics

$$\int Y_l^*m(\hat{q})Y_lm(\hat{q})d\Omega = 1$$

so that Eq. (A.59) above becomes

$$\int N^2 |R_{nlj}(q)|^2 q^2 dq = \int d^3r d^3r' 8\pi^3 \delta(\vec{r}-\vec{r}') R_{nlj}(r)R_{nlj}(r')Y_l^*m(\hat{r})Y_lm(\hat{r}') \tag{A.61}$$

where

$$\int d^3q e^{i\vec{q}\cdot(\vec{r}-\vec{r}')} = 8\pi^3\delta(\vec{r}-\vec{r}').$$

We are now left with

$$\int N^2 |R_{nlj}(q)|^2 q^2 dq = 8\pi^3 \int r^2 |R_{nlj}(r)|^2 dr \tag{A.62}$$

where the fact that the spherical harmonics are normalized to unity has been employed. Furthermore, if one notes that

$$\int r^2 |R_{nlj}(r)|^2 dr = 1$$

one is left with

$$\int N^2 |R_{nlj}(q)|^2 q^2 dq = N^2 8\pi^3 \tag{A.63}$$

noting that one desires

$$\int N^2 \left|R_{nlj}(q)\right|^2 q^2 dq = 1. \tag{A.64}$$

It is apparent that the correct normalization to satisfy Eq. (64)

$$N = \frac{1}{\sqrt{8\pi^3}} \tag{A.65}$$

So for example for a $p_{\frac{1}{2}}$ nucleon in ^{16}O one obtains

$$R_{01} = \sqrt{8\pi^3}\sqrt{\frac{8}{3\alpha^3\sqrt{\pi}}}\frac{q}{\alpha}e^{-\frac{q^2}{2\alpha^2}}. \tag{A.66}$$

Finally one defines the unit normalized momentum density satisfying Eq. (A.64) as

$$\Omega(q) \equiv \frac{1}{8\pi^3}\sum_m \left|\phi_{nljm}(\vec{q})\right|^2$$

which for a $p_{\frac{1}{2}}$ nucleon in ^{16}O yields

$$\begin{aligned}\Omega(q) &= \frac{1}{8\pi^3}\frac{1}{4\pi}\hat{j}^2\left|R_{01}\right|^2 \\ &= \frac{2j+1}{4\pi}\frac{1}{8\pi^3}8\pi^3\frac{8}{3\sqrt{\pi}}\frac{q^2}{\alpha^5}e^{-\frac{q^2}{\alpha^2}}.\end{aligned} \tag{A.67}$$

Therefore, with the assumption that in the plane wave impulse approximation (PWIA) the differential cross section is proportional to the square of the single particle momentum density (as derived in Equations (A.35) to (A.68)) evaluated at a momentum $\vec{q} = \vec{k}_N - \vec{k}_\gamma$ the differential cross section of Eq. (33) can be rewritten using equations (A.51) and (A.66) as

$$\begin{aligned}\frac{d\sigma}{d\Omega} = \frac{e^2}{16\pi^2}\frac{k_N^2}{k_\gamma}\frac{dk_N}{dE_f}\frac{1}{8\pi^3}\sum_m \left|\phi_{nljm}(\vec{q})\right|^2 \\ \cdot\left[\frac{k_p^2}{m^2}\sin^2(\theta_{\gamma,p}) + \frac{k_\gamma^2}{2m^2}\mu_p^2 + \frac{k_\gamma^2}{2m^2}\mu_n^2\right]\end{aligned} \tag{A.68}$$

where $\frac{dk_N}{dE_f}$ is given in Eq. (A.34) and

$$\sum_m \left|\phi_{nljm}(\vec{q})\right|^2 = \frac{8\pi^3\hat{j}^2}{4\pi}\left|R_{nlj}(q)\right|^2. \tag{A.69}$$

Now defining a single particle momentum density one obtains the differential cross

section as

$$\frac{d\sigma}{d\Omega} = \frac{\pi e^2}{2}\frac{k_N^2}{k_\gamma}\frac{dk_N}{dE_f}\Omega(q)\left[\frac{k_p^2}{m^2}\sin^2(\theta_{\gamma,p}) + \frac{k_\gamma^2}{2m^2}\mu_p^2 + \frac{k_\gamma^2}{2m^2}\mu_n^2\right] \tag{A.70}$$

where

$$\Omega(q) = \frac{1}{8\pi^3}\sum_m |\phi_{nljm}(\vec{q})|^2 \tag{A.71}$$

and $\frac{dk_n}{dE_f}$ is given by Eq. (A.34). Using units of $\hbar = c = 1$ and the fine structure constant is

$$\alpha_{fine} = \frac{e^2}{4\pi}$$

so that

$$\frac{d\sigma}{d\Omega} = 2\pi^2\alpha_{fine}\frac{k_N^2}{k_\gamma}\frac{dk_N}{dE_f}\Omega(q)\left[\frac{k_p^2}{m^2}\sin^2(\theta_{\gamma,p}) + \frac{k_\gamma^2}{2m^2}\mu_p^2 + \frac{k_\gamma^2}{2m^2}\mu_n^2\right]. \tag{A.72}$$

So explicitly for the case of the photon ejection of a nucleon from ^{16}O using Eq. (A.71) one obtains

$$\begin{aligned}\frac{d\sigma}{d\Omega} = 2\pi^2\alpha_{fine}&\frac{k_N^2}{k_\gamma}\frac{dk_N}{dE_f}\frac{\hat{j}^2 8\pi^3}{4\pi 8\pi^3}\frac{8}{3\sqrt{\pi}}\frac{q^2}{\alpha^5}e^{-\frac{q^2}{\alpha^2}} \\ &\cdot\left[\frac{k_p^2}{m^2}\sin^2(\theta_{\gamma,p}) + \frac{k_\gamma^2}{2m^2}\mu_p^2 + \frac{k_\gamma^2}{2m^2}\mu_n^2\right]\end{aligned} \tag{A.73}$$

where $\hat{j}^2 = 2$ must be used. Finally to convert the above cross section to $\frac{\mu b}{sr}$ the above equation must be multiplied by 0.3893.

Appendix B
Inclusive Photoprotons from ^{12}C

K.R.Garrow, H.S.Caplan, K.G.Fissum, E.L.Hallin, R.E.Pywell,
D.M.Skopik and J.M.Vogt, Saskatchewan Accelerator Laboratory,
University of Saskatchewan, Saskatoon, Saskatchewan, Canada S7N 0W0
J.W.Jury Department of Physics, Trent University,
Peterborough, Ontario, Canada K9J 7B8
G. V.O'Rielly School of Physics, University of Melbourne,
Parkville, Australia 3052

Abstract

An inclusive measurement of the $^{12}C(\gamma, p)X$ reaction was carried out using the tagged photon facility at the Saskatchewan Accelerator Laboratory. Photoproton spectra were obtained for the photon energy range from 177 to 217 MeV at the laboratory angles $\theta_p = 51°, 81°, 109°$ and $141°$. When the inclusive proton spectra were plotted as a function of momentum, structures indicative of both the quasideuteron (QD) and the quasifree pion production (QFPP) reaction mechanisms were exhibited at the forward angles. At the backward angles the structure of the proton spectra were found to exhibit characteristics arising primarily from the QD reaction mechanism. This is an important feature not previously observed for photonuclear reactions on ^{12}C. The inclusive proton spectra are compared to the results of a QD model calculation for a photon energy of 212 MeV where the two nucleon absorption peak was not obscured by the proton detection threshold inherent for the charged particle detectors used in this measurement.

B.1 Introduction

In a recent review article [1] , the similarities and complimentarities of multi-nucleon emission following the absorption of real photons, virtual photons (in the case of electron scattering), and pions for energies in the region of the Δ-resonance have been discussed. Experimental data obtained using such probes are commonly explained in terms of quasifree reaction mechanisms. The description of nuclear interactions for complex nuclei in terms of quasifree reaction mechanisms has a long history dating back to early (p, p') experiments [2] (and references therein) in which a quasielastic scattering formalism [3] was used to describe the data with reasonable success. From these early quasielastic scattering experiments it was first determined that the Fermi momentum of the nucleons within the nucleus could be modeled using a Gaussian distribution [2]. The common prescription used to describe such quasifree reactions is to factorize the differential cross section into several parts. These are: the elementary

projectile-nucleon (or projectile-deuteron) cross section; a form factor describing the momentum density of the initial absorbing particle(s); and the kinematics. For the cases of the absorption of real photons, virtual photons (for reactions where the missing momentum is greater than the Fermi momentum) and pions, it is interesting to note that structure indicative of two nucleon absorption is evident at the high energy end of the inclusive proton spectra [1]. This leads to a description of the emission of such high energy nucleons via a two nucleon or QD absorption process for these boson probes.

The foundations for the photonuclear version of a factorized two nucleon absorption model were first studied in detail by Gottfried [4], who hypothesised that the disintegration of a complex nucleus, via a two nucleon absorption mechanism, could be described by

$$d\sigma = (2\pi)^{-4} F(P_{qd}) S_{fi} \delta(E_f - E_i) d^3k_n d^3k_p, \tag{B.1}$$

where $\boldsymbol{k}_p$ and $\boldsymbol{k}_n$ are the momenta of the outgoing proton and neutron respectively, $F(P_{qd})$ is a form factor proportional to the probability for finding a proton-neutron pair with zero separation and total momentum $P = |\boldsymbol{k}_n + \boldsymbol{k}_p - \boldsymbol{w}|$ in the Slater determinant, $\boldsymbol{w}$ is the incident photon momentum, and S_{fi} is the sum of the squares of the matrix elements evaluated in the center of momentum frame of the internal pn pair. As has been pointed out by Gottfried [4], the form factor $F(P_{qd})$ is a much more rapidly varying function of $\boldsymbol{P}_{qd}$ than is S_{fi}. S_{fi} is related to $\boldsymbol{P}_{qd}$ via the Doppler shift $w \rightarrow w_o$ where w_o is the photon energy in the center of momentum frame, defined by the internal (pn) pair. This shift is therefore determined by the initial momentum of the absorbing pair within the nucleus. The QD model is then obtained from Eq. (B.1) by replacing S_{fi} with the deuterium cross section evaluated in the in the center-of-mass frame of the two ejected nucleons. The additional factors necessary are the Levinger constant, L, which accounts for the fact that in the quasideuteron model the proton and neutron are much closer together than in the free deuteron case and the NZ/A factor which counts the number of possible proton-neutron pairs in the nucleus.

The underlying assumptions necessary to describe the (γ, pn) cross section in terms of the elementary deuterium photodisintegration cross section in the Gottfried factorized approximation have recently come under scrutiny by Ryckebusch et al. [5]. The first main premise in such a formalism is that the initial (pn) pair move in a relative $^1S_3$ state and this is known as the quasideuteron assumption. The second premise is the "zero-range" approximation for the radial dependence of the $l = 0$ relative (pn) wave function. Ryckebusch et al. show that the factorized form of the QD cross section overestimates their calculation, based on a Random Phase Approximation (RPA) approach, for the unfactorized two nucleon cross section (by as much as a factor of 2) for the photon energy range $E_\gamma = 50$ to 300 MeV. Ryckebusch et al. also comment that for photon energies above 200 MeV the effect of the zero-range approximation becomes small but nonnegligible. Furthermore, Ryckebusch et al. demonstrate that their full calculation for the photoabsorption on relative P waves for the (pn) pair in the unfactorized scheme is predicted to be significant for photon

energies up to 300 MeV.

The success of the QD model has also been questioned by Eden et al. [6], who show that the success of the QD model predicting the (γ, pn) angular correlation data, in the Gottfried factorized scheme, results from the dominance of the momentum density $F(P_{qd})$ of the initial (pn) pair, and does not require the photoabsorption matrix elements of the quasideuteron and the free deuteron to be similar. A similar observation was made in a more recent paper by Ryckebusch et al. [7]. These authors, using an unfactorized RPA calculation, demonstrate the dominance of the momentum dependence of the initial absorbing pair to the angular distribution of the ejected photonucleons. These results lead them to conclude that any two nucleon wave function will produce similar results for the angular distribution and they therefore suggest that comparisons between various calculations should be made on the basis of the total cross section. Contrary to the above findings, the angular distribution of emitted nucleons following the absorption of a charged pion has been shown to be dominated by the angular distribution of the free deuterium cross section used in this factorized QD calculation [8]. In this factorized DWIA QD calculation, used to explain the high energy exclusive and inclusive proton data, Mack et al. [8] comment that the similarity of the kinematical dependence of the two nucleon pion absorption process on complex nuclei, is contained in the elementary $\pi^+ d \rightarrow pp$ cross section, while the dependence of the amplitudes $T_{AB}^{L\Lambda}$ (influencing the angular distribution of the QD cross section) is dominated by the recoil momentum or equivalently $\phi_{L\Lambda}$, which is a microscopic form factor representing the center of mass motion of the $^1S_3$ QD within the nucleus. Apparently, the assumptions made in this calculation make the results more sensitive to the two nucleon wave function in contrast to the results of the photonuclear QD [6] and the RPA [7] formalisms. The results of the present measurement will be used to address the above ambiguities in the momentum dependence of the absorbing (pn) pair dominating the angular distribution of ejected photonucleons, as well as to make a comparison of the total two nucleon absorption strength for the various models described above.

B.2 EXPERIMENT

B.2.1 Experimental setup

The inclusive $^{12}C(\gamma, p)X$ measurement reported on in this paper was carried out using the tagged photon facility at the Saskatchewan Accelerator Laboratory (SAL). A 16 channel prototype of the currently implemented 62 channel photon tagger focal plane [9] was used for this measurement. Four proton detector telescopes of ΔE-E design were placed around a ladder containing a reactor grade carbon target and a 96% deuterated CD_2 target (used primarily for the energy calibration of the telescopes). The detectors were located at the laboratory angles of 51°, 81°, 109° and 140° at a fixed distance of 0.3 m from the center of the target to the front face of each collimated

detector. The targets were oriented with respect to the incident photon beam so as to minimize the energy loss of the produced photoprotons exiting the target material as viewed by the most backward detection angle. Approximately 60 hours of beam time were used for the data taking on the carbon target while another 20 hours were used for energy calibration (CD_2 target), tagging efficiency and target-out measurements.

B.2.2 Photon beam

The extraction of the electron beam from the pulse stretcher ring (PSR) produced an approximately 25% duty factor cw beam, which allowed tagging rates of 10^7 photons/second. The monochromatic electrons extracted from the PSR were incident on a thin aluminum radiator (.001 radiation lengths). The electrons, which underwent a bremsstrahlung interaction in the radiator and were within the momentum acceptance of the tagging spectrometer, were detected in the tagger focal plane detector. Electrons which did not undergo the bremsstrahlung process were directed via a dump magnet to a well removed and shielded beam dump. A coincidence between an electron in the focal plane and a proton in one of the telescopes was due to production of a photon with energy

$$E_\gamma = E_e - E'_e, \tag{B.2}$$

where E_γ is the energy of the tagged photon, E_e is the incident electron energy and E'_e is the energy of the bremsstrahlung electron detected in the focal plane. The tagged photon energy range was from 177 to 217 MeV. The 16 focal plane detectors were binned in groups of four corresponding to approximately 10 MeV photon energy bins so that improved statistical accuracy of the data was obtained.

There was a flight path of approximately 5 m between the radiator and target ladder. A 20 mm collimator was located 1 m before the target ladder to ensure a well defined beam spot on the target. The tagging efficiency for each channel of the spectrometer (defined as the ratio of the number of photons incident on the target to the number of electrons detected in that focal plane detector) was measured periodically during the course of the experiment. The photon flux was corrected for the tagging efficiency (typically about 80%) to obtain the absolute number of photons incident on the target.

B.2.3 Detectors, electronics and data acquisition

Each proton telescope consisted of a ΔE (energy loss) plastic scintillator of dimensions 100 mm by 100 mm and a thickness of 6.4 mm which was backed by a plastic scintillator serving as an E detector of the same area acceptance with a length of 360 mm. For the photon energies used in this measurement, the detectors were collimated such that all protons were stopped by the E detector. The electronics consisted of fast NIM and CAMAC instrumentation. The configuration of the data collection electronics was similar to that employed for most tagged photon spectrometers, with each of the 16 channels of the focal plane having its own TDC. Each ΔE and E detector was charge integrated by an ADC and had the timing information recorded with

a TDC. The logic for identification of a detected event was as follows: any proton detector displaying a three-fold coincidence (ΔE, E, and their sum greater than a preset discriminator level), which in turn was in coincidence with an electron event in the tagging focal plane, caused a TDC to be started by the electron event. The TDC was then stopped by the proton signal (which had a sufficient predetermined delay) giving a time distribution of valid coincident events. Data were recorded on an event-mode basis and written to tape for off-line analysis. However, the data acquisition system at SAL allowed a subset of the acquired data to be displayed in real time in histogram and scatter plot formats to allow continuous monitoring of the data taken to ensure the electronics and other experimental parameters were performing as expected.

B.3 DATA REDUCTION

The particle identification was performed via a scatter plot of the energy deposited in the ΔE detector versus that deposited in the E detector. Excellent separation of particle bands (deuterons, protons, pions and electrons) was obtained. Energy calibration of the proton telescopes was performed by locating the two-body final state peak (corresponding to the photodisintegration of the deuteron) in the energy spectra with the CD_2 data. A coincidence between the tagger focal plane and any proton telescope trigger produced a coincidence peak in the 36 ns wide coincidence resolving time distribution. Corrections were made to each of the 16 time distributions to subtract the random background underlying the coincidence peak. The accuracy of this subtraction was enhanced by a correction for the different times-of-flight for protons of different energies. This reduced the coincident timing peak to about 1.8ns FWHM. A typical coincidence peak is shown in Fig. 1. The proton yield spectra were grouped into kinetic energy bins of T_p = 10 MeV. Corrections to the solid angle subtended by each detector, due to the extended target, were made and found not to exceed 2%. Proton energy loss in the thin target, in the air in the flight path and in the ΔE detector was corrected for. The target-out background (no greater than 2% per proton energy bin) was subtracted from the target-in data to give the absolute yield of target protons.

The double differential cross section for the inclusive $^{12}C(\gamma, p)X$ reaction for each photon energy bin and laboratory detection angle was determined using the relation

$$\frac{d^2\sigma}{dE_p d\Omega_p} = \frac{Y_p}{exp(\tau_c N_e) N_\gamma d\Omega_p \varepsilon_{tag} N_T dT_p} \tag{B.3}$$

where Y_p was the absolute yield of protons emitted into solid angle $d\Omega_p$ subtended by the detector, dT_p was the proton kinetic energy bin width, N_γ was the expected number of photons incident on the target of N_T nuclei per cm^2 and ε_{tag} was the tagging efficiency. The term $exp(-\tau_c N_e)$, where N_e was the number of correlated electrons detected in the tagging focal plane and τ_c was the location of the prompt peak indicating a correlated electron photon event had occurred, was the stolen count

correction [10] to the incident photon flux. The net systematic error for the proton spectra resulting from Eq. (B.3) is estimated to be 12%.

B.4 RESULTS AND DISCUSSION

B.4.1 Deuterium total cross sections

The total cross sections for deuterium were extracted from the energy calibration data after a suitable subtraction of the proton yield from ^{12}C in the CD_2 target was performed. To increase the statistical accuracy, the photon energy bin size was chosen to be 20 MeV. A typical proton yield spectrum, for one of the four detection angles, is shown in Fig. 2. The deuterium angular distributions were fit with a Legendre polynomial expansion to obtain the total cross sections. The results are shown in Fig. 3 with other existing monochromatic photon data. This figure serves two main purposes. First, the good agreement with the existing data indicates no large systematic errors in the current measurement. Second, it shows that the photon energy region studied in this measurement was in the so-called "dip" region between the GDR and the low photon energy side of the delta resonance. For this photon energy region the QD reaction mechanism is expected to dominate the photoabsorption process.

B.4.2 Carbon double differential cross sections

B.4.3 Proton kinetic energy spectra

The proton kinetic energy spectra resulting from Eq. (3) are shown in Figures 4 to 7. The highest photon energy bin can be compared to the results of Ref. [14] for a similar photon energy and detection angles. At the angles of 51° and 141°, the present measurement is about a factor of two smaller in magnitude at the location expected for the QD peak. At the detector angles of 81° and 109°, the magnitude of the QD peaks are in better agreement, the present data being the smaller of the two measurements by approximately 20% to 30%. In the current measurement, the sharp change in the slope of the proton energy spectrum, for $E_\gamma = 212$ MeV and $\theta_p = 51°$, at $T_p = 35$ MeV indicates the presence of protons resulting from the QFPP reaction mechanism.

The inclusive $^{12}C(\gamma, p)X$ measurement for $E_\gamma = 200$ MeV has also been performed by the FRASCATI group [15]. The proton energy spectra were obtained by annihilation γ rays after a bremsstrahlung subtraction which produced a monochromatic photon yield. The magnitude of the cross sections at the location of the QD peak are in reasonable agreement at all angles with the current data set. However, in this data set, there exists a steep increase in the cross sections at all detection angles for low proton energies which has a marked bremsstrahlung shape. This is also present in their 160 MeV photon energy data set and therefore cannot be primarily (satisfactorily) attributed to recoil protons resulting from the QFPP reaction mechanism.

B.4.4 Proton momentum spectra

According to Eq. (B.1), the elementary cross section is expected to be modulated by the Fermi momentum of the QD within the nucleus. Therefore, structure resulting from the internal motion of the QD should become more evident if the proton spectra are plotted as a function of momentum rather than the kinetic energy. The resulting cross sections were obtained by the following transformation

$$\frac{d^2\sigma}{dP_p d\Omega_p} = \frac{d^2\sigma}{dT_p d\Omega_p}\frac{dT_p}{dP_p}, \tag{B.4}$$

where

$$\frac{dT_p}{dP_p} = \frac{P_p c^2}{m_p c^2 + T_p}, \tag{B.5}$$

and where T_p is the proton kinetic energy, P_p is the corresponding proton momentum, and m_p is the rest mass of the proton.

The proton momentum spectra resulting from the transformation defined by Equations (B.4) and (B.5) are shown in Fig. 8 for E_γ = 212 MeV. An important feature displayed by the current data set is structure in the proton spectra indicative of two nucleon absorption at the backward angles. This structure had not been observed in the previous inclusive photonuclear measurements [14, 15]. The height of the upward pointing arrows in Fig. 8 is proportional to the d(γ,p)n laboratory cross section for E_γ = 208 MeV [16] when normalized to the data at 51°. The agreement between the scale of the free deuterium cross sections to the height of the high momentum peaks in the inclusive proton spectra, supports the dominance of the two nucleon absorption mechanism for producing these structures.

In the previous measurements [17, 18, 19, 20, 21, 22, 23], the systematics of the QFPP and QD reaction mechanisms have been studied for the forward angles by the analysis of the inclusive proton spectra. In Fig. 8 the small downward arrows indicate the proton momentum expected from the free deuterium kinematics for E_γ = 212 MeV. From this figure it can be seen that for the proton angle of 51°, the quasifree peak in the proton spectrum is found to occur about 35 MeV/c below the momentum expected from the free deuterium kinematics. This value is consistent with that reported in the previous measurements. However, the shifting of the quasifree peak to lower momentum is found to increase to about 55 MeV/c for θ_p = 141°. A significant background is expected to be present in the QD structure observed in an inclusive measurement. For the photon energy range studied in the present measurement, the typical energies of the nucleons ejected via the two nucleon absorption mechanism should primarily undergo (N,2N) rescattering leading to 4 or more particles in the final state. Intuitively, it seems obvious that the background under the QD peaks in the inclusive proton spectra should increase as the detection angle increases. This is a result of the larger phase space available for the rescattered protons due to the kinematical shift of the QD peak to lower energies as the detection angle increases. Furthermore, consistent with the above argument, one would expect that at any given

angle the background should decrease as the proton energy increases. The net effect of such a phase space background would be to push the apparent QD peaks in the proton spectra to higher energies. A background which would cause the QD peaks to shift to a lower proton energy seems contrary to a phase space domination of the background in the inclusive proton spectra.

Support for the shifting seen in the current quasifree structure comes from the early proton quasielastic scattering data on ^{12}C [2]. Here it was observed that the quasifree peaks were shifted to lower proton energies than expected for the free elastic (p,p) scattering kinematics, and that the magnitude of this shift was seen to increase as the detection angle increased. This shifting of the quasifree peaks as a function of the detection angle was thought to be sensitive to the real part of the nuclear potential.

As previously mentioned, in the inclusive ^{12}C measurement [14], structure was not observed at the backward detection angles. In that measurement a QD model prediction, in the form of an intranuclear cascade calculation [24] (PICA computer code), was used to fit the data. The results of the code for a photon energy similar to those studied in the current measurement are shown with their data at backward proton angles with and without the inclusion of FSI. With the inclusion of FSI, the calculation predicts that the proton spectra will decrease monatomically as the proton energy increases. This, however, is inconsistent with the present measurement, which shows structure at the backward angles consistent with QD kinematics. The present data set would agree well with the shape of the cross section predicted by PICA without the inclusion of such FSI. The structure in the proton spectra observed in the current measurement is also supported by the recent $^{16}O(\pi^+, 2p)^{14}N$ measurement [8], where the incident pion kinetic energy was T_π = 115 MeV. Here also, structure exhibiting characteristics of two nucleon absorption was observed at all detection angles for the inclusive proton spectra. The two measurements are consistent, since the FSI of the ejected protons are expected to be similar for both reactions.

B.5 Comparison with the quasideuteron model calculation

The results of the inclusive ^{12}C(γ,p)X proton momentum spectra are compared to the results of the quasideuteron model calculation of Ref. [6]. The code predicts the inclusive (γ,p) double differential cross section to be the sum of all possible couplings of the initial states of the quasideuteron resulting in the emission of a pn pair from orbitals $(nlj, n'l'j')$, and is given by

$$\frac{d^2\sigma_{qd}}{dT_p d\Omega_p}\Big|_{nlj;n'l'j'} = c' L \frac{N_{nlj} Z_{n'l'j'}}{A} \int F_{nl;n'l'}(P_{qd}) \left\{ \frac{d\sigma_d(E'_\gamma, \theta''_p)}{d\Omega''_p} \delta_{T_p} J_p dP_{qd} \right\} \qquad \text{(B.6)}$$

where N_{nlj} is the number of neutrons and $Z_{n'l'\ j'}$ is the number of protons in their respective orbitals, A represents the number of nucleons in the target nucleus, L is the Levinger constant, $F_{nln'l'}(P_{qd})$ is the unit-normalized momentum density for a quasideuteron formed from a neutron and a proton in their respective orbitals,

$d\sigma_d(E_\gamma', \theta_p'')\ /d\Omega_p''$ is the deuteron cross section which is evaluated in the center-of-momentum (c.m.) frame defined by the absorbing proton-neutron pair, E_γ' is the photon energy which has been Doppler shifted into the frame where the quasideuteron is at rest, θ_p'' is the angle between the photon and the proton momenta evaluated in the c.m. frame, J_p represents the product of the Jacobians necessary for the coordinate transformations, and c' is a normalization constant which ensures that

$$\sigma_{qd} = L\frac{NZ}{A}\sigma_d. \tag{B.7}$$

Eq. (B.7) has the same form as the original QD model proposed by Levinger [25]. The value for the harmonic oscillator parameter used in the present QD model calculation was α = 120 MeV/c as was given in Ref. [26]. This value was able to reproduce the root-mean-square charge radius of 2.50 fm for ^{12}C, as has been determined from electron scattering experiments. For further information on the QD model calculation used, the reader is referred to Ref. [6].

The sum over the bound-state orbits in Eq. (B.6) was corrected for the effects of FSI, expected to cause strong attenuation of protons from the initial QD reaction channel, using the following equation

$$\frac{d^2\sigma_{qd}}{dT_p d\Omega_p} = \sum_{nlj;n'l'j'} \eta_{nl}(T_p)\left\{\frac{d^2\sigma_{qd}}{dT_p d\Omega_p}\Big|_{nlj;n'l'j'}\right\} \tag{B.8}$$

where the transparency, η_{nl}, for a proton ejected from the (nl) orbital is given by

$$\eta_{nl}(T_p) = \frac{\int \rho_{nl}(r) exp(-\sigma_{nn'}(T_p)\int_{t=0}^{\infty}\rho_A(r'(t))dt)d^3r}{\int \rho_{nl}(r)d^3r}. \tag{B.9}$$

Here, ρ_{nl}(r) is the density of nucleons at a distance r from the center of the nucleus for the harmonic oscillator shell (nl). The reaction cross section, $\sigma_{nn'}(T_p)$, for a proton with kinetic energy T_p interacting with the spectator (A-2) nucleons was unavailable and was therefore approximated by the ^{9}Be proton reaction cross section [27] appropriately scaled to simulate that expected for ^{10}Be. The location of the photoabsorption site is defined to originate at the position (r,θ,ϕ) within the nucleus and be directed towards the detector. To account for the fact that the nuclear density is not constant as a function of the radius, the term $\rho_A(r'(t))$ giving the density at the position t along the escape trajectory was used. The results for the transparency calculations resulting from Eq.(B.9) for the harmonic oscillator shells of ^{12}C are shown in Fig. 9. The advantages of this FSI correction over the other previous phenomenological calculations has been discussed in Ref. [6]. It is worth mentioning here that the present proton transparency is in reasonable agreement (to within 10% for all proton energies) with the more accepted optical model calculation [28].

The effect of FSI of photoproduced pions has not been addressed in this paper. However, it can be demonstrated to be a small effect for protons ejected by the

pion absorption QD reaction mechanism. The dominant pion FSI mechanism for the production of high energy protons , which could result in background in the proton spectra at the location of the QD peak, results from the π^++"d" $\rightarrow$ pp quasifree reaction [8, 29, 30]. It is known [31, 32] that inclusive π^+ photoproduction cross sections are typically about an order of magnitude less than inclusive photoproton cross sections [14] for the photon energy range currently studied. In addition to the lower pion cross section it should be noted that the transparency for the "true" absorption for 60 MeV π^+ (typical pion energies encounter at these photon energies) is of the order of 0.9-0.95 [28]. Therefore, it is expected that the contribution of high energy protons resulting from FSI of the photoproduced pions should be a small effect.

Previously [6, 26], the scale of the QD model calculation was set by normalizing the results of the calculation to the backward detection angle of the inclusive proton spectra where contributions from the direct (γ,p) reaction are suppressed. As a kinematical remark it should be noted that recoil protons from the QFPP mechanism are kinematically forbidden for the photon energy range and the backward angles studied in the current measurement, so that a similar normalization of the QD calculation as discussed above may seem appropriate. However, due to the predicted strong attenuation of protons demonstrated in Fig. 9 and the unknown multinucleon phase space expected in the proton spectra, this procedure seemed inappropriate for the current analysis. Instead, the results of a reworking of Levinger's original QD calculation [25] recently undertaken [33] were used in the present calculation. The authors use the current world data set for the root-mean-square charge radius for elements throughout the periodic table. This enables the evaluation of the Levinger constant, which is proportional to $A^{1/3}/\langle r^2\rangle^{1/2}$, to be calculated in the spirit of Levinger's original model and not in a phenomenological fitting to the data. It was thought a good test for this calculation to let the value for the absolute scale of the current QD model calculation be set by their prediction. For this reason the Levinger value was chosen to be L = 4.9 which results from their global parameterized fit to the whole of the data set. For the present calculation the required normalization of Eq. (B.6), when summed over all possible couplings, with respect to the requirement of Eq.(B.7) was obtained by setting $c' = 1.27$.

The results of the current QD model calculation, including the effects of FSI with respect to the attenuation of the protons from the initial QD reaction channel, are shown by the solid curves in Fig. 8. Also shown in Fig. 8 (dashed curves) is the current QD model calculation when an isotropic angular distribution is used for the deuteron cross section. The scale was chosen so that the strength of the two cross sections were equal for $\theta_p = 141°$. The dominance of the form factor $F(P_{qd})$ on the predicted angular distribution in the QD model is clearly observed by the near equal prediction in the scale of the cross section at the other three proton angles. The fact that the Gottfried factorized calculation is quite insensitive to the form of the two nucleon wave function assumed led Eden et al. [6] to question the physical significance of the Levinger constant. However, contrary to the prediction of the

present QD calculation the data do not reflect the dominance of F(P_{qd}) governing the angular distribution. It is seen that the calculation increasingly underpredicts the measured cross section as the proton angle decreases. This difference cannot be explained with what one would intuitively expect for the simple phase space model described earlier or with the phase space background inferred from the exclusive $^{16}O(\pi^+, 2p)^{14}N$ measurement [8]. As a final note, a strikingly similar result is seen when the unfactorized RPA calculations of Ryckebusch et al. [34] are compared to the angular distribution of protons from ^{12}C at E_γ = 151 MeV.

The QD model calculations shown in Fig. 8 were integrated over the entire proton energy range (with and without the inclusion of FSI) and the results are given in Table 1. The subscript "NET" on the differential cross sections in Table 1 refers to the total yield of protons expected to result from the two nucleon absorption mechanism in the absence of FSI. Also presented for comparison is the measured cross section integrated to the detector threshold. It is worth noting that the scale of the cross section is decreased by about a factor of 2, while the angular dependence is not significantly influenced by the present FSI correction. The angular distribution resulting from the QD model calculation, presented in Table 1, is relatively flat and does not resemble the strongly forward peaked cross section for the deuteron in the laboratory system. This again reflects the strong influence of F(P_{qd}) on the angular distribution in the Gottfried factorized scheme. The apparent result of such calculations where the trend of the angular distribution is set by the form factor F(P_{qd}) is that it should predict virtually the same angular distribution for both protons and neutrons as demonstrated in Fig. 8. This rather flat prediction for the angular distribution is well fit by the inclusive neutron spectra from Ref. [35] and explains the apparent good agreement between the Gottfried factorized calculation and previous neutron measurements.

The total cross sections for the measured proton spectra and the QD calculation (with and without the effects of FSI) were obtained by using a Legendre polynomial fit to angular distributions and are given at the bottom of Table 1. The net two nucleon absorption strength for the current calculation is given by Levinger's original formula [Eq. (B.7)] and is equal to 0.825 mb. Despite the disagreement of the present QD model calculation with the current data set, for completeness the net two nucleon absorption strength predicted by the current calculation can be compared with the results of existing calculations for the same photon energy. The approximately 1.0 mb predictions of Laget [28] using a QD model based on a meson exchange formula agrees quite favorably with the current prediction. The rigorous microscopic calculations of Carrasco and Oset [36], which are based on an understanding of the photon self-energy in nuclear matter, predict a total absorption cross section of approximately 0.96 mb with an uncertainty of 10%. This result also agrees reasonably well with the QD model calculations. However, the current predicted scale is nearly a factor of 3 larger than the approximately 0.28 mb prediction from the RPA calculation of Ryckebusch et al. [7] using a RPA calculation. However Ryckebusch et al. state that there exists a 50% error in the absolute scale of the cross sections predicted by this RPA calculation.

Table B.1: Comparison of the measured inclusive $^{12}C(\gamma,p)X$ cross sections for E_γ = 212 ± 5 MeV with the current QD calculation with and without the effects of FSI. The measured cross sections have been integrated to the detector threshold while the calculated QD cross sections have been extrapolated below the detector threshold.

θ_p (deg)	$d\sigma/d\Omega)_{THRES.}$ (μb/sr)	$d\sigma/d\Omega)_{NET}$ (μb/sr)	$d\sigma/d\Omega)_{FSI}$ (μb/sr)
51	106.58 ±1.02	63.2	33.8
81	84.57 ±0.83	70.4	34.8
109	54.49 ±0.65	69.8	31.6
141	31.65 ±0.53	65.5	28.65
σ_{TOT}	925.25 ±5.33	825	405

From the current data set the structure in the proton spectra and the apparent scaling of the peak in the measured differential cross sections with the free deuterium cross sections leads one to question the assumption(s) that make the Gottfried factorization insensitive to the two nucleon cross section used. Gottfried also had questioned two of the main premises for the QD case of his factorized hypothesis. First, Gottfried questioned whether the matrix elements contained in S_{fi} can be computed from deuterium cross section. Second, he questioned if these matrix elements depend on the Doppler shift of the photon to the rest frame of the absorbing QD. In particular, as the value of $F(P_{qd})$ increases the deuterium cross section used in Eq. (B.6) becomes further off-shell, with the minimum off-shell value obtained when $F(P_{qd})$ = 0. One important point concerning the validity of applying Eq. (B.2) [and therefore Eq. (B.6)] to the present data is that Eq. (B.2) holds its exact stated form only for closed-shell nuclei. However, Gottfried justified the comparison of his theory with ^{12}C data since, as in the present comparison, the integration over the undetected neutron energy has been performed. One of the most noteworthy differences between the pion absorption and photonuclear QD models is that the originally off-shell elementary $\pi^+ d \rightarrow pp$ cross section, in the pion absorption formalism, is taken to be on-shell [8, 29, 30] by the so-called final energy prescription as determined by the two detected protons. This seems to allow the pion absorption calculation to be sensitive to the two nucleon wave function assumed, and was found to reproduce the angular distribution of their data with the strong angular dependence of the inclusive proton spectrum bearing a close resemblance to the elementary $\pi^+ d \rightarrow pp$ cross section.

B.5.1 Conclusions

Inclusive proton energy spectra have been measured for a photon energy range E_γ = 177 to 217 MeV for the proton detection angles θ_p = 51°, 81°, 109° and 141°. The inclusive proton momenta spectra were compared to the results of a QD model

calculation for the photon energies 212 ± 4.5 MeV. Although the Gottfried factorized model gives a relatively good account of the total strength expected for the two nucleon absorption strength it fails to reproduce the angular distribution of the current data set. This is taken to be evidence that the form factor $F(P_{qd})$ does not dominate the current measurement of the angular distribution of protons ejected from the QD reaction mechanism as is predicted by the Gottfried factorized hypothesis. The Levinger constant was set at L = 4.9 as predicted by a recent calculation. The agreement between the scale of the calculation (set by L) compared to the present data set is strongly model dependent on the FSI correction used. However, owing to the disagreement of the present calculation with the angular distribution of the current data set it is not possible to reach a sound conclusion on the absolute scale of the two nucleon cross section. A high resolution measurement of the exclusive photonuclear QD reaction mechanism is needed to gain further insight to the physics involved in the two-nucleon absorption mechanism. A similar analysis to that of the quoted pion absorption measurements seems the only possible way to remove the ambiguities inherent in the interpretation of single arm proton data.

ACKNOWLEDGMENTS

The authors wish to acknowledge the support of the Natural Sciences and Engineering Research Council of Canada and the dedicated work of the staff at the Saskatchewan Accelerator Laboratory. We also wish to thank to J. Eden for providing the QD model source codes, and S. Karataglidis for completing the modifications required for the present analysis.

References

[1] T. S. Bauer, Nucl. Phys. **A546**, 181c (1992).

[2] J. B. Cladis, W. H. Hess and B. J. Moyer, Phys. Rev. **87**, 425 (1952).

[3] P. A. Wolff, Phys. Rev. **87**, 434 (1952).

[4] K. Gottfried, Nucl. Phys. **5**, 557 (1958).

[5] J. Ryckebusch, L. Machenil, M. Vanderhaeghen and M. Waroquie, Phys. Lett. **B291**, 213 (1992).

[6] J. A. Eden et al., Phys. Rev. **C44**, 753 (1991).

[7] J. Ryckebusch, L. Machenil, M. Vanderhaeghen and M. Waroquie, Nucl. Phys. **A568**, 828 (1994).

[8] D. J. Mack et al., Phys. Rev. **C45**, 1767 (1992).

[9] J. M. Vogt, R. E. Pywell, D. M. Skopik, E. L. Hallin, J. C. Bergstrom, H. S. Caplan, K. I. Blomqvist, W. DelBianco and J. W. Jury, Nucl. Instrum. Methods **A324**, 198 (1993).

[10] R. Owens, Nucl. Instrum. Methods **A288**, 575 (1990).

[11] E. De Sanctis et al., Phys. Rev. **C34**, 413 (1986).

[12] J. Arends, H. J. Gassen, A. Hegerath, B. Mecking, G. Noldeke, P. Prenzel, T. Reichelt and A. Voswinkel, Nucl. Phys. **A412**, 509 (1984).

[13] A. M. Sandorfi, Private Communication (1991).

[14] J. Arends, J. Eyink, H. Hartmann, A. Hegerath, B. Mecking, G. Noldeke and H. Rost, Z. Phys. **A298**, 103 (1980).

[15] Perspectives in Nuclear Physics at Intermediate Energies, Edited by S. Boffi, C. Ciofodegli Atti and M. M. Giannini, copyright 1985 by World Scientific Publishing Co. pg 390.

[16] K. Garrow, M.Sc. thesis, Queen's University (1991), SAL report No. 40 (unpublished).

[17] S. Homma, M. Kanazawa, K. Maruyama, Y. Murata, H. Okuno, A. Sasaki and T. Taniguchi, Phys. Rev. Lett. **45**, 706 (1980).

[18] S. Homma, M. Kanazawa, K. Maruyama, Y. Murata, H. Okuno, A. Sasaki and T. Taniguchi, Phys. Rev. **C27**, 31 (1983).

[19] S. Homma et al., Phys, Rev. Lett. **53**, 2536 (1984).

[20] S. Homma et al., Nucl. Phys. **A446**, 241c (1985).

[21] M. Kanazawa, S. Homma, M. Koike, H. Okuno, F. Soga, N. Yoshikawa and A. Sasaki, Phys. Rev. **C35**, 1828 (1987).

[22] S. Homma et al., Phys. Rev. **C36**, 1623 (1987).

[23] Proceedings of the Workshop on Photonuclear Reactions using Continuous Electron Beams, edited by T. Terasawa, 88 (1989).

[24] T. Gabriel and R. Alsmiller, Phys. Rev. **182**, 1035 (1969).

[25] J. Levinger, Phys. Rev. **84**, 43 (1951) and Nuclear Photodisintegration, Oxford University Press, London (1960).

[26] H. Schier and B. Schoch, Nucl. Phys. **A229**, 93 (1974).

[27] P. U. Renberg, D. F. Mesday, M. Pipen, P. Schwaller, B. Favier and C. Richard-Serre, Nucl. Phys. **A183**, 81 (1972).

[28] J. M. Laget, New Vistas in Electro-Nuclear Physics, Edited by E. L. Tomusiak , H. S. Caplan and E. T. Dressler, copyright 1986 Plenum Press New York, pp 410 - 415.

[29] M. Steinacher et al., Nucl. Phys. **A517**, 413 (1990).

[30] R. A. Schumacher et al., Phys. Rev. **C38**, 2205 (1988).

[31] K. G. Fissum, Ph.D thesis, University of Saskatchewan (1993). and article to be published.

[32] J. Arends, J. Eyink, H. Hartmann, A. Hegerath, B. Mecking, G. Noldeke and H. Rost, Z. Phys. **A305**, 205 (1982).

[33] O. A. P. Tavers and M. L. Terranova, J. Nucl. Part. Phys. **G18**, 521 (1992).

[34] J. Ryckebusch, L. Machenil, M. Vanderhaeghen, V. Van der Sluys and M. Waroquie, Phys. Rev. **C49**, 2704 (1994).

[35] T. Emura et al., Phys. Rev. **C49**, 597 (1994).

[36] R. C. Carrasco and E. Oset, Nucl. Phys. **A536**, 445 (1992).

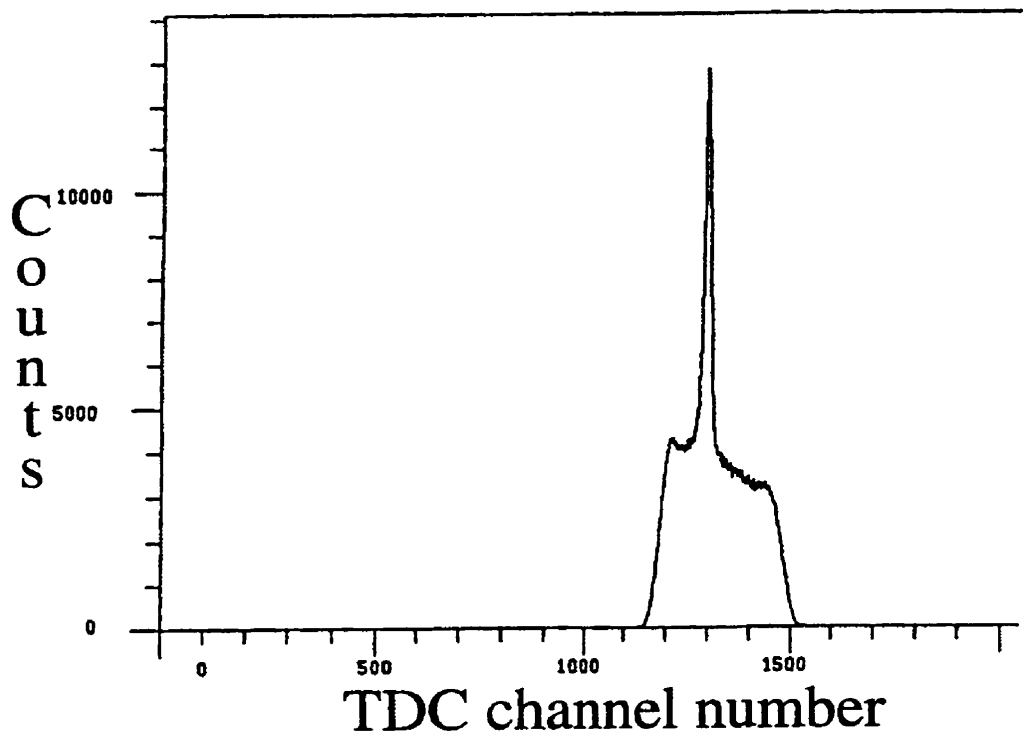

Figure B.1: A typical prompt peak (FWHM = 1.8 ns) resulting from a coincidence between the tagging focal plane and one of the proton telescopes.

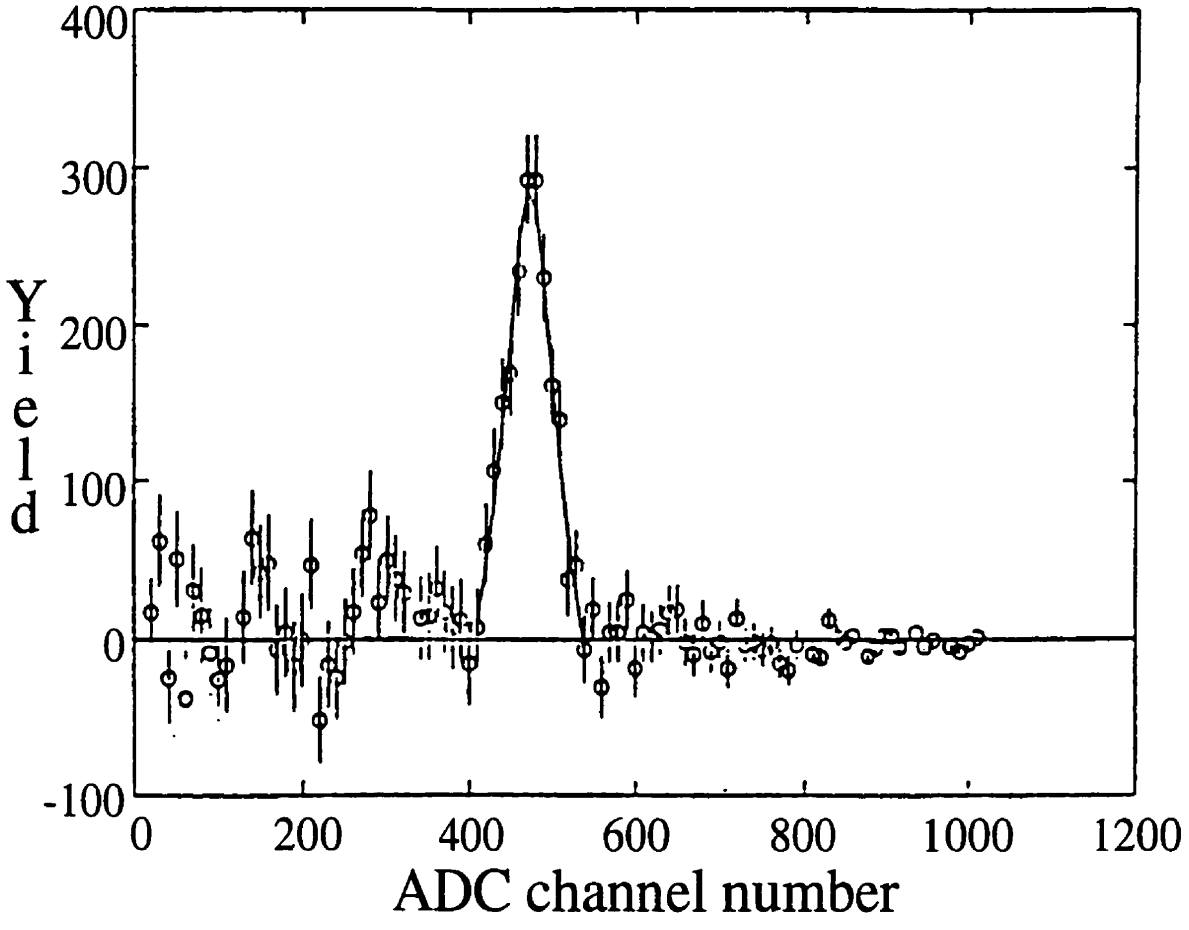

Figure B.2: A typical proton yield spectrum, used for both energy calibration and evaluation of the deuterium differential cross section, is shown.

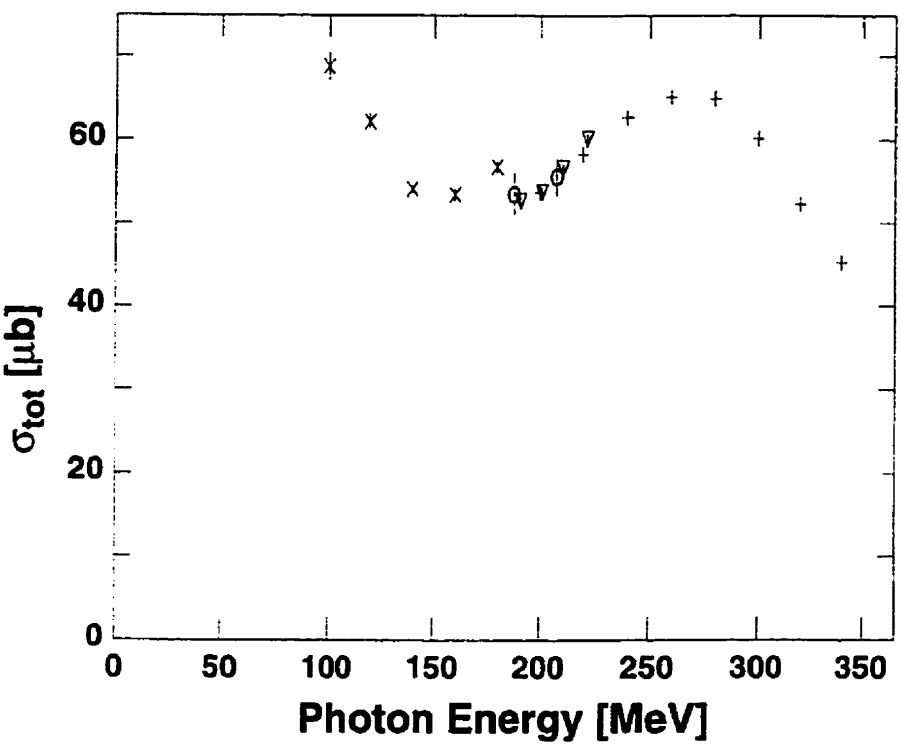

Figure B.3: Total cross sections for the D(γ, p) reaction as a function of the incident photon energy. The data are taken from: crosses Ref. [11], daggers Ref. [12], triangles Ref. [13], and the ovals are from the current measurement.

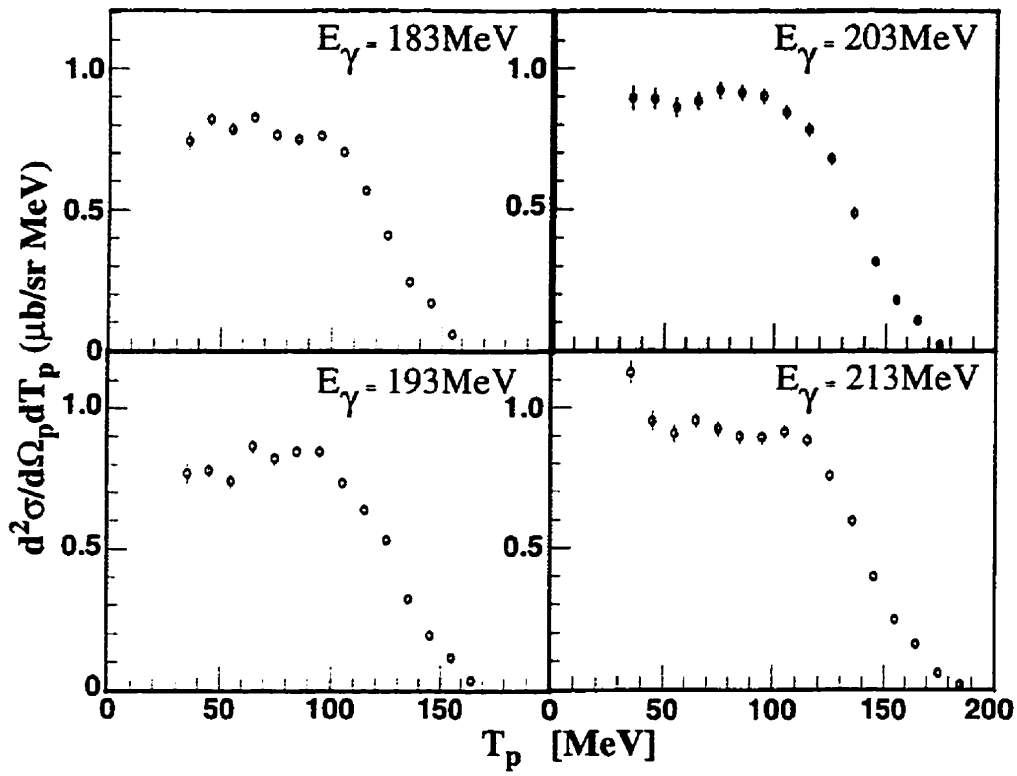

Figure B.4: Double differential cross sections for the reaction $^{12}C(\gamma,p)$ X for the photon energy range 177 to 217 MeV. The laboratory angle is $\theta_p = 51 \pm 7°$.

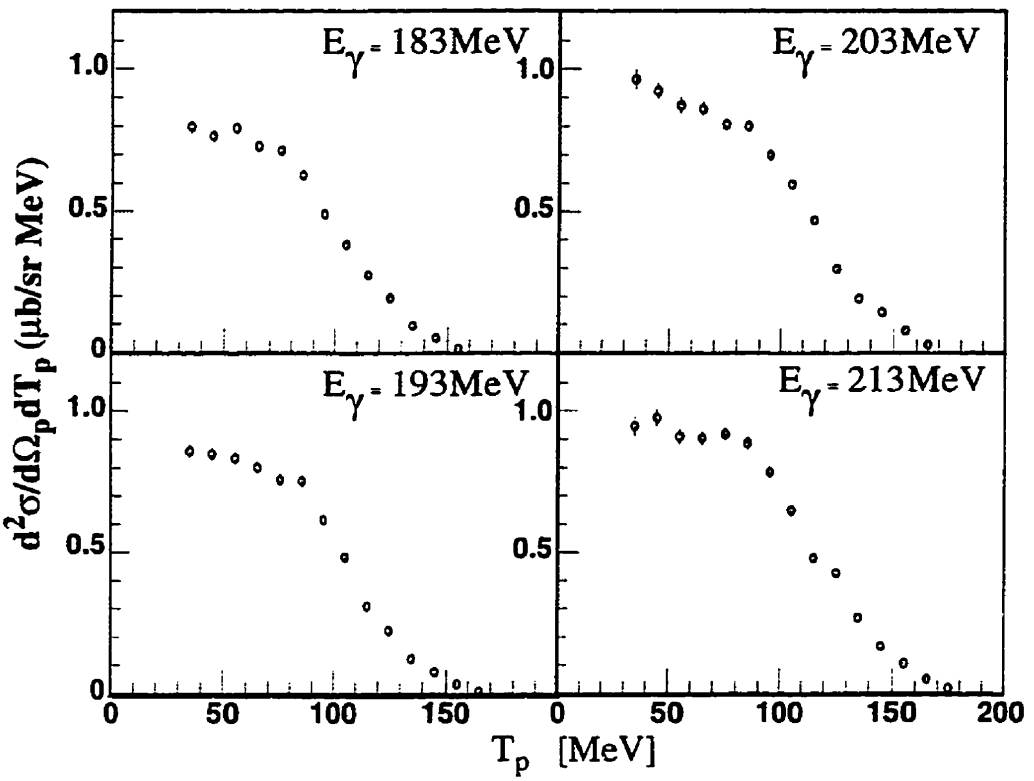

Figure B.5: Double differential cross sections for the reaction ^{12}C(γ,p) X for the photon energy range 177 to 217 MeV. The laboratory angle is $\theta_p = 81 \pm 7°$.

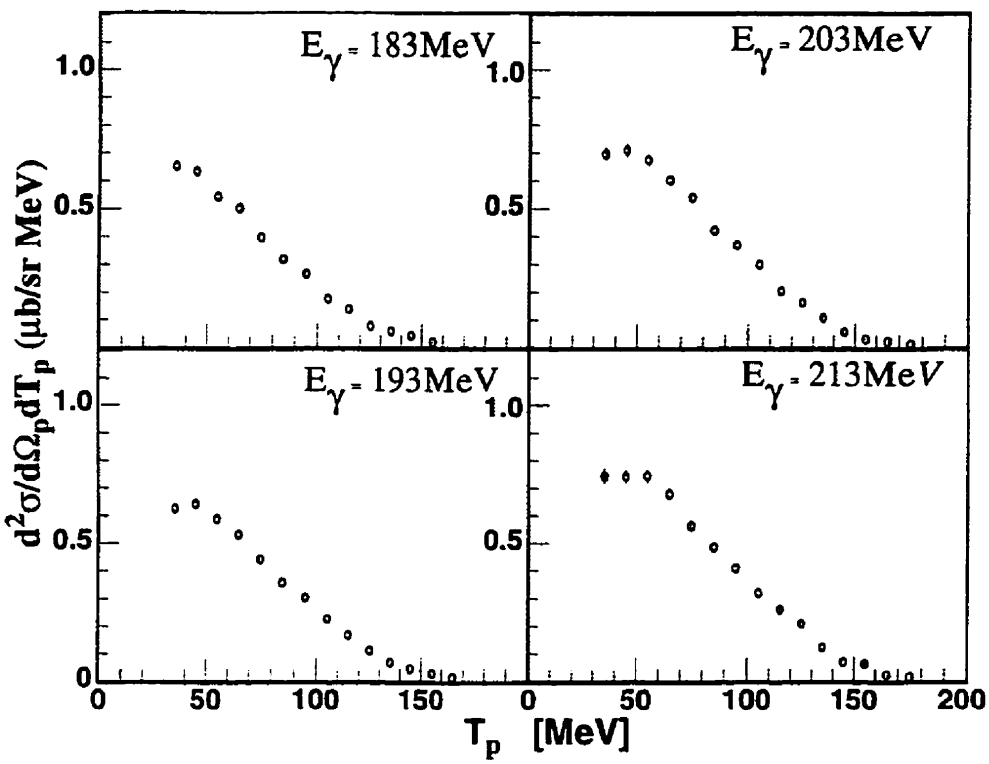

Figure B.6: Double differential cross sections for the reaction ^{12}C(γ,p) X for the photon energy range 177 to 217 MeV. The laboratory angle is $\theta_p = 109 \pm 7°$.

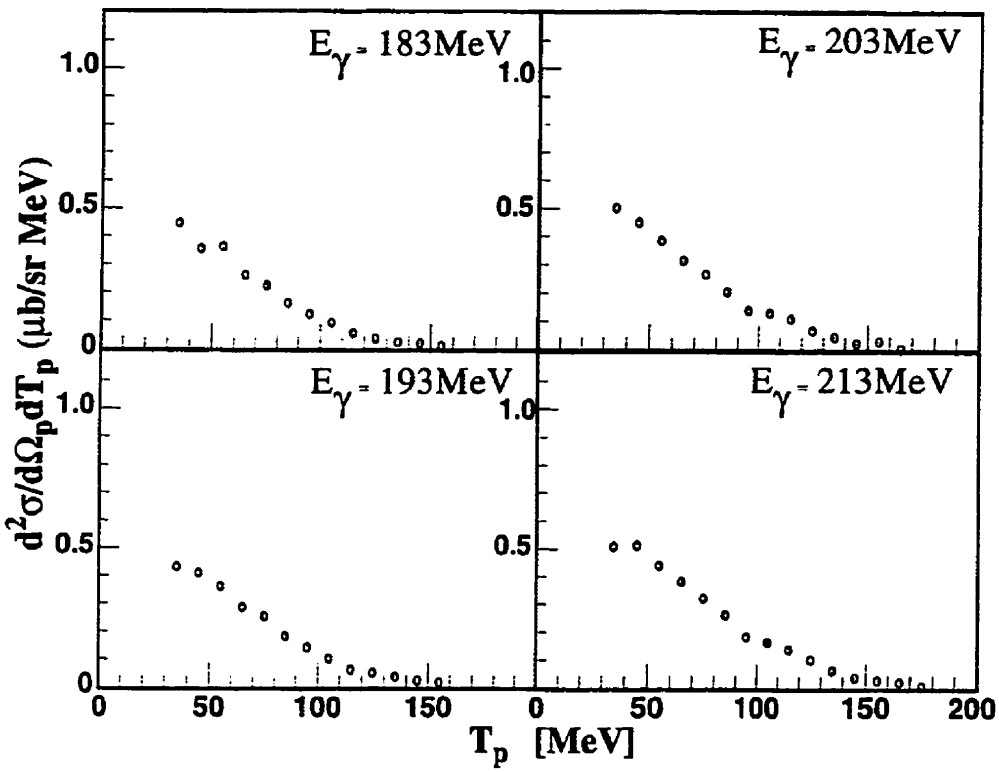

Figure B.7: Double differential cross sections for the reaction $^{12}C(\gamma,p)$ X for the photon energy range 177 to 217 MeV. The laboratory angle is $\theta_p = 141 \pm 7°$.

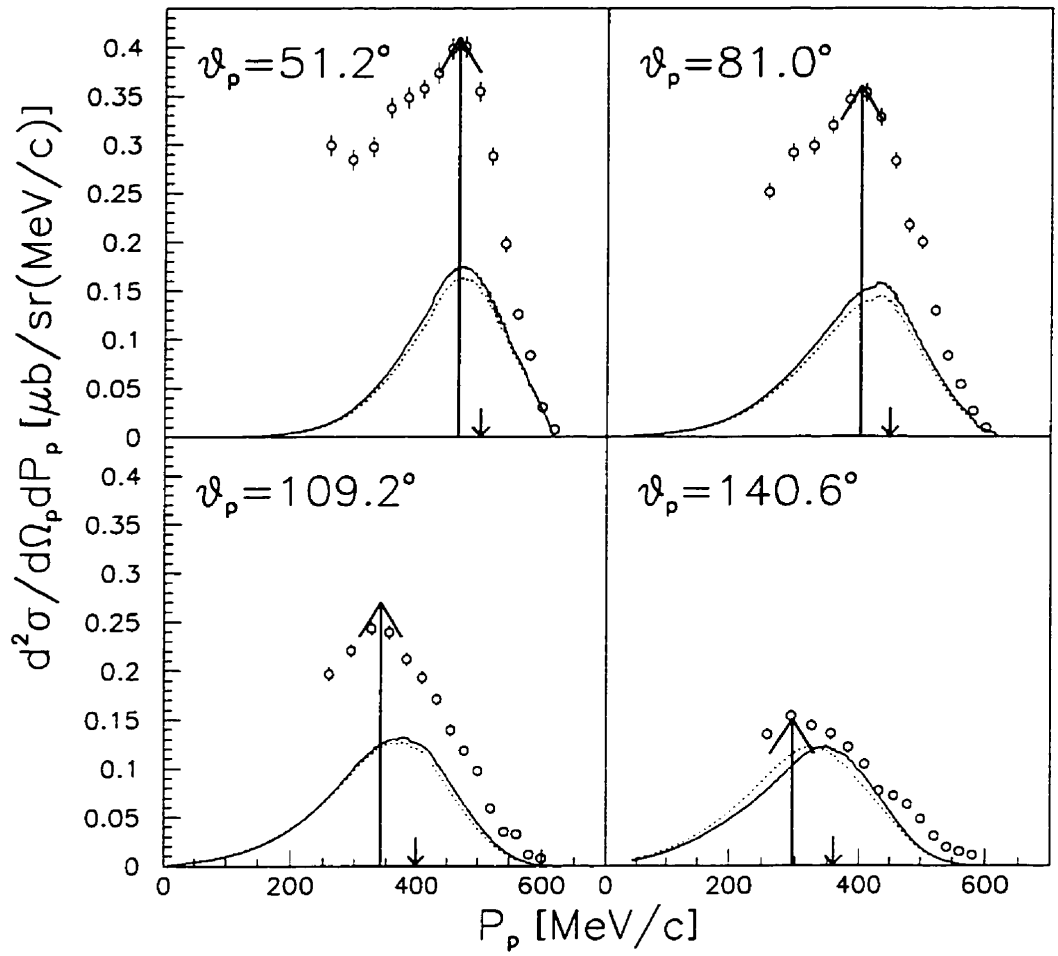

Figure B.8: Proton momentum spectra for the photon energy range 212.6 ± 4.5 MeV at all four proton detection angles. The solid curves in the figure are the results of the quasideuteron calculation of reference [6] when the real angular distribution for the deuteron was used. The dashed curves are the results of the same calculation when an isotropic angular distribution for the deuterium cross section was assumed. The normalization was such that at $\theta_p = 141°$ the two calculations predicted equal strength for the cross section. The height of the arrows in the figure are proportional to the d(γ, p)n laboratory cross section for $E_\gamma = 208$ MeV [16] when normalized at 51°. The small downward arrows represent the proton momentum required for the free deuterium photodisintegration kinematics.

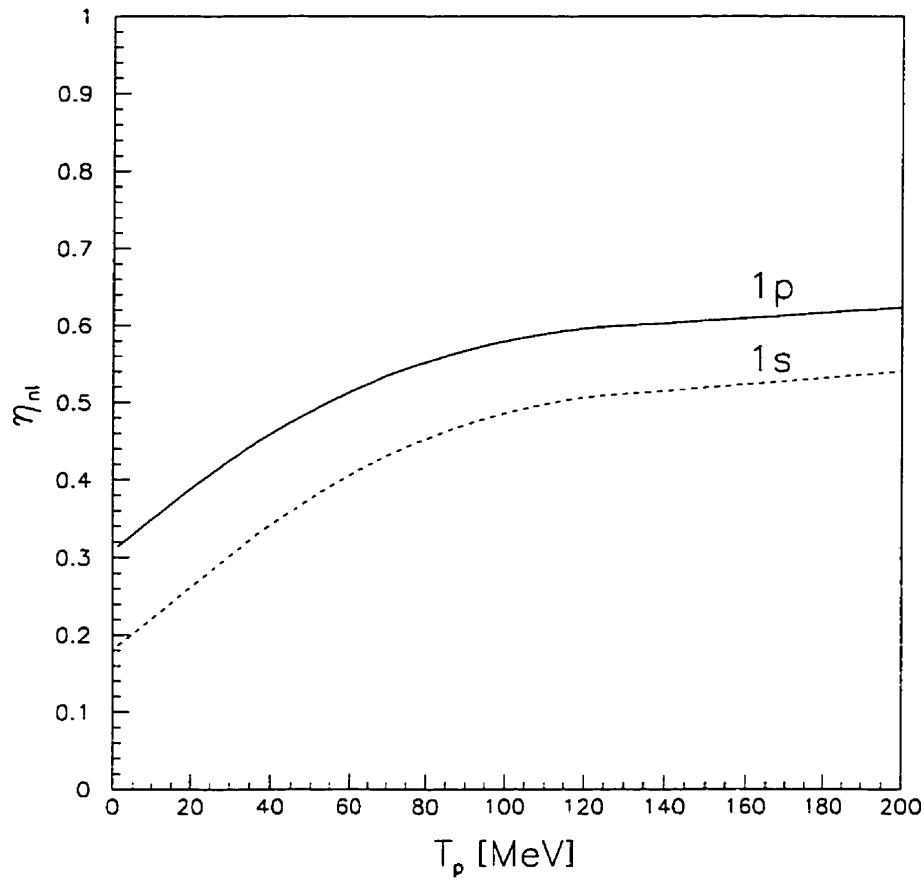

Figure B.9: Proton transparencies for the 1s and 1p harmonic oscillator shells for ^{12}C.

IMAGE EVALUATION
TEST TARGET (QA-3)

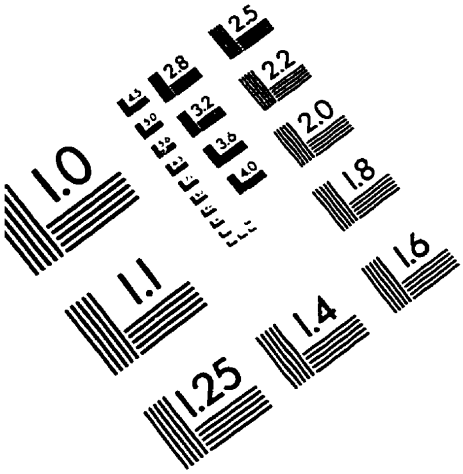

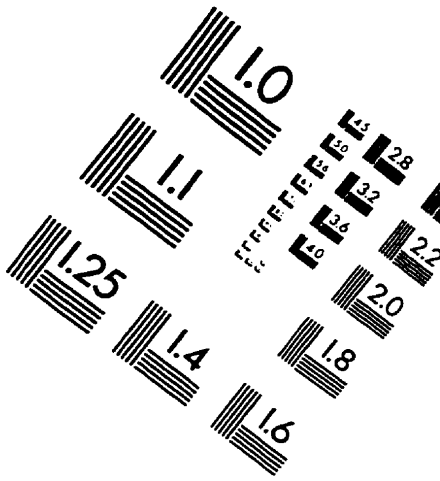

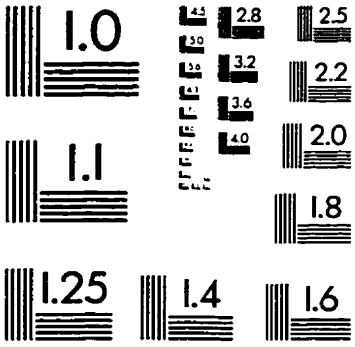

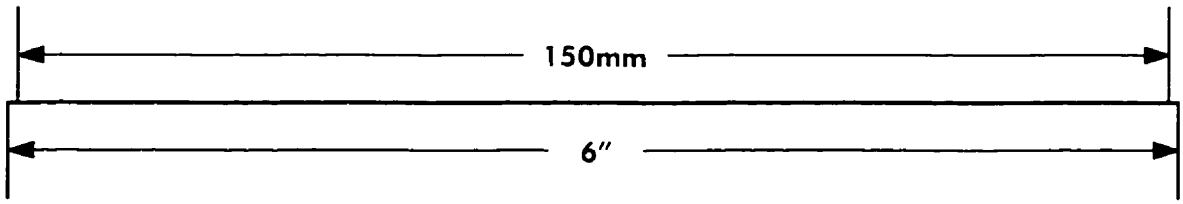

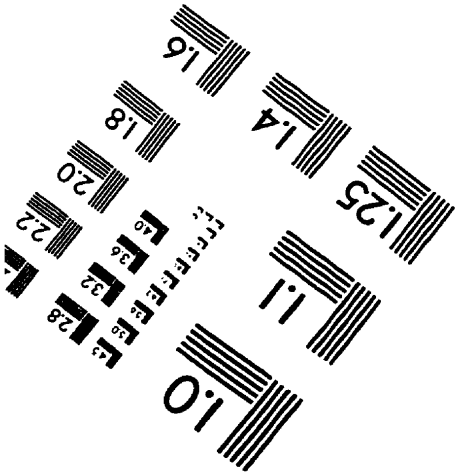

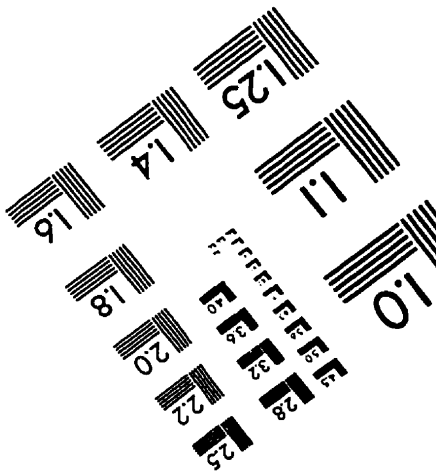

APPLIED IMAGE, Inc
1653 East Main Street
Rochester, NY 14609 USA
Phone: 716/482-0300
Fax: 716/288-5989